

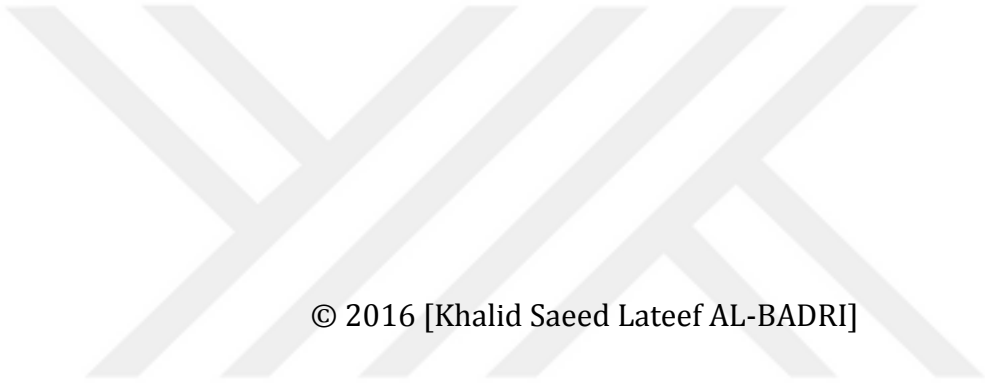
**T.C.**  
**SÜLEYMAN DEMİREL UNIVERSITY**  
**Graduate School of Applied and Natural Sciences**

**MICROWAVE REGION ELECTROMAGNETIC ABSORBER DESIGN  
AND APPLICATIONS**

**Khalid Saeed Lateef AL-BADRI**

**Supervisor**  
**Assist. Prof. Dr. Evren EKMEKÇİ**

**MASTER OF SCIENCE DEGREE (M. Sc.)**  
**DEPARTMENT OF ELECTRONICS AND COMMUNICATION ENGINEERING**  
**ISPARTA - 2016**

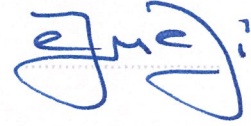


© 2016 [Khalid Saeed Lateef AL-BADRI]

APPROVAL OF THE THESIS

**"Microwave Region Electromagnetic Absorber Design and Applications"**  
submitted by **Khalid Saeed Lateef Al-Badri** in partial fulfillment of the  
requirements for the degree of **Master of Science** in **Department of  
Electronics and Communication Engineering**, Graduate School of Natural and  
Applied Sciences, Süleyman Demirel University by,

**Supervisor**                      **Assist. Prof. Dr. Evren EKMEKÇI**  
Süleyman Demirel University



**Committee Member**            **Prof. Dr. Mustafa MERDAN**  
Süleyman Demirel University



**Committee Member**            **Prof. Dr. Gönül TURHAN SAYAN**  
Middle East Technical University



**Director**                      **Assoc. Prof. Dr. Yasin TUNCER** .....

## **COMMITMENT**

I hereby declare that all information in this document has been obtained and presented in accordance with academic rules and ethical conduct. I also declare that, as required by these rules and conduct, I have fully cited and referenced all material and results that are not original to this work.

**Khalid Saeed Lateef AL-BADRI**



## Contents

	Page
ABSTRACT .....	iv
ÖZET .....	iii
ACKNOWLEDGEMENTS.....	v
LIST OF FIGURES .....	vi
LIST OF TABLES .....	ix
LIST OF SYMBOLS .....	x
1. INTRODUCTION .....	1
1.1. History .....	1
1.2. Advantages of Metamaterial Based Absorbers.....	3
1.3. Aim and Scope of the thesis .....	4
2. THEORETICAL BACKGROUND .....	5
2.1. General Definitions .....	5
2.1.1. Electromagnetic Spectrum and Microwave Range .....	5
2.1.2. Reflection, Transition, and Absorption .....	6
2.2. Electromagnetic Waves Fundamental .....	7
2.3. Boundary Conditions .....	9
2.4. The Wave Equation .....	10
2.5. Wave Impedance .....	11
2.6. Electromagnetic Resonator Structures.....	12
2.6.1. Edge-Coupled Split Ring Resonator (EC-SRR) .....	13
2.6.2. Broadside Coupled SRR (BC-SRR) .....	14
2.6.3. Double-Sided SRR (DSRR) .....	14
2.7. Tuning methods .....	15
2.7.1. Dynamic tuning by active device control .....	15
2.7.2. Dynamic tuning by passive control .....	16
2.8. Electromagnetic Absorbers and Applications .....	17
2.8.1. General Review of Electromagnetic Absorbers and Their Applications .....	18
2.8.1.1. Absorber for broadband applications .....	18
2.8.1.2. Absorber for switching applications .....	18
2.8.1.3. Absorber for sensing applications .....	18
2.9. Modeling Methods .....	19
3. DESIGN, FABRICATION, AND CHARACTERIZATION OF ABSORBER TUNABLE RESONATOR (AD-CRR) STRUCTURE .....	22
3.1. Design .....	22
3.1.1. Simulation environments and methods .....	22
3.1.2. CST microwave studio setup .....	24
3.1.3. Design dimension and materials properties .....	25
3.2. AD-CRR Structure Fabrication and Experimental Setup .....	27
3.2.1. Structure fabrication .....	27
3.2.2. Experimental Setup .....	28
4. Angle Dependent Closed Ring Resonator (AD-CRR) Applications .....	31
4.1. AD-CRR Based Pressure/Weight Sensor .....	31
4.2. AD-CRR Based ON-OFF Switching .....	33
4.3. AD-CRR Based Absorber Modulator .....	34
5. RESULTS AND DISCUSSION .....	36

5.1. Simulation Results .....	36
5.1.1. Absorption reasons .....	39
5.1.2. Impedance matching .....	40
5.1.3. Multi-reflection interference theory .....	41
5.1.4. Effects of changing angle $\alpha$ on absorption spectrum .....	43
5.1.3.1. Explanation for the rapid decreases in absorption level .....	48
5.2. Experimental Realization .....	54
5.3. Influence of Geometrical Parameters .....	56
5.3.1. Influence of substrate thickness (h) .....	56
5.3.2. Influence of ring width (w) .....	57
5.3.3. Influence of ring size ( $L_r$ ) .....	58
5.3.4. Influence of dielectric change ( $\epsilon_r$ ) .....	60
5.3.5. Influence of tangent loss ( $\tan\delta$ ) .....	61
5.4. Scaling Structure to THz Region .....	63
6. CONCLUSION .....	65
Appendix A .....	67
Appendix B .....	70
REFERENCES .....	73

## **ABSTRACT**

**Master of Science**

### **MICROWAVE REGION ELECTROMAGNETIC ABSORBER DESIGN AND APPLICATIONS**

**Khalid Saeed Lateef AL-BADRI**

**Süleyman Demirel University  
Graduate School of Natural and Applied Sciences  
Department of Electronic and Communication Engineering**

**Supervisor: Assist. Prof. Dr. Evren EKMEKÇİ**

In this thesis, a proof of concept study is performed including design, simulations and experiments for a microwave region (i.e. S-band) foldable absorber structure, based on closed ring resonator type metamaterial structure. This design is composed of three layers; one is metallic resonator structure, second the dielectric interlayer which is FR-4 and third the entire ground plane made of 35  $\mu\text{m}$  thick copper.

The proposed absorber structure promises the ability of almost monochromatic tuning of its absorption level at almost constant resonance frequency with a high sensitivity on the folding angle, which is supposed to be desired for many sensing applications. The prototype of the proposed structure is fabricated and experimental results agree very well with the simulations. Additionally, the proposed structure is studied with numerical parametric analysis in details; in order to explain the electromagnetic mechanism.

The results obtained in this work are believed to be exciting for many microwave, terahertz and optical region applications such as; sensor, amplitude modulation, and ON/OFF switching.

**Keywords:** foldable resonator structure, metamaterial, absorber, sensor, on/off switching.

**2016, 84 pages**

## ÖZET

**Yüksek Lisans**

### **MİKRODALGA BÖLGESİ ELEKTROMANYETİK SOĞURUCU TASARIM VE UYGULAMALARI**

**Khalid Saeed AL-BADRI**

**Süleyman Demirel Üniversitesi**

**Fen Bilimleri Enstitüsü**

**Elektronik ve Haberleşme Mühendisliği Anabilim Dalı**

**Danışman: Yrd. Doç. Dr. Evren EKMEKÇİ**

Bu tezde, kapalı halka rezonatör tipi metamalzeme yapısı tabanlı S-bant mikrodalga bölgesi katlanabilir soğurucu yapısı için tasarım, benzetim ve deneysel çalışmaları içeren bir kavram kanıtı çalışması yürütülmüştür. Önerilen tasarım üç katmandan oluşmaktadır. İlki metalik rezonatör yapısı, ikincisi FR-4 dielektrik katman ve üçüncüsü de 35 µm kalınlığında bakırdan yapılmış bütün toprak düzlemdir.

Önerilen soğurucu yapısı soğurma seviyesinin katlama açısına bağlı olarak yüksek hassasiyette ve neredeyse tek frekansta ayarlanma kabiliyetine olanak sağlar ve bunun pek çok algılama uygulaması için arzu edilen bir durum olduğu tahmin edilmektedir. Önerilen yapının prototipi üretilmiş ve deneysel sonuçlar benzetimler ile çok iyi uyum sağlamaktadır. Bunlara ek olarak, önerilen yapının arka plandaki elektromanyetik mekanizmasını açıklamak için nümerik olarak parametrik analizler yapılmıştır.

Bu tez kapsamında elde edilen sonuçların sensor, genlik modülasyonu ve AÇIK/KAPALI anahtarlama gibi pek çok mikrodalga, terahertz ve optik bölgesi uygulama için heyecan verici olduğuna inanılmaktadır.

**Anahtar Kelimeler:** katlanabilir rezonatör yapı, metamalzeme, soğurucu, sensor, açık/kapalı anahtarlama.

**2016, 84 sayfa**

## **ACKNOWLEDGEMENTS**

I should present my private thanks to my supervisor, Assist. Prof. Dr. Evren EKMEKÇİ, for his excellent help, guidance, and encouragement me with an excellent atmosphere for doing my thesis.

And, I should present many thanks to my father, mother, and my brothers.

Also I present greet thanks to my wife and child.

**Khalid Saeed AL-BADRI**

Isparta, 2016



## LIST OF FIGURES

	Page
Figure 2.1. Electromagnetic spectrum (Pozar, 2012) .....	5
Figure 2.2. Wave incident on boundary between two deferent mediums, and according to angle of incident and medium properties reflection and transition wave are generated.....	6
Figure 2.3. Electric and magnetic fields, surface current and charge at a general interface between two media ( Orfanidis 2014)...	10
Figure 2.4. Electromagnetic Resonator Structures (a) derivative of split ring resonator, (b) derivative of loop resonator, (c) spiral resonator, and (d) electric-field-coupled ELC resonator (Munk, 2000) .....	12
Figure 2.5. (a) Edge-Coupled Split Ring Resonator (EC-SRR), (yellow color) represents metallic rings printed on dielectric board (dark gray color). (b) Equivalent circuit model.....	13
Figure 2.6. Broadside Coupled SRR (BS-SRR), (yellow color) represents metallic rings printed on dielectric board (white color).....	14
Figure 2.7. Double-Sided SRR (DSRR), (yellow color) represents metallic rings printed on dielectric board (white color).....	15
Figure 2.8. Types of tuning methods.....	17
Figure 2.9. Electromagnetic plane wave normal incidence on interface between two different medium, reflection plane wave, and transition plane wave (Cheng, 1993) .....	20
Figure 3.1. Ring resonator with unite cell periodic boundary condition, when EM wave normal incident on resonator plane .....	23
Figure 3.2. Ring unite cell resonator with PEC and PMC boundary condition, when EM wave normal incident on resonator plane.	24
Figure 3.3. CST simulation setup, green sides represent PEC boundary, port one in -z-direction and port two +z-direction .....	25
Figure 3.4. Schematic of AD-CRR. (a) Schematic perspective view, (b) Schematic side view, (c) schematic perspective view two symmetrical parts. (Note that the parts are connected to each other during the simulation and experiments).....	26
Figure 3.5. Schematic of perspective view for AD-CRR structure.....	27
Figure 3.6. (a) Photograph of two half parts of AD-CRR structure, (b), (c), and (d) Photographs of 10 <sup>0</sup> , 30 <sup>0</sup> , and 60 <sup>0</sup> respectively .....	28
Figure 3.7. Photographes show the expermental (a) vector network analyzer (VNA) (Agilent Fieldfox N9926A) connected to waveguid, (b) two waveguid ports connected through $\lambda/4$ spacer (i.e. sample holder) .....	29
Figure 3.8. Thru-Reflect-Line (TRL) calibration flowchart .....	30
Figure 4.1. Schematic of pressure sensor layer one and two resonator layer, yellow color represent copper green substrate .....	31
Figure 4.2. State process of AD-CRR based on pressure sensor .....	32
Figure 4.3. ON/OFF switch based on absorber, the switch convert between reflection and absorption state (a) ON- state reflection, and (b) OFF state absorption .....	33
Figure 4.4. AM modulator structure .....	34
Figure 5.1. Absorption and reflection spectra for AD-CRR at $\alpha = 0^0$ .....	37

Figure 5.2. z-component of electric field distribution for E-field along y-axis at resonance frequency 2.805 GHz, (a) for ring, and (b) for ground plane .....	37
Figure 5.3. Magnetic field distribution for H-field along x-axis at resonance frequency 2.805 GHz, (a) top view in (xy-plane), and (b) side view in (xz-plane) .....	38
Figure 5.4. Surface current distribution for at resonance frequency 2.805 GHz, (a) ring, and (b) ground plane .....	39
Figure 5.5. Three cases of table 4.1, (a) absorption as a function of frequency, and (b) power as a function of frequency .....	40
Figure 5.6. Calculated normalized impedance and absorption plots. The dashed line is set at resonance frequency 2.811 GHz.....	41
Figure 5.7. Calculated absorption and reflection in normal incident consideration by using interference model .....	43
Figure 5.8. Calculated propagation phase in normal incident consideration by using interference model .....	43
Figure 5.9. Simulation result for absorption level related with changing in rotation angle ( $\alpha$ ) .....	45
Figure 5.10. Simulation result for Reflection coefficient $S_{11}$ with respect to frequency .....	45
Figure 5.11. Simulation result for transition coefficient $S_{21}$ related with frequency .....	45
Figure 5.12. The relation between angles and absorption peaks, (red-line) linear fitting curve according to equation $A = -0.016 \times \alpha + 0.98$ .....	46
Figure 5.13. H-field components obtained by using xz-cutting plane at $y = 0$ , (a) $\alpha = 0^\circ$ , (b) $\alpha = 10^\circ$ , (c) $\alpha = 20^\circ$ , (d) $\alpha = 30^\circ$ , (e) $\alpha = 40^\circ$ , (f) $\alpha = 50^\circ$ , and (g) $\alpha = 60^\circ$ .....	47
Figure 5.14. Absorber structure for comparative, all geometrical dimensions similar to Table 3. . The all structure parts rotate as one part .....	49
Figure 5.15. Absorption related with rotation angle for comparable design .....	50
Figure 5.16. Vector analysis for $E_x$ , and $E_z$ .....	51
Figure 5.17. E-field x-component (a-g) for CAR-CRR, and (f-n) for AD-CRR, for each rotation angle $0^\circ$ , $10^\circ$ , $20^\circ$ , $30^\circ$ , $40^\circ$ , $50^\circ$ , and $60^\circ$ respectively .....	52
Figure 5. 18. E-field z-component (a-g) for CAR-CRR, and (f-n) for AD-CRR, for each rotation angle $0^\circ$ , $10^\circ$ , $20^\circ$ , $30^\circ$ , $40^\circ$ , $50^\circ$ , and $60^\circ$ respectively.....	53
Figure 5. 19. Experimental result for absorption level related with changing in rotation angle ( $\alpha$ ) .....	55
Figure 5. 20. Experimental result for reflection level related with changing in rotation angle ( $\alpha$ ) .....	55
Figure 5. 21. Experimental result for transition level related with changing in rotation angle ( $\alpha$ ) .....	55
Figure 5. 22. Influence of changing substrate thicknesses .....	57
Figure 5. 23. Effect of ring width in absorption level .....	58
Figure 5. 24. The effect of changing ring size in absorption level .....	59

Figure 5. 25. The effect of changing substrate dielectric constant in absorption level .....	60
Figure 5. 26. The effect of tangent loss $\tan\delta$ changes in absorption level....	62
Figure 5. 27. The effect of changing tangent loss $\tan\delta$ in absorption bandwidth for rotation angle = $0^\circ$ .....	62
Figure 5. 28. Absorption level related with frequency for all rotation angles for scaling structure .....	64
Figure A. 1. Electromagnetic plane wave normal incidence on interface between two different medium, reflection plane wave, and transition plane wave (Cheng, 1993) .....	67
Figure B. 1. Electromagnetic plane wave oblique incidence on interface between two different medium by incident angle $\theta_i$ .....	70



## LIST OF TABLES

	Page
Table 2. 1. Approximate Microwaves Sub-bands Designations (Pozar, 2012) .....	5
Table 3. 1. AD-CRR parameters list .....	26
Table 5. 1. Three different cases .....	40
Table 5. 2. Relation between change in angle and (resonance frequency, maximum surface current, maximum E-field, and maximum H-field) .....	46
Table 5. 3. The shift in resonance frequency according to angle step .....	48
Table 5. 4. Shift of resonance frequency related with rotation angle for comparative design.....	49
Table 5. 5. Comparison between simulation and experimental results.....	56
Table 5. 6. Relation between rotation angle, absorption level, and resonance frequencies $f_0$ (GHz) for three steps of changing in substrate thicknesses .....	57
Table 5. 7. Relation between rotation angle, absorption level, and resonance frequencies $f_0$ (GHz) for different ring width .....	58
Table 5. 8. Relation between rotation angle, absorption level, and resonance frequencies $f_0$ (GHz) for three steps of changing ring size .....	59
Table 5. 9. Relation between rotation angle, absorption level, and resonance frequencies $f_0$ (GHz) for three different substrate dielectric constants values .....	61
Table 5.10. The effect of changing tangent loss $\tan\delta$ in absorption bandwidth area under curve for rotation angle $\alpha = 0^0$ .....	64

## LIST OF SYMBOLS

AD-CRR	Angle Dependent Closed Ring Resonator.
B	Magnetic Flux Density
D	Electric Flux Density
DNG	Double Negative
E	Electric Field Intensity
EC-SRR	Edge-Coupled Split Ring Resonator
EMA	Electromagnetic Absorber
EMC	Electromagnetic Compatibility
EMI	Electromagnetic Interference
$\epsilon_0$	Free Space Permittivity $8.854 \times 10^{-12}$ Farad/Meter
$\epsilon_r$	Complex relative Electric Permittivity
FSS	Frequency Selective Surfaces
H	Magnetic Field Intensity
HIS	High Impedance Surface
J	Electric Current Density Vector In Amperes / Meter <sup>2</sup>
M	Magnetic Current Density Vector/Meter <sup>2</sup>
PEC	Perfect Electrically Conducting
R	Wave reflected
RCS	Radar Cross Section
T	Wave transmitted
TEM	Transverse electromagnetic
$\lambda$	Wavelength
$\mu_0$	Free Space Permeability $4\pi \times 10^{-7}$ Henry/Meter
$\mu_r$	Complex relative Magnetic Permeability
$\rho_e$	Electric Charge Density In Coulombs/Meter <sup>3</sup>
$\rho_m$	Magnetic Charge Density In Webbers/Meter <sup>3</sup>
$k$	Propagation Constant of Free Space.
$\gamma$	Propagation Constant
$\eta$	Intrinsic impedance
$\sigma$	Conductivity of Material (S/M).

## 1. INTRODUCTION

In recent years, metamaterial based absorber devices has received researchers' attentions since Landy et al. opened a new path in metamaterials subject in 2008 with their work entitled 'Perfect Metamaterial Absorber PMA' (Landy et al., 2008). Until now, there have been more than one thousand research papers in this field according to ISI Knowledge. Therefore, in the introduction it will be useful to provide some brief consolidated information in order to draw a complete image about absorbers.

### 1.1. History

In the 3<sup>rd</sup> decade of the 19<sup>th</sup> century, exactly in 1930, the first experimental work and theoretical description of microwave absorber was presented (Emerson 1973), when the scientists at Namaalooze Vennootschap Machinereen in Holland investigated a quartz resonator at 2 GHz. However, this absorber depended on increasing the dielectric constant to provide high dissipation in very low thickness by using **TiO<sub>2</sub>** (carbon black). The first application of absorber was used to cover the back side of an antenna to cancel the effect of electromagnetic wave interference (Emerson 1973).

During the World War II, the demand on using absorber structures increased, because the two encampments (USA army and Germany army) heavily depended on radars in battlefield. The USA army with MIT Radiation Laboratory developed Halpern Anti-Radiation Paint (**HARP**) in a research led by Mr. Halpern (Halpern et al., 1946) to increase the efficiency of radar by decreasing the radiation interference from nearby objects. HARP absorber was also based on carbon black but with rubber filling carried on aluminum flakes and barium titanate disc. This absorber was used to cover aircraft because it is very thin about 0.6 mm and provided very good absorption peak about -15 dB in X-band region. On the other hand scientists from Germany, also designed some absorber structures in this period such as multilayer Jaumann absorber, which depended on resistive shite and regard plastics (du Toit et al., 1990).

In 1952, Mr. Winfield Salisbury from America investigated a simple resonance microwave absorber based on resistive sheet. This type of absorber gave zero reflection when the resistance of sheet is equal to free space impedance  $377 \Omega$ . The construction of this absorber depended on three or more layers. The first one was resistive sheet, the second layer was an air gap with thickness equal to the quarter of the incident wavelength, and the third layer was perfect electrically conducting (PEC) ground plate (Che et al., 2011).

To demonstrate the success of the designed absorber structures, researchers needed some sophisticated measurement setups in the laboratory. The anechoic chambers became essential here by preventing any unwanted environmental reflections. To achieve that polymer foams with carbon black was used to cover the inside wall of a room in long pyramidal structures. Hence, this setup provided wide and high electromagnetic absorber (Emerson 1973).

At the end of 1968 Benedikt A. Munk, from Ohio, investigated a new method known as Frequency Selective Surfaces (FSS). FSS take place in many applications such as radomes, filters applications, missiles shielding, sensors, anechoic chambers absorption enhancement and electromagnetic shielding applications (Mitra et al., 1988). Since the main function of FSS structure was to provide a High Impedance Surface (HIS) depending on the resonance structure, this type of absorber enhanced the problem in previous absorber designs in HARP. Salisbury resistive sheet and Jaumann represented an electromagnetic wave absorber, but they attenuated the wanted wave (Abdin et al., 2012).

The theoretical description of left-handed materials by V.G. Veselago in 1968 opened the door for Professor John Pendry who had been the first to investigate the first metamaterial structure after thirty years. After that in 2008, Professor N. I. Landy and his group presented the first microwave absorber based on metamaterials which was published as the first article in this field (Landy et al., 2008).

## 1.2. Advantages of Metamaterial Based Absorbers

There are many advantages of using metamaterial based absorbers. One is, they can be designed as active or passive devices. The other advantages are being thin (Lee et al., 2016), ease of manufacturing (Watts et al., 2012), being small in structure size, providing high absorption levels, ability to be tuned, and possibility of frequency scaling for example scaling the operating band from microwave to THz by just physically scaling the structure (Landy et al., 2008). Metamaterial based absorbers played a key role in developing a lot of applications such as the single band perfect absorber (Yu et al., 2015), multi band absorber (Yoo et al., 2015), broadband absorber (Aydin et al., 2011), and polarization insensitive absorber (Dincer et al., 2014). They are also used for enhancing the electromagnetic shielding (Sabah et al., 2014), enhancing the radar cross section in antenna applications (Zhang et al., 2014), cloaking the objects (Shao et al., 2013), changing the polarization of the wave (Huang, et al., 2014), switching the absorption spectra on/off (Ekmekci et al., 2015), energy harvesting (Dincer 2015), sensing application (Lee et al., 2016), and etc.

Specifically, absorber based sensors are also growing rapidly due to design flexibility, tuning ability, and availability in large frequency ranges. Therefore, in order to design a good sensor structure based on an absorber device, the reflection from the absorber and the transmission through it should be controlled in some way in order to support sensor function as much as possible. However, controlling electromagnetic reflection from a sensor and/or transmission is a bit difficult (Mandal et al., 2013). This will be the main goal of the thesis. There are a few tuning methods in literature such as; structure rearranging (Zhu et al., 2012), broken structure symmetry (Valente et al., 2015), layer shifting in double layer designs (Ekmekci et al., 2015), using sensitive materials (i.e. electric sensitive material (Manceau et al., 2010), thermal sensitive (Valente et al., 2015), and chemical sensitive (Withayachumnankul et al., 2012)).

Moreover, microwave region takes an important part in communication technologies, especially in mobile communications, Wi-Fi systems, satellite communications, medical devices, sensing applications, and military communication systems (Feng et al., 2007). Considering the high demand for microwave communication systems together with the laboratory facilities, the absorber design that will be conducted in this thesis is planned to be in microwave region.

### **1.3. Aim and Scope of the Thesis**

The aim of this thesis is to investigate the literature about resonator based absorber designs, understanding the theory, learning the simulation techniques, propose a novel structure, fabrication and measurement of the novel structure and proposal of some possible applications..

This work will cover simulation and fabrication of tunable resonator absorber in microwave frequencies (S-band). However, some simulation results will also be provided for terahertz region (far-infrared) .

## 2. THEORETICAL BACKGROUND

This section includes the required theoretical background for the thesis studies.

### 2.1. General Definitions

In this part some general definitions are provided.

#### 2.1.1. Electromagnetic Spectrum and Microwave Range

Electromagnetic spectrum, this term refers to all ranges of frequencies; starting from very low frequencies to very high frequencies. Moreover, electromagnetic spectrum is divided into some regions like microwave, infrared, visible light and etc. Generally, the term microwave is generally used to specify the range of frequencies from upper limit of VHF (Very High Frequency) 3 GHz to 300 GHz, with corresponding wavelength ( $\lambda$ ) from 10 cm at 3 GHz to 1 mm at 300 GHz (see Figure 2.1). The microwave region is also divided into various frequency bands as demonstrated in Table 2.1 (Pozar, 2012).

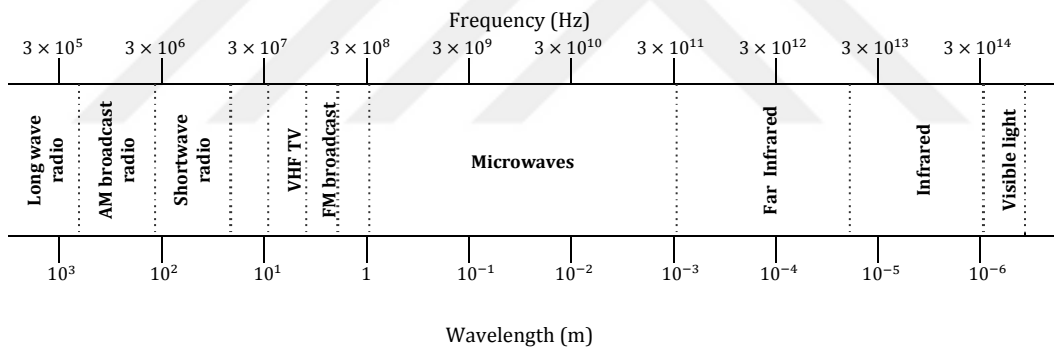


Figure 2.1. Electromagnetic spectrum (Pozar, 2012)

Table 2. 1. Approximate Microwaves Sub-bands Designations (Pozar, 2012)

<b>Band name</b>	<b>Frequency range (GHz)</b>
Ultra-high frequency (UHF)	0.3–3
L band	1–2
S band	2–4
C band	4–8
X band	8–12
Ku band	12–18
K band	18–26
Ka band	26–40
U band	40–60
V band	50–75

E band	60-90
W band	75-110
F band	90-140

### 2.1.2. Reflection, Transition, and Absorption

These three definitions which are very important in this thesis therefore they will be elaborated in detail. **Wave reflection R** means the process when electromagnetic wave meets the boundary between the two medium reflected back in the same medium (remain in the first medium). According to the law of reflection, the direction and angle of the reflected wave can be specified (Daintith et al., 2005) (see Figure 2.2.). Additionally, the reflection can be a total reflection or a partial reflection as we see later in section 2.3. Boundary conditions. **Wave transmitted T** is the amount of wave that are transmitted through the boundary between two deferent mediums and it depends on the two medium properties see (Figure 2. 2).

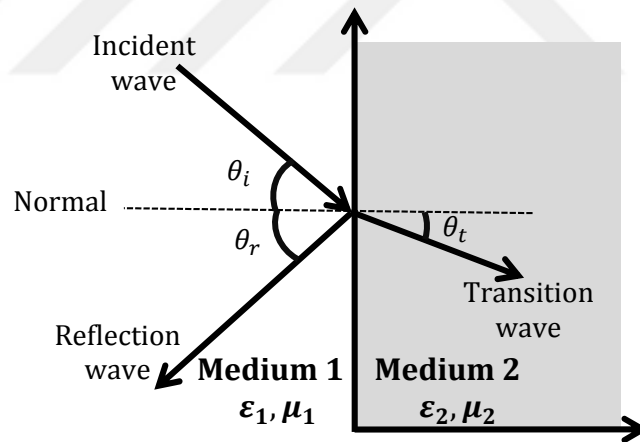


Figure 2. 2. Wave incident on boundary between two deferent mediums, and according to angle of incident and medium properties reflection and transition wave are generated.

**Absorption A** refers to the amount of energy that is dissipated into absorber, thereby when the absorption increase, the reflection and transmission decreases (Watts et al., 2012). Hence, the electromagnetic absorber can be defined as the structure which can absorb electromagnetic energy and convert

it into heat and other energy forms (Zhu et al., 2010), (Watts et al., 2012), (Landy et al., 2008). According to absorption band the electromagnetic absorber EMA can be classified into two types:

1. Resonated Absorber: This type depends on interaction of electromagnetic wave with resonator structure configuration at designed resonance frequency (Watts et al., 2012). Therefore, the resonance frequency is important factor in many applications. The mechanism of this type in general depends on reflection factor at the resonance frequency. In this way, the absorber structure works to reduce the amount of electromagnetic reflection when the wave transmission is set at zero level by using entire ground plate at the background (Balamati et al., 2016).
2. Broadband Absorber: The important property of this type is that; it does not depend on resonance frequency, but it has a vast range of absorption frequencies bands, inherent from material absorber properties (Watts et al., 2012).

## **2.2. Electromagnetic Waves Fundamental**

When a wave strikes an object, it may pass through object, be reflected, or be absorbed. James Clerk Maxwell presents a set of mathematical functions based on Gauss' law, Faraday's law and Ampere's law in order to explain and analyze these operations for electromagnetic waves stroked on a boundary between different medium (Celozzi et al., 2008). In summary, Faraday's law specifies the relation between electric field intensity and change in magnetic flux density equation (2. 1). However, Ampere's law (equation (2. 2)) explains the change in electric flux density which changes magnetic field intensity when the electric current passes through closed loop. The last two has important relations Gauss' laws for electric and magnetic charge. The electric flux density is caused by an electric charge inside closed surface area.

$$\vec{\nabla} \times \vec{\mathcal{E}} = -\frac{\partial \vec{\mathcal{B}}}{\partial t} - \vec{\mathcal{M}} \quad (\text{Faraday's law}), (2. 1)$$

$$\vec{\nabla} \times \vec{\mathcal{H}} = \frac{\partial \vec{\mathcal{D}}}{\partial t} + \vec{\mathcal{J}} \quad (\text{Ampere's law}), (2. 2)$$

$$\vec{\nabla} \cdot \vec{\mathcal{D}} = \rho_e \quad (\text{Electric Gauss' law}), (2. 3)$$

$$\vec{\nabla} \cdot \vec{\mathcal{B}} = \rho_m \quad (\text{Magnetic Gauss' law}), (2. 4)$$

Where:  $\vec{\mathcal{B}}$  is the magnetic flux density,  $\vec{\mathcal{E}}$  is the electric field intensity,  $\vec{\mathcal{D}}$  is the electric flux density,  $\vec{\mathcal{H}}$  is the magnetic field intensity,  $\vec{\mathcal{J}}$  is the electric current density vector in amperes per square meter,  $\vec{\mathcal{M}}$  is the magnetic current density Volt/meter<sup>2</sup>,  $\rho_e$  is the electric charge density in Coulombs/meter<sup>3</sup>, and  $\rho_m$  is the magnetic charge density in Webers/meter<sup>3</sup>

There are also three important constitutive relations defined between field's values ( $\vec{\mathcal{E}}$ ,  $\vec{\mathcal{D}}$ ,  $\vec{\mathcal{B}}$ ,  $\vec{\mathcal{H}}$ , and  $\vec{\mathcal{J}}$ ) and medium properties:

$$\vec{\mathcal{B}} = \mu_r \mu_0 \vec{\mathcal{H}} \quad (2. 5)$$

$$\vec{\mathcal{D}} = \epsilon_r \epsilon_0 \vec{\mathcal{E}} \quad (2. 6)$$

$$\vec{\mathcal{J}} = \sigma \vec{\mathcal{E}} \quad (2. 7)$$

Where:

$\epsilon_r$  is the complex relative electric permittivity,  $\epsilon_0$  free space permittivity which is  $8.854 \times 10^{-12}$  Farad/meter,  $\mu_r$  is the complex relative magnetic permeability,  $\mu_0$  free space permeability which is  $4\pi \times 10^{-7}$  Henry/meter,  $\sigma$  is the conductivity of material (S/m).

In other words, the medium properties (relative permittivity and relative permeability) can be rewritten in another form as real and imaginary components.

$$\boldsymbol{\epsilon}_r = \frac{\boldsymbol{\epsilon}}{\boldsymbol{\epsilon}_0} = \boldsymbol{\epsilon}_r - j\boldsymbol{\epsilon}_r \quad (2.8)$$

$$\boldsymbol{\mu}_r = \frac{\boldsymbol{\mu}}{\boldsymbol{\mu}_0} = \boldsymbol{\mu}_r - j\boldsymbol{\mu}_r \quad (2.9)$$

All the above equations (2. 1, 2. 2, 2. 3 and 2. 4) are time dependent. However, in many times, to get rid of time dependence, the phasor forms of these equations are preferred. Therefore, the phasor forms are given below (where  $\omega = 2\pi f$ ):

$$\vec{\nabla} \times \vec{\mathcal{E}} = -j\omega\vec{\mathcal{B}} - \vec{\mathcal{M}} \quad (\text{Faraday's law}), (2.10)$$

$$\vec{\nabla} \times \vec{\mathcal{H}} = j\omega\vec{\mathcal{D}} + \vec{\mathcal{J}} \quad (\text{Ampere's law}), (2.11)$$

$$\vec{\nabla} \cdot \vec{\mathcal{D}} = \rho_e \quad (\text{Electric Gauss' law}), (2.12)$$

$$\vec{\nabla} \cdot \vec{\mathcal{B}} = 0 \quad (\text{Magnetic Gauss' law}), (2.13)$$

### 2.3. Boundary Conditions

Previous section focused on the electric and magnetic field propagates in free space medium and supposed that this medium has no obstacle disturbing the propagation of the electromagnetic wave. However in practice, there is no unbounded medium. It infers that any medium ought to have own limits, which are in contact with the other media. Also there are a lot off objects hinder propagation. Additionally previous section presented the electromagnetic fields inside medium related to each other (according to relations 2. 5, and 2. 6). The transition of wave from one medium to another, it means there are two different

contiguous mediums with different constitutive properties ( $\epsilon_1, \mu_1$ , and  $\epsilon_2, \mu_2$ ). So, the Maxwell's equations take the below forms:

$$\mathbf{D}_{1n} - \mathbf{D}_{2n} = \rho_s \quad (2.14)$$

$$\mathbf{B}_{1n} - \mathbf{B}_{2n} = \mathbf{0} \quad (2.15)$$

$$\mathbf{E}_{1t} - \mathbf{E}_{2t} = \mathbf{0} \quad (2.16)$$

$$\mathbf{H}_{1t} - \mathbf{H}_{2t} = \mathbf{J}_s \times \hat{\mathbf{n}} \quad (2.17)$$

Where:  $\rho_s$  is the free surface charge (coulomb/m<sup>2</sup>),  $\mathbf{J}_s$  the free surface current (ampere/m<sup>2</sup>),  $\hat{\mathbf{n}}$  is a unit normal outward from the surface from medium 2 to medium 1, see Figure 2. 3 (Orfanidis, 2014). Therefore the tangential components of the E-field are continuous across the interface; then the difference of the tangential components of the H-field is equal to the surface current density; the difference of the normal components of the flux density D are equal to the surface charge density; and the normal components of the magnetic flux density B are continuous.

$$\mathbf{D}_{1n} = \mathbf{D}_{2n} \quad (2.18)$$

$$\mathbf{B}_{1n} = \mathbf{B}_{2n} \quad (2.19)$$

$$\mathbf{E}_{1t} = \mathbf{E}_{2t} \quad (2.20)$$

$$\mathbf{H}_{1t} = \mathbf{H}_{2t} \quad (2.21)$$

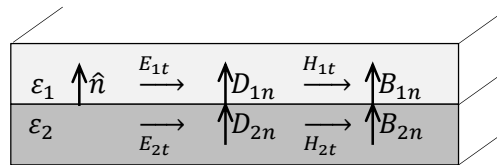


Figure 2. 3. Electric and magnetic fields, surface current and charge at a general interface between two media (Orfanidis, 2014).

## 2.4. The Wave Equation

By using Faraday's law (2. 10) and Ampere's law (2. 11), Helmholtz derived a partial derivative second order wave equation, or Helmholtz equation for free-source, homogenous medium (homogenous means that the characteristics

properties of medium  $\epsilon, \mu$  and  $\sigma$  do not change inside medium. Then, inhomogeneous medium the characteristics properties are changing from point to point inside medium) and isotropic medium. This equation is more reliable form, as it described the wave according to either only  $\vec{\mathcal{E}}$  (**electric**) field or only  $\vec{\mathcal{H}}$  (**magnetic**) field.

$$\nabla^2 \vec{\mathcal{E}} + \gamma^2 \vec{\mathcal{E}} = \mathbf{0} \quad (2.22)$$

$$\nabla^2 \vec{\mathcal{H}} + \gamma^2 \vec{\mathcal{H}} = \mathbf{0} \quad (2.23)$$

Where:  $\gamma = \sqrt{j\omega\mu(\sigma + j\omega\epsilon)} = \alpha + j\beta$  is the propagation constant of the medium in 1/ Meter.

Herein  $\alpha$  is defined as attenuation constant (specifies the attenuation of the electromagnetic wave propagating through a medium) and  $\beta$  is the phase constant (specifies the change in the phase of an electromagnetic wave propagating through a medium).

## 2.5. Wave Impedance

In general, the term wave impedance or intrinsic impedance is used to describe the ratio of  $E$  field to  $H$  field for a **TEM** (transverse electromagnetic) wave that propagates along a medium (Pozar, 2012). Since, the wave impedance in free space is shown below, when  $\sigma$  conductivity is zero,  $\epsilon_0$  free space permittivity is  $8.854 \times 10^{-12}$  Farad/meter, and  $\mu_0$  free space permeability is  $4\pi \times 10^{-7}$  Henry/meter:

$$\mathbf{Z} = \frac{E_x}{H_y} = \sqrt{\frac{j\omega\mu_0}{\sigma + j\omega\epsilon_0}} \approx 377 \Omega \quad (2.24)$$

The above function combines between electric and magnetic properties of the wave. Therefore, it is very important in the absorption mechanism as it will be demonstrated in the following section.

## 2.6. Electromagnetic Resonator Structures

At the beginning of 1990's decade was introduced very interested and wide applicable artificial resonator structure, (especially in the materials that work at microwave region) was introduced. Then, this artificial structure has opened the door to new sub-science fields in physic and electromagnetic engineering. Later these materials are called as “metamaterials”.

These structures take many-engineered shapes according to applications goals such as split ring resonator (Pendry et al., 1999), ring resonator (Shen et al., 2011), (Huang, and Chen, 2011), spiral resonator (Huang et al., 2013), (Zhong, and He, 2013), triangular resonator (Zhang et al., 2015), hexagonal resonator (Bingham et al., 2008), electric-field-coupled (ELC) resonator (Bingham et al., 2008) (Ekmekci et al., 2011), and etc. (see Figure 2.4). From the basic principle of metamaterials design, the structure elements must be much smaller than the operating frequency i.e. sub-wavelength for the effective medium approach (Zouhdi et al., 2012) (Balanis 2012). Hence, “Metamaterials are macroscopic composites having that are man-made, three-dimensional, periodic cellular architecture designed to produce an optimized combination, not available in nature, with two or more responses to specific excitation” (Munk 2008).

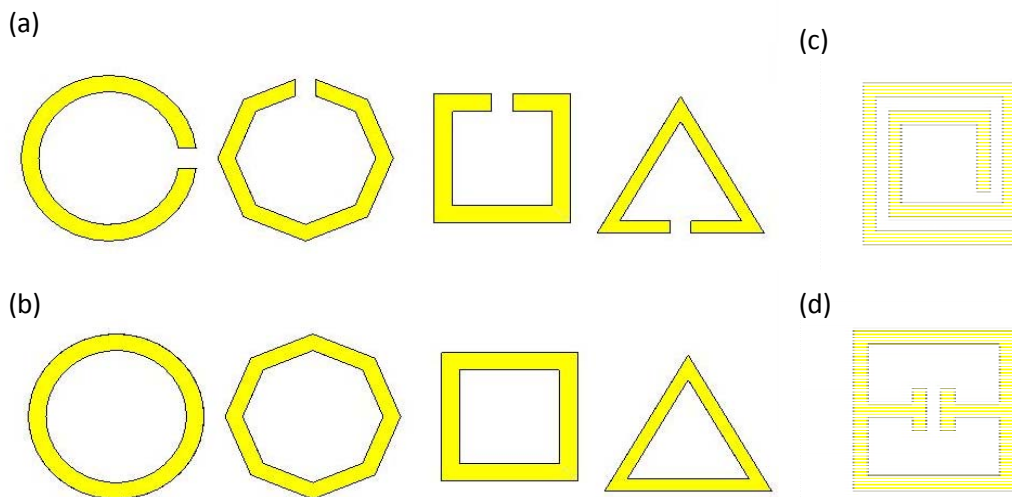


Figure 2.4. Electromagnetic resonator structures (a) Derivatives of split ring resonator, (b) derivatives of loop resonator, (c) spiral resonator, and (d) electric-field-coupled ELC resonator (Munk, 2000)

The next sub sections present the basic and important resonators as these resonators play important roles in many designs and applications.

### 2.6.1. Edge-Coupled Split Ring Resonator (EC-SRR)

The first artificial magnetic resonator structures suggested by Pendry et al. were SRR (Split Ring Resonator) and swiss rolls (Pendry et al., 1999). However, SRR is the most popular one. This design consists of two rings split from each other by a small gap. Generally, each ring has a small cut positioned on opposite side. These rings are made of metal, commonly copper in microwaves, and printed on dielectric substrate (see Figure 2. 5.(a)). The EC-SRR resonates when the time varying electromagnetic wave is perpendicular into the plane of rings. Moreover, the exiting electromagnetic wave generates strong current flow at the resonance frequency (Marques et al., 2008). In most cases, the  $LC$ -resonance circuit model is used to understand the mechanism of resonance. The current is distributed symmetrically around the line pass the center of two rings gap. Finally, the equivalent circuit model consists of two capacitances serially (then can be represented by a single equivalent capacitance) connected in parallel with the inductance (Ekmekci et al., 2009). Directly the resonance frequency can be calculated in equation (2. 23), the value of  $L$ , and  $C$  depending on material properties and shape (Bilotti et al., 2007) and (Marques et al., 2008).

$$\omega_o = 2\pi f_o = 1/\sqrt{LC} \quad (2. 25)$$

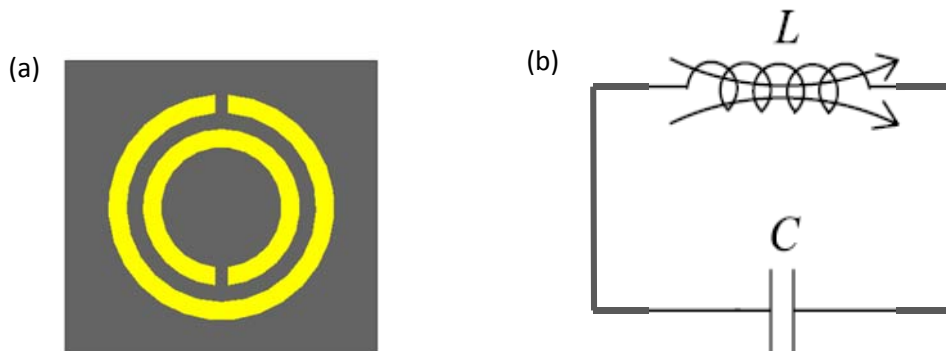


Figure 2. 5. (a) Edge-Coupled Split Ring Resonator (EC-SRR), (yellow color) represents metallic rings printed on dielectric board (dark gray color). (b) Equivalent circuit model.

### 2.6.2. Broadside Coupled SRR (BC-SRR)

Another important magnetic resonator design called broadside coupled SRR (BC-SRR) is proposed by Marques et al. (Marques et al., 2002). This design in short way consists of two identical rings printed on both sides of the substrate; however the gaps directions are positioned as  $180^\circ$  apart from each other (see Figure 2.6). The main advantage of this design is to provide higher capacitance than EC-SRR because of the relative displacement current generated between the two parallel plate rings (Marques et al., 2008), (Ekmekci et al., 2011). For this modification, the capacitance strongly depends in square root of substrate thickness, and inverse square root of substrate relative permittivity (Marques et al., 2008).

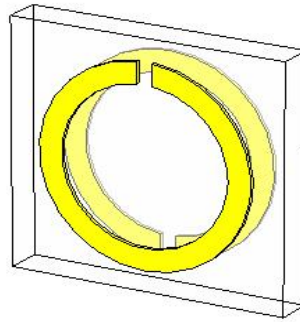


Figure 2.6. Broadside Coupled SRR (BC-SRR), (yellow color) represents metallic rings printed on dielectric board (white color).

### 2.6.3. Double-Sided SRR (DSRR)

In 2009 Ekmekci et al. investigated a hybrid design from EC-SRR and BC-SRR, this new design was constructed by printing two EC-SRRs by  $180^\circ$  symmetric difference (see Figure 2.7) on each sides of the substrate. The equivalent circuit can be presented by using two EC-SRR connected in parallel form across parallel capacitance that come from BC-SRR in between the two EC-SRR (Ekmekci et al., 2009). This design become more sensitive to the substrate parameters than ordinary EC-SRR and electrically smaller. (Ekmekci et al., 2009).

The sub-sections above presented demonstrate the basic and well known structures. Many designs and applications were performed according to their

engineering and physics principles such as many cuts at the rings, different cut size, using different geometries (i.e. squares, triangle and hexagon ring, etc). (Bingham et al., 2008), (Shen et al., 2011), (Huang et al., 2013), (Zhang et al., 2015), (Wang et al., 2015).

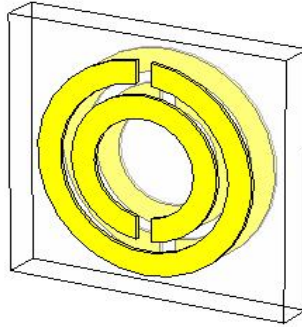


Figure 2.7. Double-Sided SRR (DSRR), (yellow color) represents metallic rings printed on dielectric board (white color).

## 2.7. Tuning methods

There are many methods presented in literature on tunable absorber designs. These methods depend on the application and how they reflect the dynamic change in absorption to support the specific function of an application, such as tuning the resonance frequency (Han et al., 2014), controlling wave phase (Mirza et al., 2009), tuning absorption peak level (Averitt et al., 2007), and tuning the quality factor (Q-Factor) (Naqui et al., 2013). Additionally, the dynamic change can be classified into two main categories (see Figure 2. 8). Dynamic tuning by active device control (Watts et al., 2014), (Ekmekci et al., 2011) as it will be discussed in 2.7.1. and dynamic tuning by passive device control (Zaichun et al., 2012) which will be discussed in section 2.7.1. and 2.7.2.

### 2.7.1. Dynamic tuning by active device control

Active control means realization of the tunability by using an external active source. There are some examples in literature. The switching state had been achieved by using electronic diode connected in series with the resonator to control between two states which are perfect absorbance and reflectance (Xu et

al., 2013). Yuan, et al., obtained resonance frequency tuning by controlling the bias voltage of a varactor diode (Yuan et al., 2015). In varactor diode, changes in the bias voltage cause relatively smooth changes in the junction capacitance (Pozar, 2012). By using a different method, He et al. achieved the tuning of absorption peak level and/or resonance frequency by using semiconductor substrate that can control the conductivity of the substrate by controlling the substrate bias voltage (He et al., 2014). Additionally, the tunability is achieved by using photo excitation semiconductor substrate, such as Gallium Arsenide (GaAs), where the external photo source causes changing in relative permittivity of GaAs semiconductor substrate (Manceau et al., 2010).

### **2.7.2. Dynamic tunable by passive control**

Passive tuning depends on controlling electric and/or magnetic coupling, such as, near field effect between resonators (Zheludev et al., 2012), or the changing in excitation field. There are many tuning methods in literature such as plane shift. Ekmekci et al. investigated the effects of shifting one resonator layer away from the other one which are separated from each other and demonstrated a significant shift in the resonance frequency (Ekmekci et al., 2011), and on/off switching (Ekmekci et al., 2015). Lapine, et al. used the reconfigurable unit cell to control the transition resonance frequency by shifting centers of the layers from each other (Lapine et al., 2009). The microelectromechanical systems (MEMS) are also widely used in this field such as moving parts to/from away resonator i.e. reconfigurable unit cells resonator (Zhu et al., 2011), (Zhu et al., 2012). MEMS is sometime used to generate new shape such as: square “[ ]”, square with variable gap “[ ]”, and I shape “[ ]” (Zhu et al., 2011).

Therefore, all the above mentioned methods are based on plane reconfiguration. Another possible way is bending a part of the structure towards the substrate plane. This bending in some designs creates change in capacitance, hence a change in the resonance frequency (Hu et al., 2013). In addition, layer bending is shown to provide very good tuning results, which are according to change in coupling between fields and metallic layers (Valente et al., 2015).

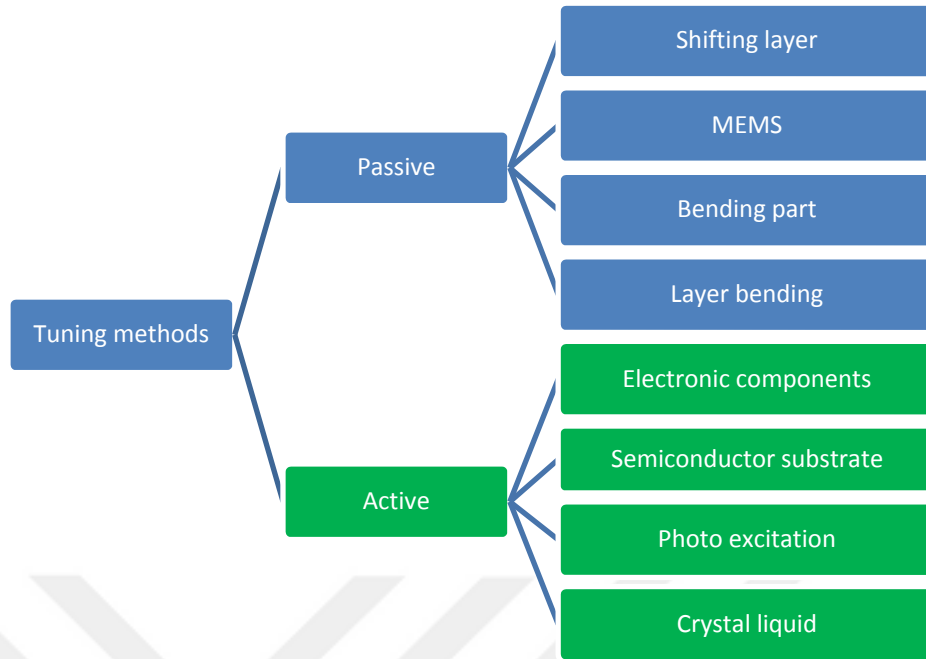


Figure 2.8. Types of tuning methods

In summary, these various tuning methods yield many applications for these sophisticated resonator based structures. The next section presents some applications in a brief description.

## 2.8. Electromagnetic Absorbers and Applications

The electromagnetic absorbers attract the interest of scientists due to their possible wide range of applications in many fields of science and also applicability of the work nearly in all frequency ranges from microwaves to optical region; especially after the revolution of micro and nanostructure materials (Zheludev et al., 2012). However, we can find absorbers in many fields such as energy harvesting applications (Dincer, 2015), antenna gain enhancement (Zhang et al., 2014), clocking (Alaee et al., 2012), electromagnetically induced transparency (EIT) (Shao et al., 2013), (Nakanishi et al., 2015), sensor applications (Wang et al., 2015), switching (Ekmekci et al., 2015).

This section discusses the general applications of electromagnetic absorbers as a quick review. And chapter four present the proposed applications of the Angle Depended Closed Ring Resonator (AD-CRR), which is the product of this thesis.

### **2.8.1. General Review of Electromagnetic Absorbers and Their Applications**

This part present the most popular applications in metamaterials absorber, due to the wide range of applications can be depend on it.

#### **2.8.1.1. Absorber for broadband applications**

For a very long time, scientists have designed broadband EM absorbers, especially for reducing the RCS (Radar Cross Section), because RCS is very important issue in military security applications. If RCS is very small enough, it will make the target almost invisible to radar stations (Dybdal, 1987).

On the other hand, broadband absorbers play a key role in increasing the energy harvesting capacity in many applications such as power transfer to another device in dangerous areas, wireless power charging (Dincer, 2015), (Hawkes et al., 2016), photovoltaic cells to collect energy from natural sources in low price ( Aydin et al., 2011), and electromagnetic shielding (Yang et al., 2014).

#### **2.8.1.2. Absorber for switching applications**

There are methods to control On/Off state (Balamati et al., 2016) ,(Lee et al., 2016), (Ekmekci et al., 2015) have been discussed in the previous section 2.7. There are a lot of applications for switching such as; optical switches, tunable filters (Zhang et al., 2012), and special modulator (He et al., 2014), (Padilla et al., 2006).

#### **2.8.1.3. Absorber for sensing applications**

Many types of sensors can be designed based on absorber structures and the output may be observed through their absorption spectra. Wang B. X. et al.

presented pressure sensor based on changing the substrate thickness, which in turn changes resonance frequency (Wang et al., 2015). A detailed discussion of Pressure sensor will be provided in the following section. Additionally, the absorber structures have also been reported for sensing the thickness of the materials (Al-Naib et al., 2008), (Sabah et al., 2014), and extracting the permittivity (Sabah et al., 2014).

## 2.9. Modeling Methods

There are a few methods for absorber modeling. These modeling can be used to provide useful information about understanding the physical behavior and tools to select parameters for a desired absorber structure design. Thus, some hypothetical methodologies can be exemplified as effective medium theory (Landy et al., 2009), interference theory (Chen, 2012), (Sun et al., 2011), impedance matching theory (Landy et al., 2008), (Watts, et al., 2012), (Ayop et al., 2016), and equivalent circuit model (Pang et al., 2013), (Ghosh et al., 2015). In this work impedance matching method is chosen to explain absorption mechanism. Absorption level tuning is achieved by tuning the effective permittivity and effective permeability of the absorber (i.e. tuning impedance matching see Appendix A), (Landy et al., 2008), (Huang, et al., 2015).

Additionally, suppose uniform electromagnetic plane wave incidents perpendicularly on interface between two different medium (for example free space medium as a surrounding medium and absorber medium see (Figure 2. 9)). Therefore, according to the boundary conditions provided in section 2.3, Appendix A, and (Smith, et al., 2005) the reflection coefficient, transition coefficient, and impedance matching can be written as follows:

$$\Gamma(\omega) = \frac{\eta(\omega) - \eta_0}{\eta(\omega) + \eta_0} \quad (\text{Reflection coefficient}) \quad (2. 26)$$

$$T(\omega) = \frac{2\eta(\omega)}{\eta(\omega) + \eta_0} \quad (\text{Transmission coefficient}) \quad (2. 27)$$

$$Z(\omega) = \sqrt{\frac{(1+\Gamma(\omega))^2 - T(\omega)^2}{(1-\Gamma(\omega))^2 - T(\omega)^2}} \quad (\text{Normalized Impedance matching}) \quad (2.28)$$

Where  $\eta_0$  is the free space intrinsic impedance,  $\eta$  is the absorber medium intrinsic impedance see equation (2.29), and  $Z(\omega)$  in (2.28) represent normalized impedance. Additionally, from the definition of impedance is the ratio between  $E$ -field and  $H$ -field at resonance frequency as explained in Appendix A:

$$\eta(\omega) = \frac{E}{H} = \sqrt{\frac{\mu(\omega)}{\epsilon(\omega)}} \quad (2.29)$$

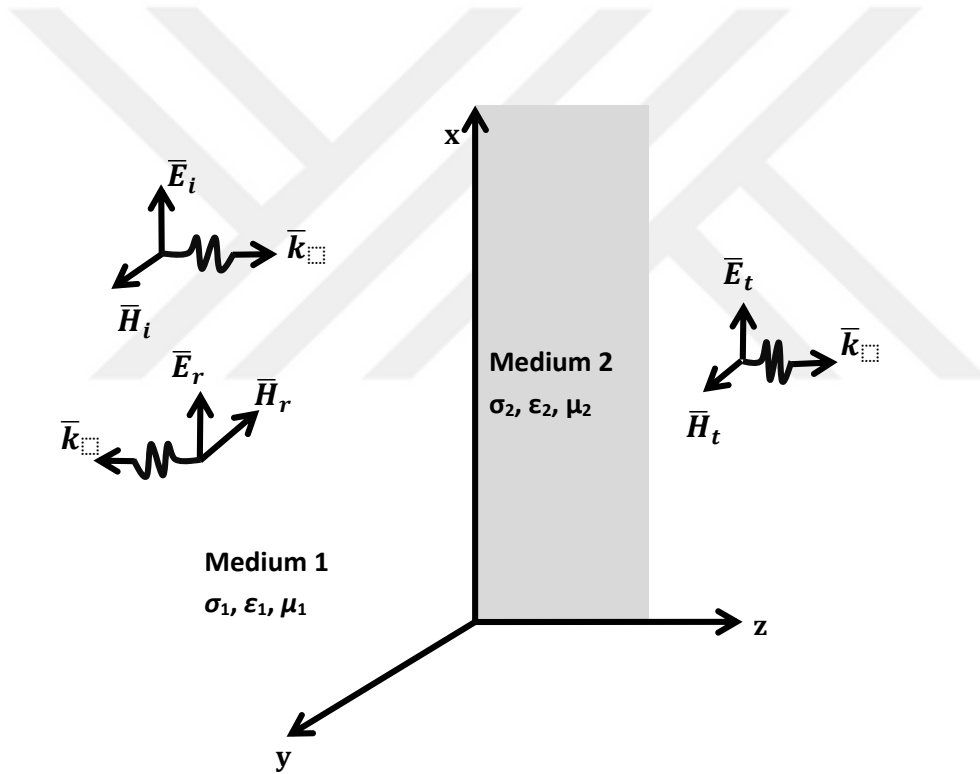


Figure 2.9. Electromagnetic plane wave normal incidence on interface between two different medium, reflection plane wave, and transition plane wave (Cheng, 1993).

Equation (2.29) is frequency depended, so we need to calculate effective permittivity  $\epsilon_r(\omega)$ , and effective permeability  $\mu_r(\omega)$ . Nevertheless, this way is very difficult especially when we use fully metallic ground plane, because the

absorber become anisotropic and inhomogeneous medium (Smith et al., 2005), (Landy et al., 2008), (Singh et al., 2011). Therefore, equation (2. 28) is easier as we will see in next chapter.



### **3. DESIGN, FABRICATION, AND CHARACTERIZATION OF ABSORBER TUNABLE RESONATOR (AD-CRR) STRUCTURE**

This chapter is composed in two parts. In the first part, the design of the suggested structure in CST MWS (Microwave Studio) will be provided with numerical analyses. In the second part fabrication and experimental setup will be described.

#### **3.1. Design**

This section provides a descriptions of simulation environments and methods, simulation tool setup, design dimensions, and material properties.

##### **3.1.1. Simulation environments and methods**

Most of the literature use standard commercial computational software tools to simulate structure before fabrication and experimental studies. These softwares provide good chance to present optimized structure, parametrical studying. In many cases, the experimental results match with the simulation results to a great extent. There are some famous software in this field: Computer Simulation Technology (CST) microwave studio (MWS), COMSOL Multiphysics, and High Frequency Structural Simulator HFSS from ANSYS. Additionally, these simulation tools generally depend on finite element method or finite difference time domain method to numerically analyze the structure. In this work, the software that had been chosen to design and simulation was CST MWS. This software is a full wave electromagnetic solver that uses FIT (Finite Integration Technique) to solve Maxwell's equations (see section 2.2.). Thus, in order to construct a good setup and comment on the results, the fundamental knowledge on boundary condition (BC) mechanism is important. There are two different methods in this field (Watts et al., 2012). The first one is periodic unite cell-boundary condition PUC-BC. In this method, the software analyzer just repeats the unit cell geometry in the same dimension and orientation to make a periodic

array. Hence, the electric and magnetic currents for original unit cells and image unites become in the same phase and directions (see Figure 3. 1).

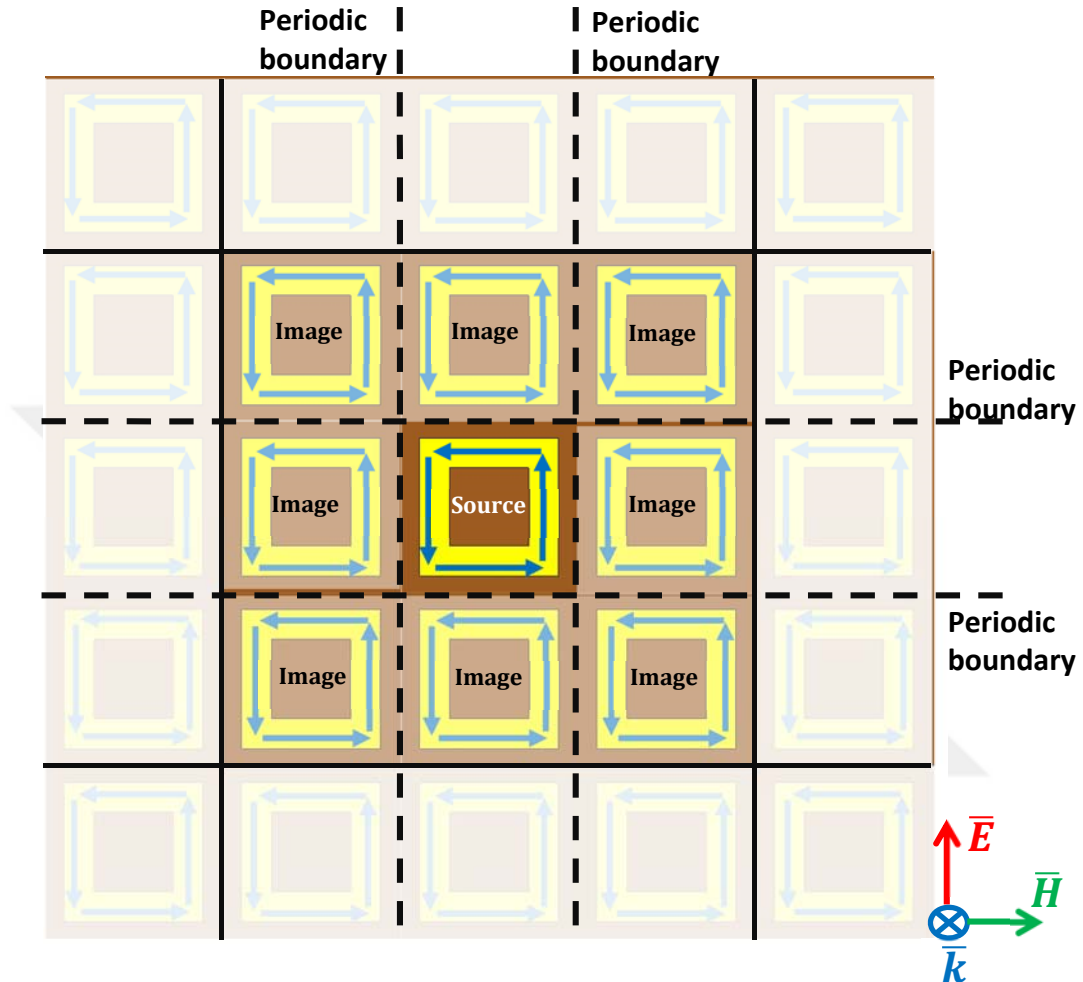


Figure 3. 1. Ring resonator with unite cell periodic boundary condition, when EM wave normal incident on resonator plane.

The second method uses PEC-BC (perfect electric conductor), and PMC-BC (perfect magnetic conductor). This configuration is explained by using image theory (Balanis, 2005) when the electromagnetic wave is normal incident. In PEC boundary case, the electric current flow in original resonator and neighbor image resonator is parallel to each other (original resonator and image resonator). Also, we note  $180^\circ$  phase shift in the electric current flow see Figure 3. 2. But we note  $0^\circ$  phase shift for perpendicular current flow on PEC boundary. In the other hand for PMC boundary case, the electric current flow in

original resonator and neighbor image resonator also is parallel to each other (original resonator and image resonator). But, we note  $0^\circ$  phase shift in the electric current flow see Figure 3. 2.

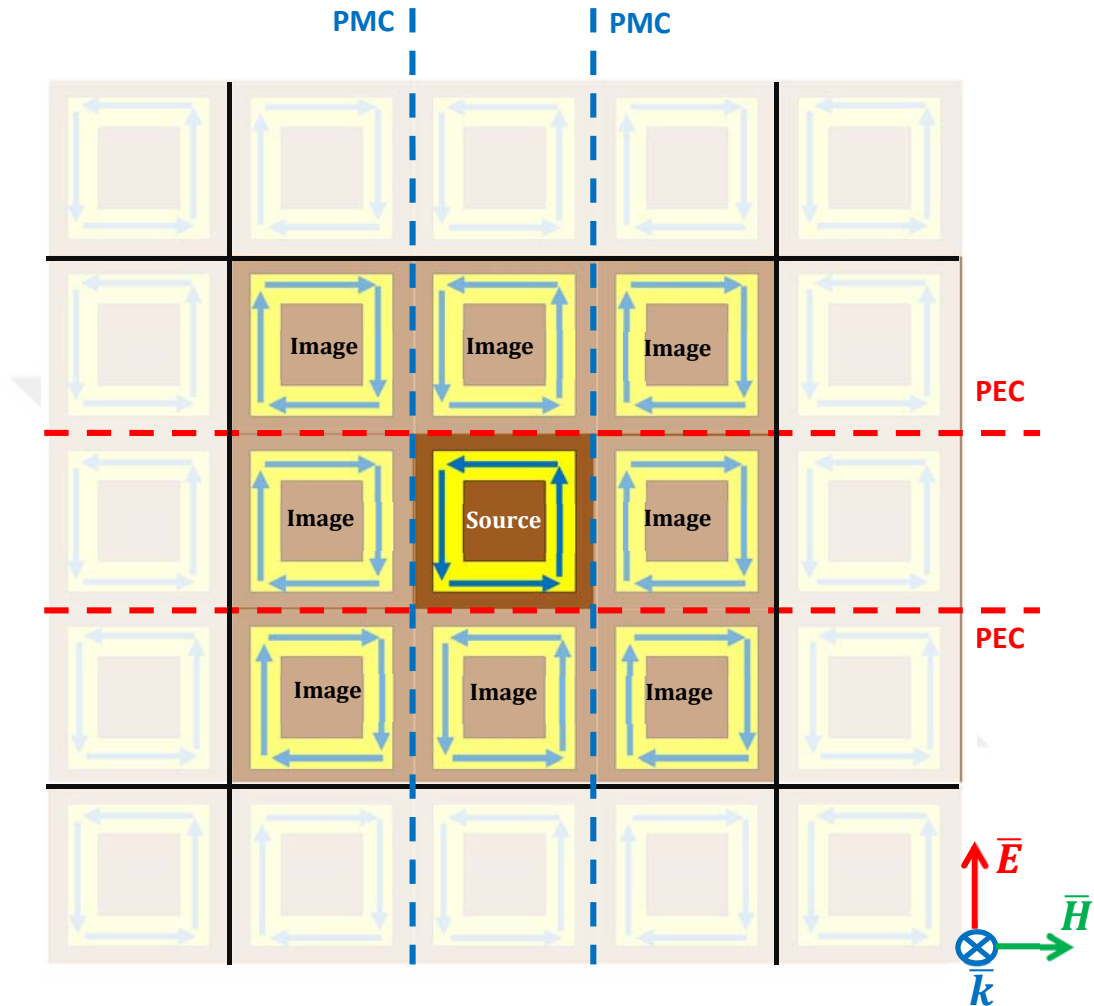


Figure 3. 2. Ring unit cell resonator with PEC and PMC boundary condition, when EM wave normal incident on resonator plane.

### 3.1.2. CST Microwave studio setup

In order to make the simulation and the experiment in a comparable environment the CST setup are chosen as presented in references (Ekmekci et al., 2015). Normal setting was applied for materials in background. The excitation ports are chosen as waveguide ports, where the port one is in  $-z$ -direction and port two is in  $+z$ -direction. The dimensions along  $x$  and  $y$  directions are  $L_x = 72.136$  mm and  $L_y = 34.036$  mm, respectively. Under  $TE_{10}$

mode excitation, the propagation vector  $\bar{k}$  is along  $-z$ -direction,  $E$ -field and  $H$ -fields are along  $y$ -direction,  $x$ -direction, respectively. Additionally, the other four waveguide walls which are perpendicular on  $x$  and  $y$  directions are selected as PEC boundary (i.e.  $E_t = 0$ ). In addition to this, the simulation is applied by using frequency domain solver, with S-band frequency ranges from 2.4 GHz to 4.1 GHz, (see Figure 3. 3).

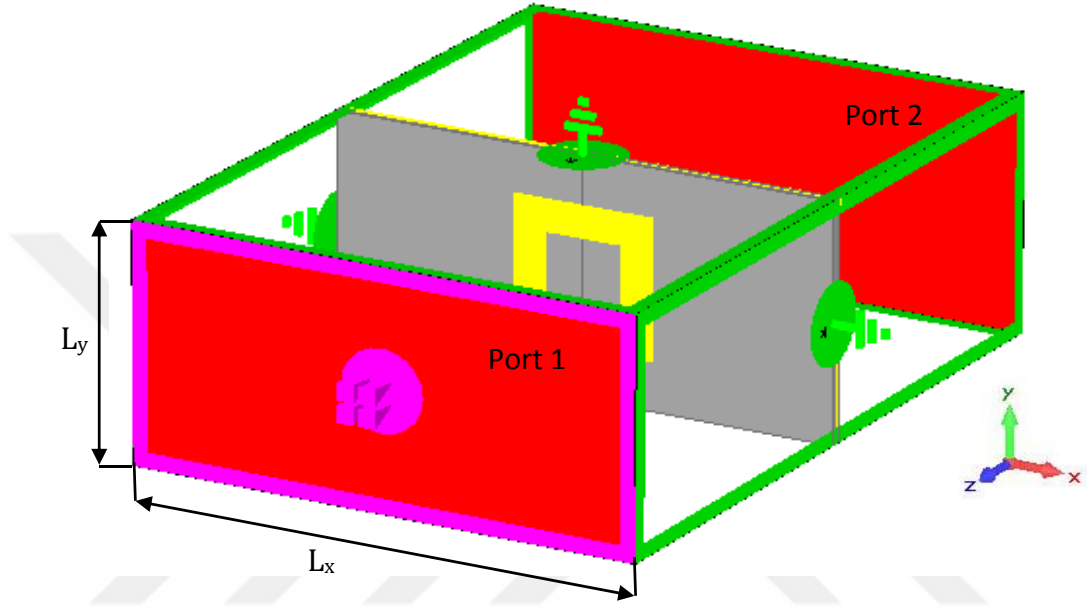


Figure 3. 3. CST simulation setup, green sides represent PEC boundary, port one in  $-z$ -direction and port two  $+z$ -direction

### 3.1.3. Design dimension and materials properties

The proposed design AD-CRR (Angle Dependent Closed Ring Resonator) consists of three layers: Two conductive layers and one FR-4 substrate layer in between the two conductive layers. The top layer consists of a square ring structure with side length  $L_r$  and ring width  $w$ , whereas the bottom layer is total metallic ground plate, in order to cancel any transmission (Ekmekci et al., 2015). The all conductive layers are chosen as lossy copper with electric conductivity  $\sigma = 5.8 \times 10^7 \text{ s/m}$ , and the thickness  $35 \mu\text{m}$ . The FR-4 is chosen as lossy FR-4 with thickness  $h$ , length  $L_x$ , height  $L_y$ , dielectric constant  $\epsilon_r = 4.3$  and tangent loss  $\tan\delta = 0.025$ . See schematic design Figure 3. 4. and dimensions are listed in Table 3. 1. On the other hand, we should refer to the AD-CRR structure is

divided into two symmetrical parts around central  $y$ -axis, with zero distance between them see Figure 3. 4 (c).

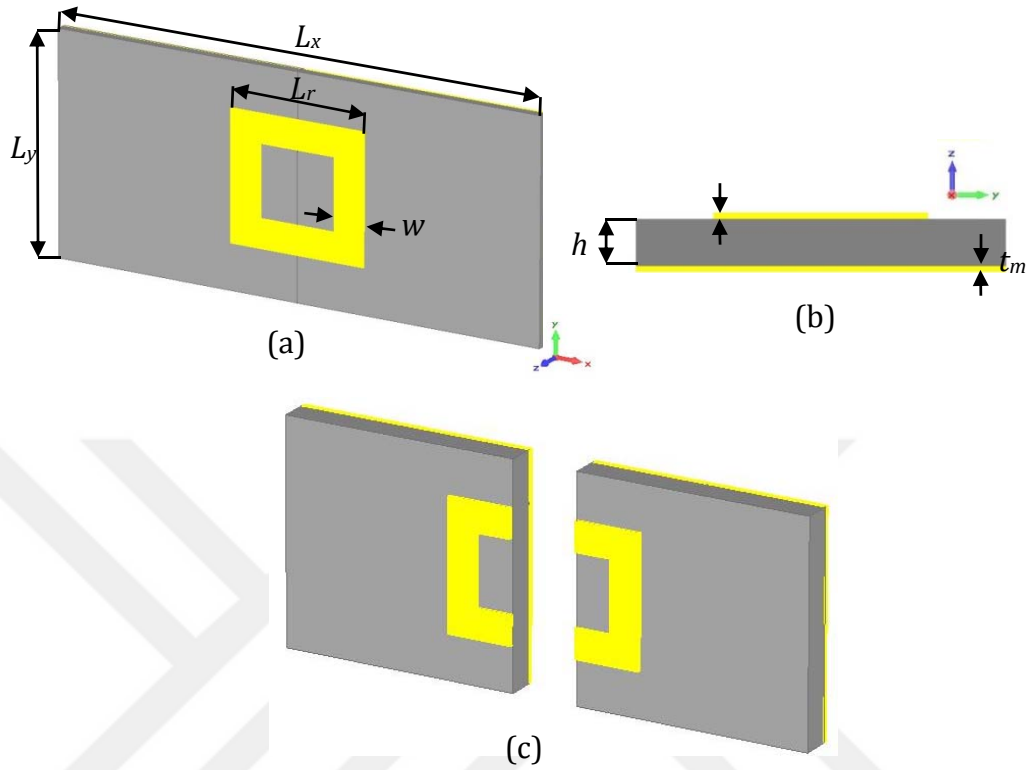


Figure 3. 4. Schematic of AD-CRR. (a) Schematic perspective view, (b) Schematic side view, (c) schematic perspective view two symmetrical parts. (Note that the parts are connected to each other during the simulation and experiments).

Table 3. 1. AD-CRR parameter list.

Parameters	Dimensions (mm)
$L_x$	72.136
$L_y$	34.036
$h$	1.5
$L_r$	20
$w$	4.5
$t_m$	0.035

In order to generate the function of tuning for AD-CRR structure we fold the two parts inward around  $y$ -axis at point  $(0, 0, t_m)$  where:

$$0 \leq \alpha \leq 90^\circ \quad (3. 1)$$

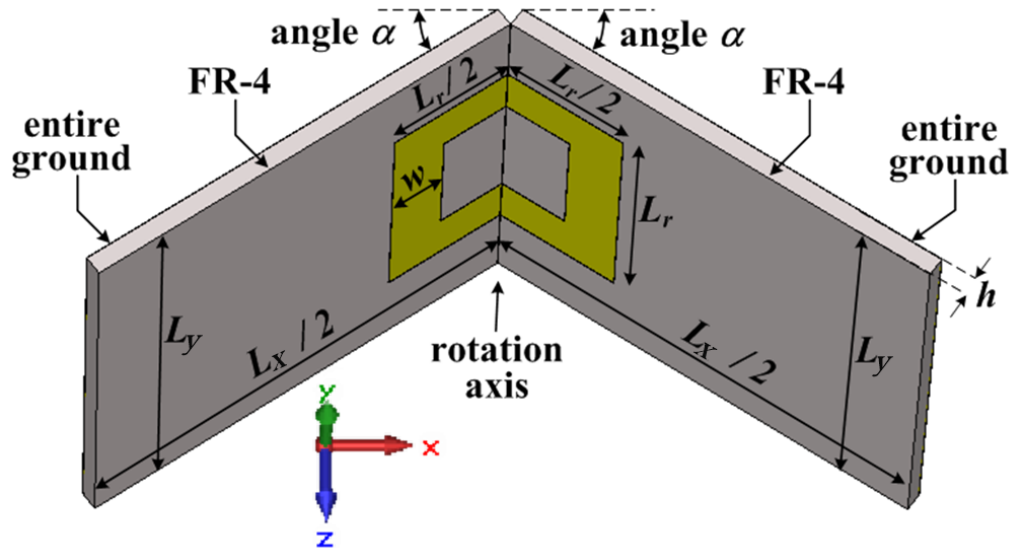


Figure 3. 5. Schematic of perspective view for AD-CRR structure.

## 3.2. AD-CRR Structure Fabrication and Experimental Setup

### 3.2.1. Structure fabrication

In order to verify the simulation results, two half parts of AD-CRR are fabricated using standard printed circuit board (BCP) methods (see Figure 3. 6 (a)). The substrate dielectric constant,  $\tan\delta$ , the copper electric conductivity, and copper thickness, are all same values in section 3.1.3.

All geometric dimensions have also been chosen as the same as presented in Table 3. 1. Additionally, in order to construct angles, AD-CRR is supported by the pink-foam which act like the air medium (i.e.  $\epsilon_r = 1$  and  $\tan\delta = 0$ ). Figure 3. 6 presents photographs taken for  $10^\circ$ ,  $30^\circ$ , and  $60^\circ$  angles respectively as the example.

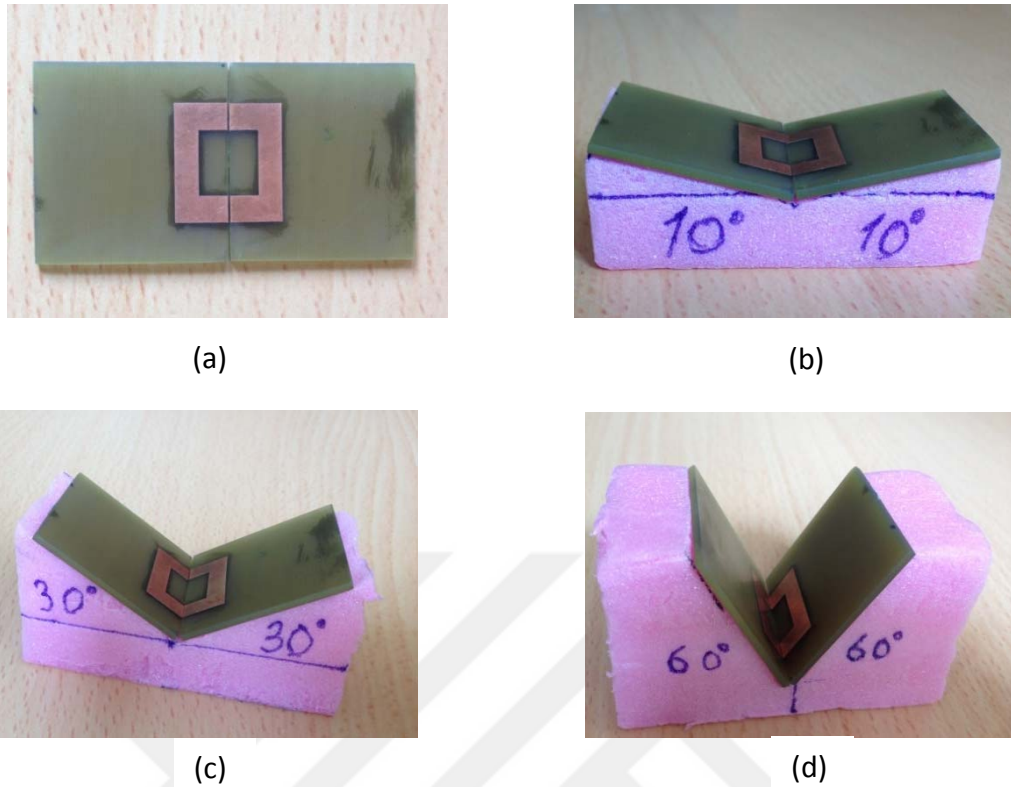


Figure 3. 6. (a) Photograph of two half parts of AD-CRR structure, (b),(c), and (d) Photographs of  $10^\circ$ ,  $30^\circ$ , and  $60^\circ$  respectively.

### 3.2.2. Experimental setup

For the experimental setup, all equipment, devices, and procedure were chosen as presented in reference (Ekmekci et al., 2015). Using two hollow ports rectangular waveguide WR-284 at S-band (from 2.4 GHz to 4.1 GHz), this waveguide was directly connected into two ports of vector network analyzer (VNA) (Agilent Fieldfox N9926A) by coaxial cable. In addition to this,  $\lambda/4$  spacer was used in between two waveguide aperture ports to hold AD-CRR sample. Figure 3.7. presents experimental setup. In addition to complete the measurement setup, the VNA must be calibrated carefully. There are a few techniques for (open ended flanged waveguide) can be used to calibrate, such as: Short Short Load (SSL) is very good calibration technique that provides highly accurate measurements. However, the disadvantage in this setup is that is it a time-consuming method (You et al., 2014). Another highly accurate measurement setup is Thru-Reflect-Line (TRL) calibration kit (You et al., 2014),

(Dunsmore, 2012 ). Herein, the thru means port one is connected directly to port two, reflect means port one and two are shorted, and line means port one is connected with port two through delay “spacer” ( Engen et al., 1979). So, this technique depends on using two ports as it will be used in this work. There are four steps to make TRL calibration Figure 3. 8 presents TRL calibration flowchart.

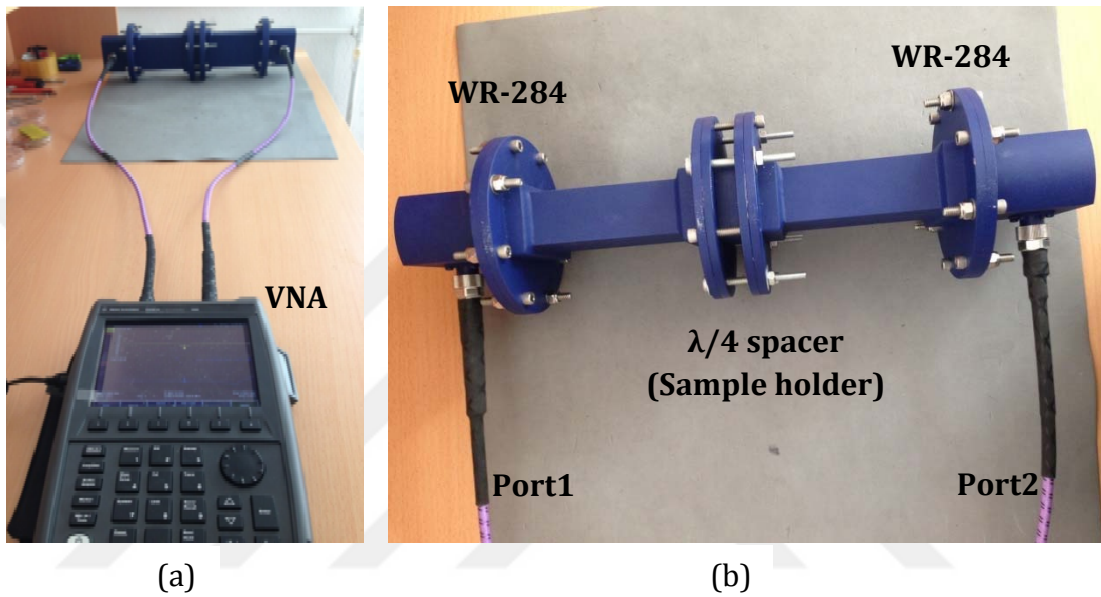


Figure 3. 7. Photographes show the expermental (a) vector network analyzer (VNA) (Agilent Fieldfox N9926A) connected to waveguid, (b) two waveguid ports connected through  $\lambda/4$  spacer (i.e. sample holder)

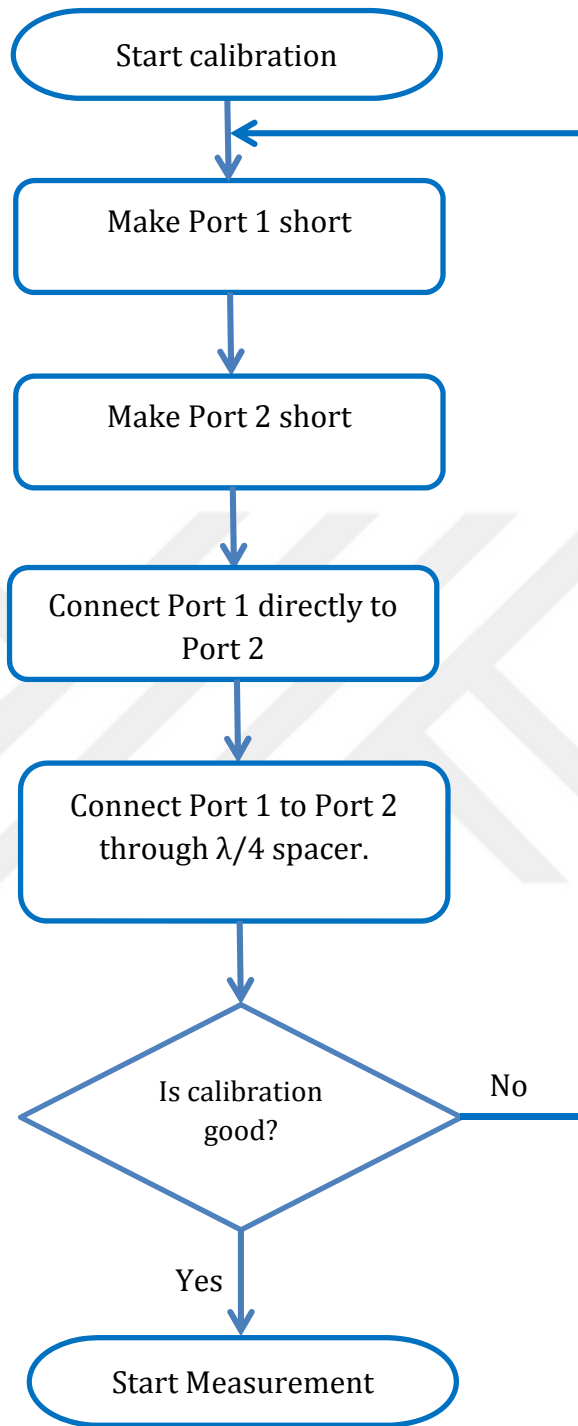


Figure 3. 8. Thru-Reflect-Line (TRL) calibration flowchart

## 4. ANGLE DEPENDENT CLOSED RING RESONATOR (AD-CRR) APPLICATIONS

This chapter investigates some possible applications that can be derived from the suggested design. The Angle Dependent Closed Ring Resonator AD-CRR design consists of two metallic layers (copper) separated by one FR-4 substrate layer. More description about dimensions, materials properties, simulation, and experimental setup can be found in the previous chapter.

### 4.1. AD-CRR Based Pressure/Weight Sensor

The pressure sensor applications of SRR type metamaterial has been investigated by Ekmekci et al. which is based on shifting the resonance frequency by using double-sided split ring resonator (two resonators layer separated from each other by a variable air gap) (see Figure 4.1) (Ekmekci et al., 2013).

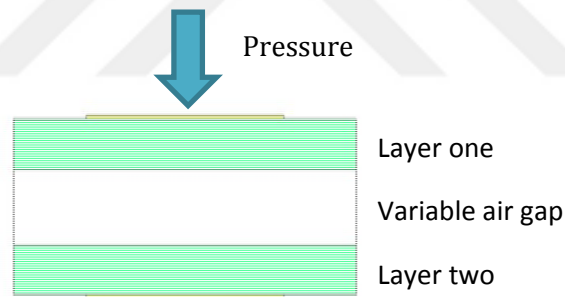


Figure 4.1. Schematic of pressure sensor layer one and two resonator layer, yellow color represent copper green substrate.

The air-gap can be tuned by applying external pressure. Please note, the change in thickness of air gap causing a change in the resonance frequency (Ekmekci et al., 2013). Also, Li et al. investigated tunable sensor based on stretch power. The applied force into sensor cells makes a slight shift between cells, then it cause a change in capacitance and yields a tuning in the resonance frequency. However, the tuning range is very small about 0.8% of resonance frequency, because the high stretch force may crack the metallic resonator (Li et al., 2013). In addition to this, Melik et al. presented strain sensor based on metallic resonator carried

on Kapton tape (polyimide tape or sometimes called vacuum tape) and ground plane. The applied force into sensor is caused decreasing in distance between resonator and ground plane, which means a change the capacitance, and in turn this change leads to a shift in resonance frequency (Melik et al., 2009). In another work by this group, strain sensor, is proposed that uses different types of substrate which are derlin and polyamide (Melik et al., 2010). Additionally, Ekmekci et al. investigated a new method of pressure sensing based on metamaterial absorber by changing the amount of coupling between two layers that are stacked in the z-direction simply by applying a force in bottom resonator's layer to make it move along x-direction. This shift changes the coupling, hence the resonance frequency (Ekmekci et al., 2011).

It is also possible to use AD-CRR structure for pressure sensing purpose. Applying a pressure yield a change in the folding angle. This angle change also changes the electromagnetic wave interaction with the structure and changes the absorption level. This mechanism is summarized in Figure 4.2.

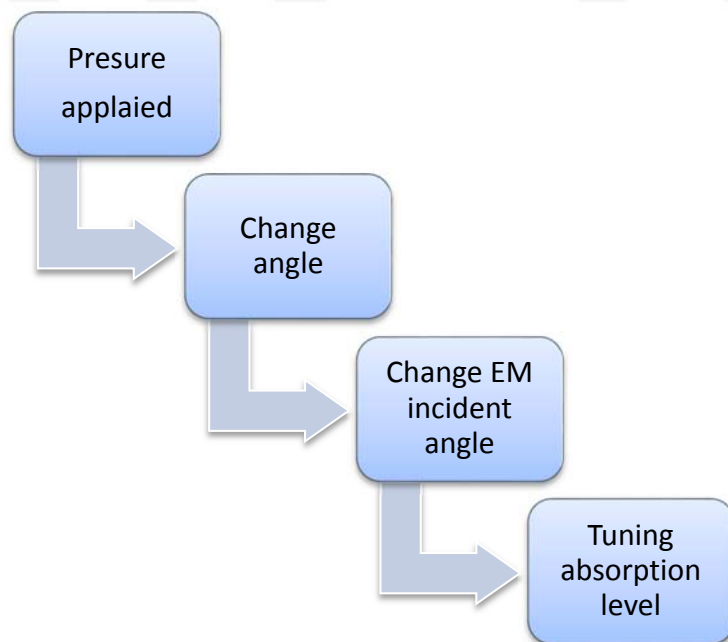


Figure 4.2. State process of AD-CRR based on pressure sensor

## 4.2. AD-CRR Based ON-OFF Switching

In many applications, it is important to tune the states between ON and OFF. For example:

- Controlling between reflection (ON) and absorption (OFF) (Ekmekci et al., 2015) see (Figure 4.3).
- Controlling between transmission (ON), and absorption (OFF) (Shadrivov et al., 2015).
- In metamaterial applications the switching between RH (Right Handed medium) and LH (Left Handed medium),
- In some applications of antenna switching between deferent types of polarization horizontal or vertical (Capolino, 2009).

However, there are many researches in this field which present various methods about ON/OFF switching in microwave, THz and optical region. In the meanwhile, due to change in absorption level of the AD-CRR design, it can be used for ON/OFF switching between reflection and absorption, as we will see in the next chapter. This mechanism is explained in Figure 4. 3.

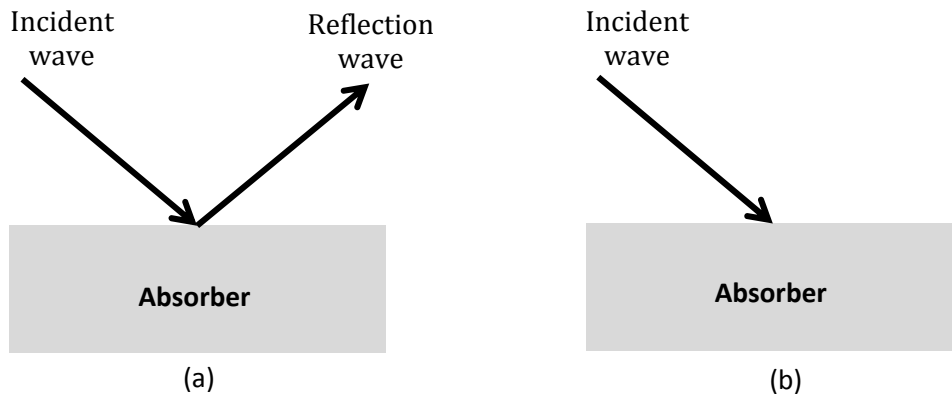


Figure 4.3. ON/OFF switch based on absorber, the switch convert between reflection and absorption state (a) ON- state reflection, and (b) OFF state absorption.

### 4.3. AD-CRR Based Absorber Modulator

In all communications systems, the modulator takes an important place due to the role it plays. Many modulation methods are used to modulate information for example AM (amplitude modulation), FM (frequency modulation) and PM (phase modulation). Additionally, the growth in optical communication imposed to creation of very high-speed devices that match the speed between optical and electronic devices, optical storage, optical modulator transmitter, and receiver (Zheludev et al., 2012). Metamaterial absorber based modulator is one of the greatest solutions to this problem. In many recent studies, scientists suggested different absorber modulators. For example Savo et al. accomplished THz-FM modulator based on orientation in liquid crystal (Savo et al., 2014). Another FM tuning method based on MEMS cantilevers by Pitchappa et al. presents controlling capacitance by adjusting the distance between cantilever and ground plate to achieve frequency tuning (Pitchappa et al., 2015). FM modulator is also achieved by breaking the symmetry of through shifting the layer (Zhu et al., 2012), (Hsing Fu et al., 2011 ), (Zhu et al., 2011).

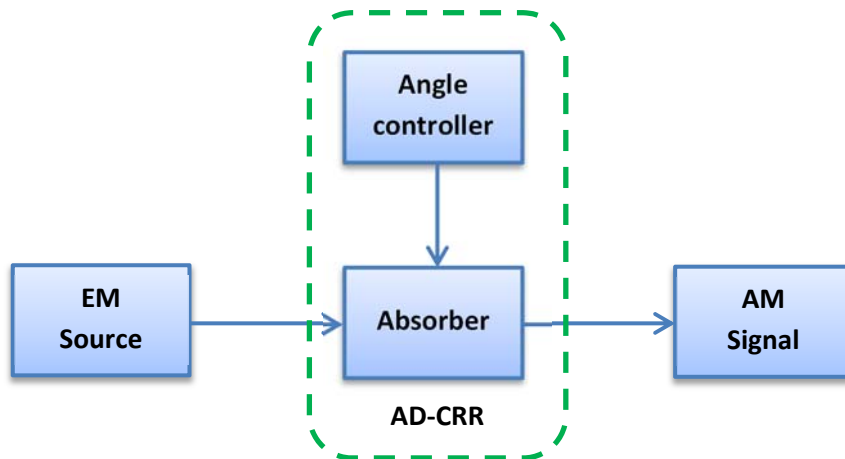


Figure 4.4. AM modulator structure

On the other hand, AM modulator has also received wide attentions in literature. Ou et al. explored a resonator based on metal bowing. They applied an external voltage to increase the temperature of free moving metal, which in turn causes

this metal to bow so it contacts with another constant metal. Hence, MEMS-tuning control the distance between these two metallic layers to control the absorption level (Ou et al., 2013). Using the same method, AM modulator achieved at infrared band by Liu et al (Liu et al., 2015). Padilla et al. reported that using Gallium arsenide (GaAs) substrate and changing GaAs tangent loss by applying voltage, they got an AM modulator (Padilla et al., 2006).

Then in accordance with the compatible work between AD-CRR design and AM modulator function, the AD-CRR can be used as AM modulator by controlling the rotation angle to handle change in absorption level see Figure 4.4.



## 5. RESULTS AND DISCUSSION

In this chapter, the absorption characteristics of AD-CRR are investigated in a comparative way between full wave electromagnetic simulation, and experiment results to figure out the AD-CRR advantages. The numerical calculations are obtained by using CST MWS studio the full wave electromagnetic simulation. The experiment results are obtained by using hollow rectangular waveguide and measured by using Agilent Fieldfox N9926A vector network analyzer. The information about simulation setup and experimental setup is illustrated in chapter 3. Herein, the absorption level, reflection level, transition level and resonance frequency are obtained from the scattered S-parameter matrix for different rotation angles values.

### 5.1. Simulation Results

The AD-CRR geometrical dimensions, materials properties, and simulation setup are presented in chapter 3. The first step in this study is to investigate the absorption characteristic spectrum  $A(\omega)$  at  $\alpha = 0^\circ$ . Then, the absorption dependent on frequency can be directly calculated from frequency dependent reflectance  $R(\omega)$  and transmittance  $T(\omega)$  (Smith et al., 2005), (Tao et al., 2008), (Landy et al., 2009). These values were carried out from S-parameters  $|S_{11}|^2$ , and  $|S_{21}|^2$ , respectively by using equation in section (3.3). Where  $|S_{21}| = 0$ , according to use completely copper ground plane (Ayop et al., 2014), (Ekmekci et al., 2015). Since, the updating form for equation (3.3) is only dependent on reflectance  $R(\omega)$  as we see in equation (5. 1):

$$A(\omega) = 1 - R(\omega) = 1 - |S_{11}|^2 \quad (5. 1)$$

Figure 5. 1 presents the reflectance and absorption of AD-CRR structure. Where, the electromagnetic wave is TE<sub>10</sub> mode, and normal incident onto surface of absorber is as shown in Figure 3. 3. This structure is provided resonance frequency at 2.811 GHz, zero transmission, and  $|S_{11}| = -9.195$  dB (0.347 in linear scale). Then, the total absorption from equation 5.1 is 0.879 (unit less).

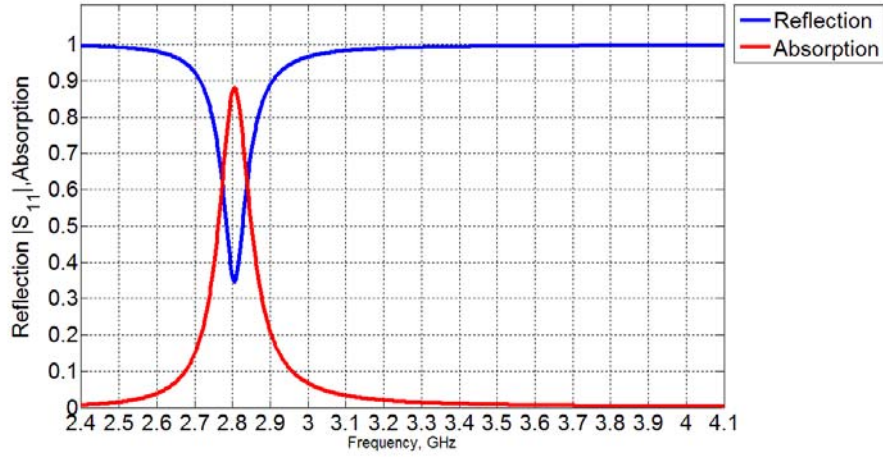


Figure 5. 1. Absorption and reflection spectra for AD-CRR at  $\alpha = 0^\circ$

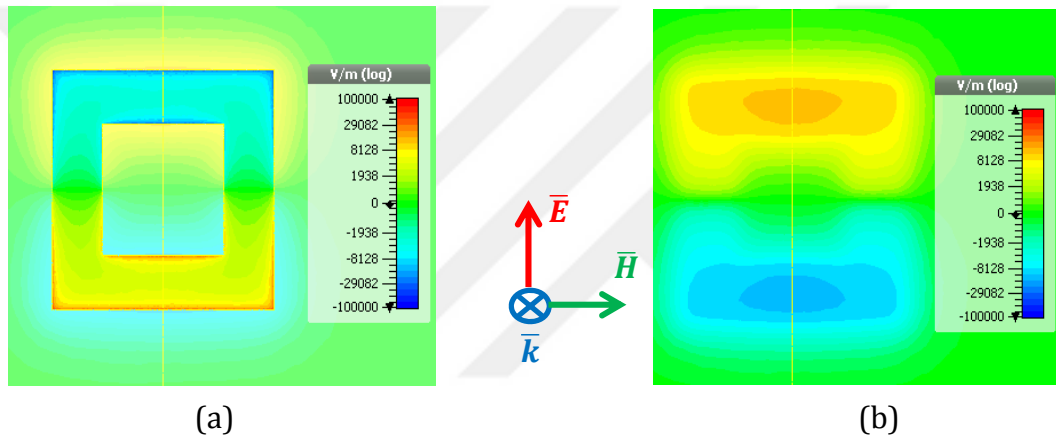


Figure 5. 2. z-component of electric field distribution for E-field along y-axis at resonance frequency 2.811GHz, (a) for ring, and (b) for ground plane.

In order to gain insight regarding the absorption reasons and mechanism in AD-CRR, three types of simulation were carried out by CST microwave studio, electrical field monitoring, magnetic field monitoring, and surface current distribution at resonance frequency (2.811 GHz). (Figure 5. 2 a, and b) present electric field at different reference points plane. We can figure out two different charges distribution at the two end of ring along y-axis direction, which is according to logarithmic color bar ranging from 0 V/m to 67006 V/m see Figure 5. 2(a). Also, the opposite electric field distribution simultaneously occurs onto ground copper (see Figure 5. 2 (b)), where, the high coupling occurs between ring and ground. Therefore, it is stated that the difference in electric field

direction is referred to the ring which works like an electric dipole resonator (Hu et al., 2013), (Luo et al., 2011).

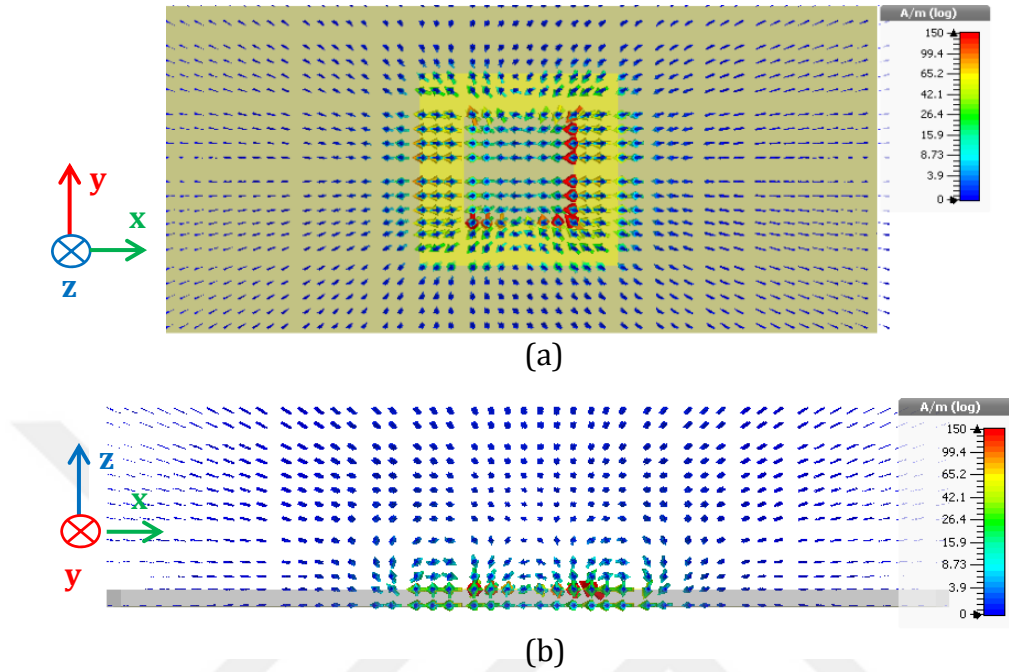
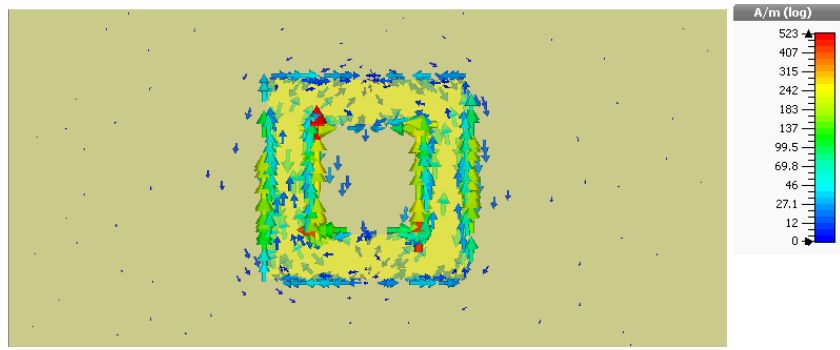


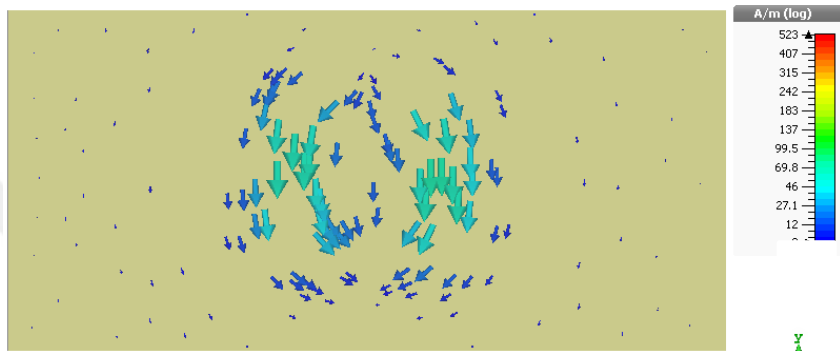
Figure 5.3. Magnetic field distribution for H-field along x-axis at resonance frequency 2.811 GHz, (a) top view in (xy-plane), and (b) side view in (xz-plane)

In the other hand the magnetic field distribution also proved the same point. There is a very high circulating magnetic field between the two metallic layers (Tao et al., 2008), (Zhu et al., 2010) (Cheng et al., 2012). See Figure 5. 3 (a, and b), top view (xy-plane), and side view (xz-plane) in order, at the same logarithmic bar colors.

Figure 5. 4. presents opposite current distribution between upper ring Figure 5. 4(a), and lower ground plane Figure 5. 4(b) which proved that the type of resonance is an electrical dipole resonance.



(a)



(b)

Figure 5. 4. Surface current distribution for at resonance frequency 2.811 GHz, (a) ring, and (b) ground plane.

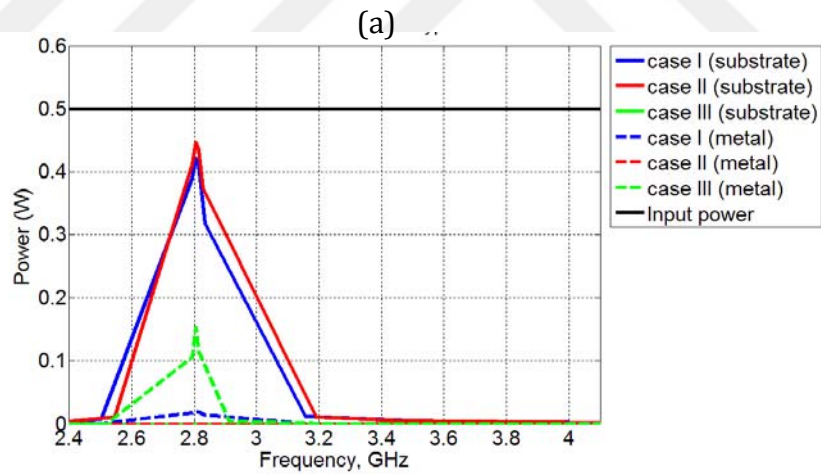
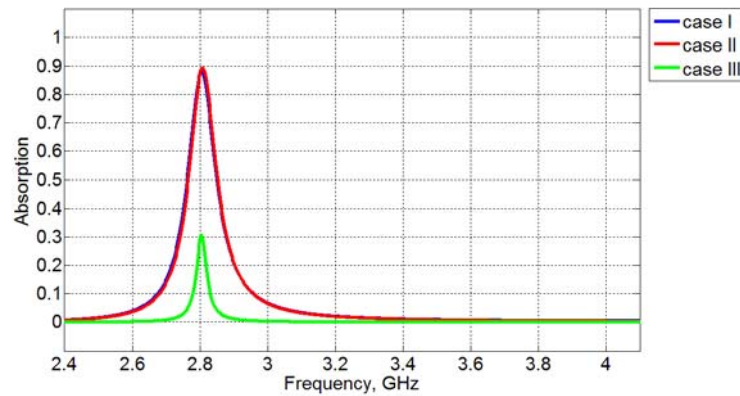
### 5.1.1. Absorption reasons

In order to investigate the reasons of absorption we need to figure out the loss in each part of resonator as an unaccompanied structure (ring, substrate, and ground plane). For this reason, three types of simulation carried out by CST for each case listed in Table 5.1. Herein ‘case I’ is the factual state as presented previously in Figure 5.1. In ‘case II’ the all metals are chosen as lossless materials in order to study the effect of substrate only (see Figure 5.5. a, and b). Lastly ‘case III’, the substrate is chosen as lossless (Figure 5.5. a, and b). Therefore, we can figure out that the main power losses come from substrate since, the power is dissipated as heat or ohmic losses inside the substrate and the copper can be supposed as PEC (perfect electrical conductor) in microwave regain (Fedotov et al., 2007), (Lee et al., 2016). This result is fully coherent with

previous studies for circular ring absorber (Nguyen et al., 2014), cut-wire metamaterials absorber (Do et al., 2012).

Table 5.1. Three different cases

State	Ring	ground	substrate
case I	Lossy metal	Lossy metal	Lossy dielectric
case II	PEC	PEC	Lossy dielectric
case III	Lossy metal	Lossy metal	Lossless



(b)

Figure 5. 5. Three cases of table 5.1, (a) absorption as a function of frequency, and (b) power as a function of frequency

### 5.1.2. Impedance matching

In chapter 2, there are mentioned a few methods to model absorber structures (see section 2.9). In this thesis, the impedance matching is used to explain the absorption mechanism, in order to explain and understand the reason behind

the absorption. The maximum absorption (perfect absorption PA) occurs when the absorber impedance at resonance frequency is equal to impedance of surrounding medium (Landy et al., 2009), (Huang et al., 2013). The complex normalized impedance value follows the next equation (Smith et al., 2005), (Baskey et al., 2015):

$$\mathbf{Z} = \sqrt{\frac{(1+S_{11})^2 - s_{21}^2}{(1-S_{11})^2 - s_{21}^2}} \quad (5.2)$$

Also,  $|S_{21}| = 0$ ,  $\alpha = 0^0$  then:

$$\mathbf{Z} = \frac{1+S_{11}}{1-S_{11}} \quad (5.3)$$

Figure 5. 6 shows the real and imaginary parts for  $Z$ , the maximum absorption occurs at minimum positive imaginary point (Baskey et al., 2015).

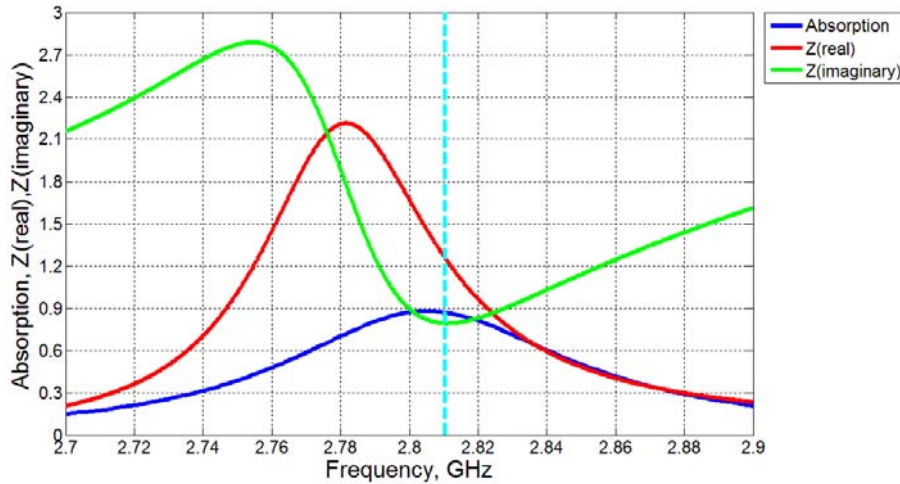


Figure 5. 6. Calculated normalized impedance and absorption plots. The dashed line is set at resonance frequency 2.811 GHz.

### 5.1.3. Multi-reflection interference theory

Multi-reflection interference theory is analyzing methods that are used to describe the mechanism of the metamaterial absorber depend on superposition of multiple reflections from absorber structure, due to use multiple layers that have different reflective index factors (Huang et al., 2015). The multi-reflection

interference theory is good way to describe the structure with ground plane. In the other hand the impedance matching theory and effective medium theory are not suitable to describe the interactions between absorber and ground plane (Wanguang et al., 2013).

In appendix B, the mathematical formulas are provided in details to calculate total reflection. To apply these functions, some additional setups and practical considerations are needed, that are presented in some studies (Chen 2012), (Wanguang et al., 2013), (Huang et al., 2015). The total reflection for sandwich absorber (two metallic layers bounded one substrate) is defined as follows:

$$R_{\text{total}} = |S_{11}|e^{i\phi_{11}} + \frac{|S_{12}||S_{21}|e^{i(\theta_{12}+\theta_{21}-2\beta-\pi)}}{1-|S_{22}|e^{i(\phi_{22}-2\beta-\pi)}} \quad (5.4)$$

In order to obtain parameter values for equation (5.4) from CST, the structure should be simulated in decoupled consideration, which is applied by removing the ground plane, and attaching port 2 directly to structure (Dincer et al., 2014). In addition to this,  $|S_{12}| = |S_{21}|$ , and  $\theta_{12} = \theta_{21}$  because the substrate is passive layer, therefore we can rewrite the equation above:

$$R_{\text{total}} = |S_{11}|e^{i\phi_{11}} + \frac{|S_{12}|^2 e^{i(2\theta_{12}-2\beta-\pi)}}{1-|S_{22}|e^{i(\phi_{22}-2\beta-\pi)}} \quad (5.5)$$

Where:

$$\beta = \frac{2\pi}{\lambda_0} nd = \frac{2\pi f}{c} nd$$

$$n = \sqrt{\varepsilon_2 \mu_2} = \sqrt{4.3 \times 1} = 2.074, \text{ (for FR4 } \varepsilon_2 = 4.3, \mu_2 = 1)$$

$$\theta_{12} = \sin^{-1} \left( \sqrt{\frac{\varepsilon_1 \mu_1}{\varepsilon_2 \mu_2}} \sin(\theta_i) \right) = 0, \text{ (} \theta_i = 0^0)$$

$$d = h \cos \left( \sin^{-1} \left( \frac{\sin(\theta_{12})}{\sqrt{\frac{\varepsilon_2 \mu_2}{\varepsilon_1 \mu_1}}} \right) \right) = h = 1.5, \text{ (h is FR4 substrate thickness).}$$

$$\beta = 2\pi \times 3.11 \times \frac{f}{c}$$

After extracting data and applying the above function, the results in Figure 5.7 and Figure 5.8 are obtained, where the  $(\omega) = 1 - R(\omega) - T(\omega)$ , where  $T(\omega) = |T_{total}|^2 = 0$ , and  $R(\omega) = |R_{total}|^2$  calculate from equation (5.5)

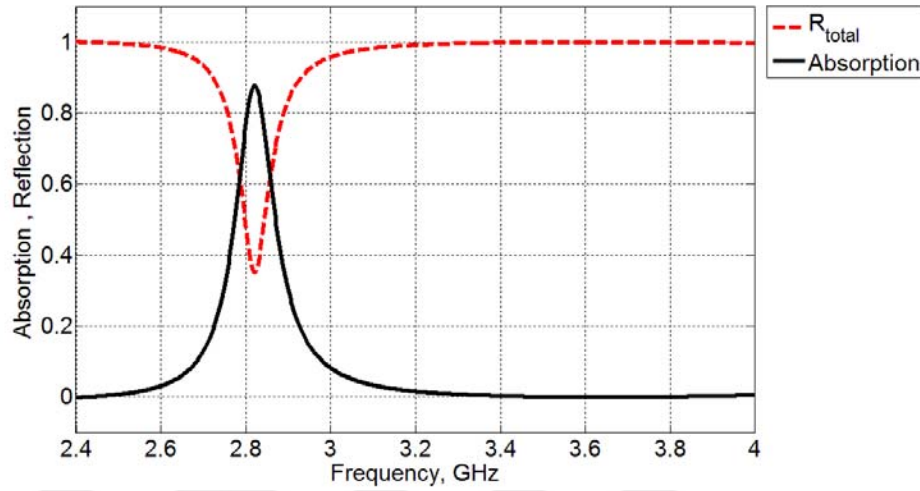


Figure 5.7. Calculated absorption and reflection in normal incident consideration by using interference model

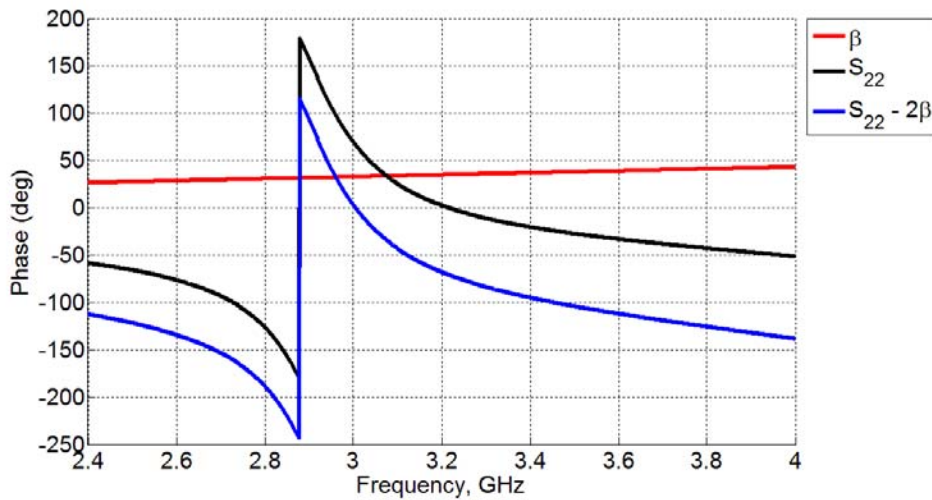


Figure 5.8. Calculated propagation phase in normal incident consideration by using interference model

#### 5.1.4. Effects of changing angle $\alpha$ on absorption spectrum

The main part of this work concentrates on the effects of angle  $\alpha$  on absorption level. Figure 5.9. shows the absorption levels for various  $\alpha$  values ( $0^\circ$ ,  $10^\circ$ ,  $20^\circ$ ,  $30^\circ$ ,  $40^\circ$ ,  $50^\circ$ , and  $60^\circ$ ), where when the angle is higher than  $60^\circ$  the absorption

level is almost zero. Here, the absorption levels are tabulated in Table 5.2. Additionally  $|S_{11}|$  and  $|S_{21}|$  are also presented in Figure 5.10 and 5.11, respectively. It is important to note here that the range of frequency interval is set to be from 2.7 GHz to 2.9 GHz, because there are no other absorption peaks observed for this design in S-band region and besides, narrow frequency range is useful to observe the small details.

These results reveal that when the rotation angle increases, both the reflection level and transmission levels increase. However the transmission levels take values around zero. On the other hand, the absorption decreases dramatically with the increased angle  $\alpha$ . The relation between angle and the absorption peak is observed to be almost linear (see Figure 5. 12). For example: at a constant resonance frequency 2.811 GHz (the resonance frequency at  $0^\circ$ ), the results yield the line equation which is a function of angle  $\alpha$  as given in (5. 6):

$$A = -0.016 \times \alpha + 0.98 \quad (5. 6)$$

Additionally, the reason behind the decrease of absorption level may be explained by the decreases in the circulating currents between the two metallic layers (the ring and the ground) that is generated by H-field. This result is highly compatible with the previous studies reported in literature. For example: Tao, et al. designed insensitive wide-angle range (from  $0^\circ$  to  $70^\circ$ ) metamaterial absorber. They got above 70% absorption peak in TE mode (Tao et al., 2008). Similarly, Ye, et al., presented Omni-directional absorber and they got near 80% absorption peak (from  $0^\circ$  to  $70^\circ$ ) in TE mode (Ye et al., 2013). In these previous studies, the researchers suggested that a decrease in absorption levels represents a disadvantage point for absorber. On the other hand, this disadvantage represents the key point of this thesis work.

Furthermore, Figure 5.13, shows the H-field component by using xz-cutting plane at  $y = 0$ . It is worth noting that the increase in rotation angle significantly decrease in circulating current, where the maximum at  $\alpha = 0^\circ$  (see Figure 5.13 (a)) (note: according to the color bar blue color is set for 0 A/m, and red color is set to 75 A/m), and minimum value noted at  $60^\circ$  (blue arrow) Figure 5.13 (g).

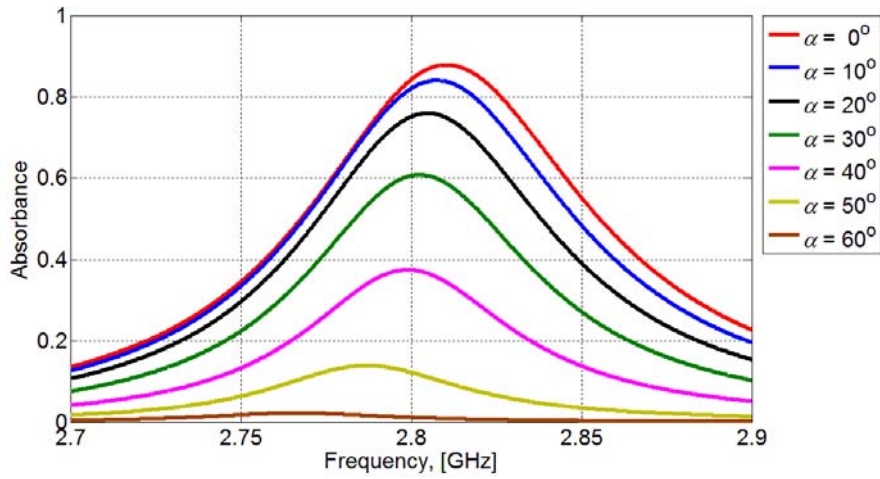


Figure 5.9. Simulation result for absorption level related with changing in rotation angle ( $\alpha$ )

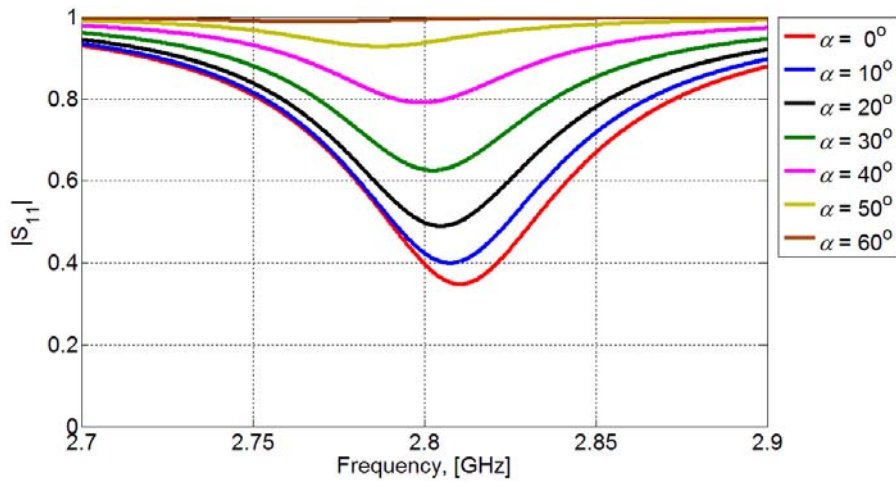


Figure 5.10. Simulation result for Reflection coefficient  $S_{11}$  with respect to frequency

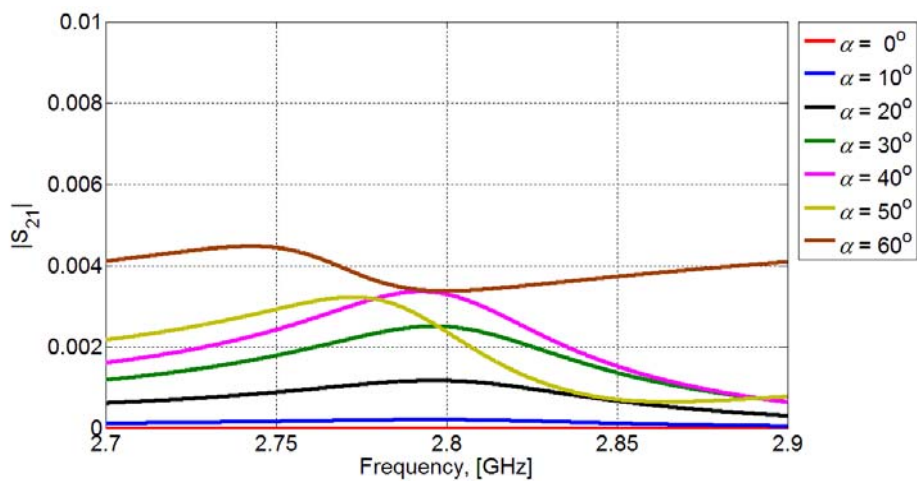


Figure 5.11. Simulation result for transition coefficient  $S_{21}$  related with frequency.

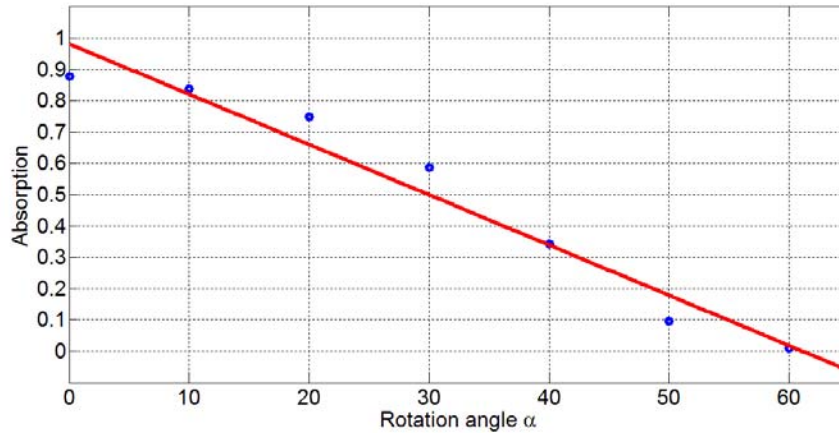


Figure 5. 12. The relation between angles and absorption peaks, (red-line) linear fitting curve according to equation  $A=-0.016 \times \alpha +$

In addition to this, the numerically calculated data for surface current, E-field, and H-field are tabulated in Table 4. 2 for each rotation angle at the resonance frequency. We can also see increasing angle causing gradually change in maximum surface current clearly (from 1208 A/m to 37.3 A/m) for  $0^\circ$  and  $60^\circ$  respectively. Similar behavior goes for E-field and H-field.

Table 5.2. Relation between change in angle and (resonance frequency, maximum surface current, maximum E-field, and maximum H-field)

Angle	Resonance frequency (GHz)	Absorption level	Surface current (A/m)	E-field (V/m)	H-field (A/m)
$0^\circ$	2.811	0.879	1208	250000	1210
$10^\circ$	2.808	0.841	1083	232000	1082
$20^\circ$	2.806	0.760	991	212200	993
$30^\circ$	2.803	0.608	941	169219	943
$40^\circ$	2.800	0.375	695	138033	695
$50^\circ$	2.794	0.139	203	29457	199
$60^\circ$	2.781	0.022	37.3	6399	35.7

Table 5.2 also shows that there is a little shift in resonance frequency related with rotation angle (from 2.811 GHz at  $0^\circ$  to 2.781 GHz at  $60^\circ$ ). Then, the difference is  $\nabla f = |f_{0^\circ} - f_{60^\circ}| = 2.811 - 2.781 = 30$  MHz. Table 5.3, shows the simulation resonance frequency shift based on the angle  $\alpha$  varying between  $0^\circ$  and  $60^\circ$  with step value  $10^\circ$ . Consequently, the shift increases rapidly after  $40^\circ$ .

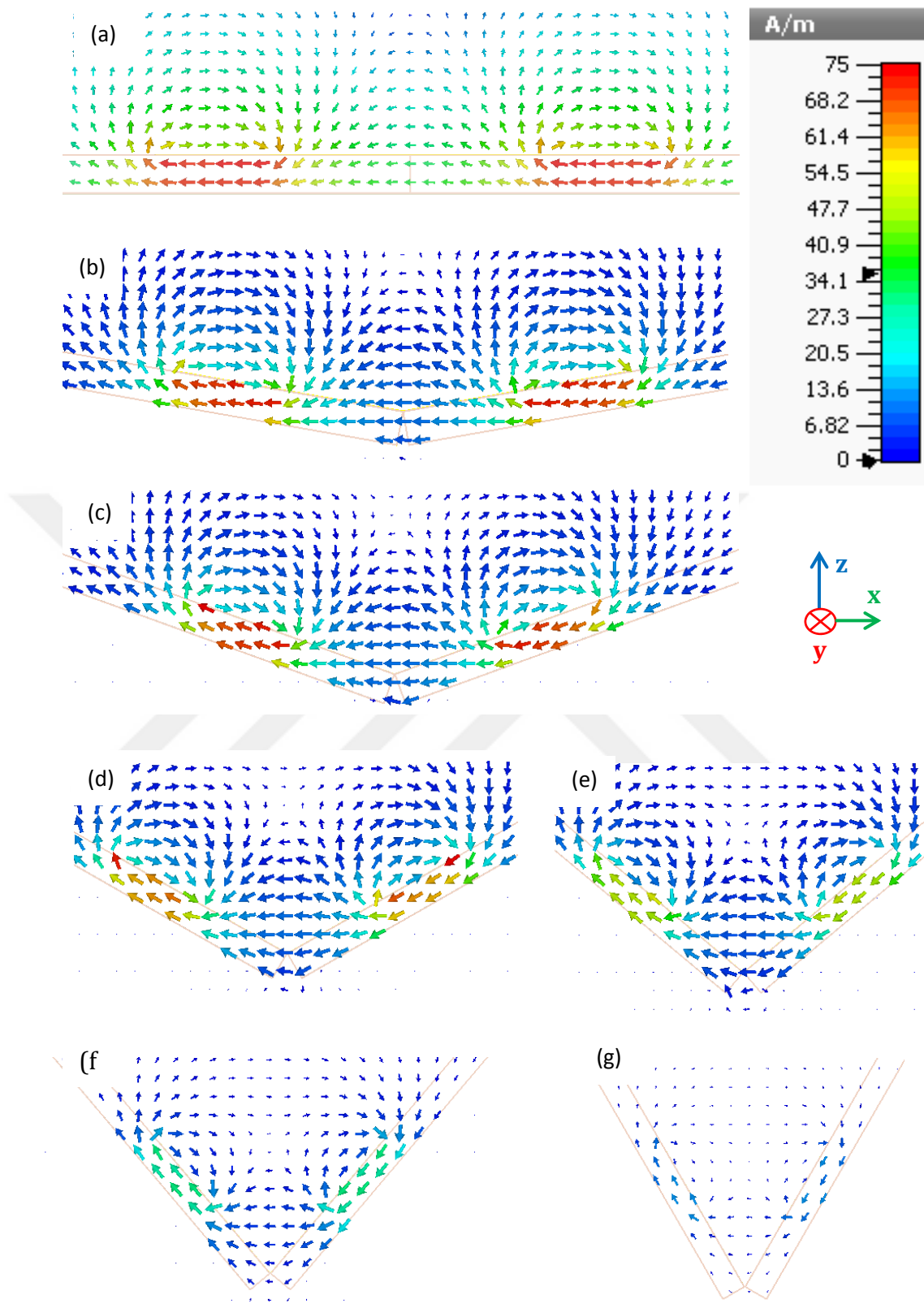


Figure 5. 13.  $H$ -field components obtained by using  $xz$ -cutting plane at  $\mathbf{y} = \mathbf{0}$ , (a)  $\alpha = 0^\circ$ , (b)  $\alpha = 10^\circ$ , (c)  $\alpha = 20^\circ$ , (d)  $\alpha = 30^\circ$ , (e)  $\alpha = 40^\circ$ , (f)  $\alpha = 50^\circ$ , and (g)  $\alpha = 60^\circ$

$$f_{res.} = \frac{1}{2\pi\sqrt{LC}} \quad (5.7)$$

This function tells us that any change in  $L$  and/or  $C$  cause changes resonance frequency. So in next sub section 5.1.3.1 we will see the mechanism behind the change in  $L$ , and  $C$ .

Table 5. 3. The shift in resonance frequency according to angle step

$\nabla\alpha$ (degree)		$\nabla f$ (MHz)
$0^0$	$10^0$	2
$10^0$	$20^0$	2
$20^0$	$30^0$	3
$30^0$	$40^0$	3
$40^0$	$50^0$	6
$50^0$	$60^0$	13

### 5.1.3.1. Explanation for the rapid decreases in absorption level

In many studies in literature, also summarized in section 5.1.3, the absorption peak decreases slowly as the angle of incident wave increases for TE mode. Such slow decrease suggested to be supporting the main aim of this subject: “wide angle and polarization insensitive absorber”. For example He X. J. et al., examined two peaks absorber by using metallic square ring, and metallic cross inside the ring. They achieved a very high angle-insensitive absorber (He et al., 2011). Huang X. et al., also, investigated triple band polarization insensitive and wide incident wave independent absorber in TE polarization and concluded that the lowest absorption peak was achieved 80% at angle  $60^0$  (Huang et al., 2013).

In order to explain the reasons behind the change in absorption peak level and resonance frequency, a new absorbing material design, Central Angle Rotation Dependent Closed Ring Resonator CAR-CRR, is introduced. Herein the material properties and geometrical parameters were kept as the same in Table 3. 1. However, the only change in CAR-CRR design is that the structure is completely rotated around the  $y$ -axis as shown in Figure 5. 14. Herein the rotation angle is defined as  $\phi$ . The absorption results for the rotation angle-steps  $\phi = 0^0, 10^0, 20^0, 30^0, 40^0, 50^0$ , and  $60^0$  are calculated to be 0.879, 0.8715, 0.847, 0.798, 0.714,

0.583, and 0.404 and the resonance frequencies in GHz are found to be 2.810, 2.809, 2.809, 2.808, 2.808, 2.807, and 2.808, respectively. The maximum shift between  $0^\circ$  and  $60^\circ$  is 2.6 MHz see Figure 5.15 and Table 5.4. One can see that the absorption level decreased slowly as rotation angle increased. On the other hand, the shift in the resonance frequency was smaller than the shift in AD-CRR (see Figure 5.9.). Therefore, we can conclude that the results of the CAR-CRR are highly agreement with previous studies reported in literature.

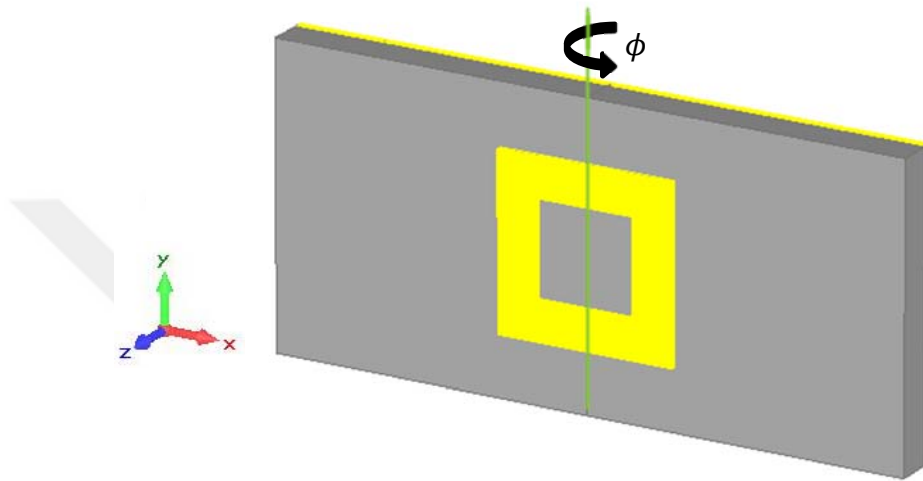


Figure 5.14. Absorber structure for CAR-CRR, all geometrical dimensions similar to Table 3. 1. The all structure parts rotate as one part.

Table 5. 4. Shift of resonance frequency related with rotation angle for CAR-CRR design.

$\nabla\phi$ (degree)		$ \nabla f $ (MHz)
$0^\circ$	$10^\circ$	0.12
$10^\circ$	$20^\circ$	0.4
$20^\circ$	$30^\circ$	0.4
$30^\circ$	$40^\circ$	0.6
$40^\circ$	$50^\circ$	0.4
$50^\circ$	$60^\circ$	0.4
$0^\circ$	$60^\circ$	2.6

Furthermore, the E-field simulation of AD-CRR and CAR-CRR were presented in Figure 5. 17. The figure presents x-component of E-field (a-g) for CAR-CRR, and (f-n) for AD-CRR. Additionally, Figure 5.18 presents z-component of E-field (a-g) for CAR-CRR and (f-n) for AD-CRR.

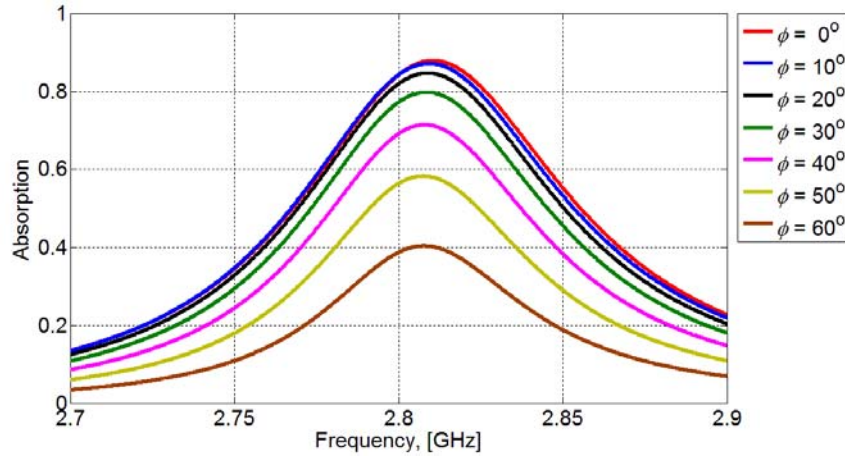


Figure 5. 15. Absorption related with rotation angle for CAR-CRR design.

These results clearly show the difference between two structures in response to the applied electromagnetic wave (Note: all figures are reported by using a common color bar). One can observe that there no induced x-component of local E-field (i.e. the field observed after excitation) on both structures for  $0^\circ$ , however there are strong local E-field z-components, which play role in electrical dipole resonance and hence absorption. Hence, this result is not surprising as seen in Figure 5. 17 (a), (b), and Figure 5. 18(a), (b). In a CAR-CRR, when the rotation angle starts increasing, x-component of the local E-field starts increasing systematically. In the other hand, the z-component starts decreasing, because of the rotation will generate two components for z. The first one ( $E_z \sin(\alpha)$ ) is parallel to structure plane with no effect (like x-component at  $0^\circ$ ). The second component ( $E_z \cos(\alpha)$ ) is perpendicular onto structure plane. Therefore, increasing in angle results with decreasing in  $E_z \cos(\alpha)$  (see Figure 5. 18 (a)-(g)). Conversely, there are two components for x that work in opposite directions. One component has no effect that is parallel to structure ( $E_x \cos(\alpha)$ ). The second one is perpendicular on to structure plane ( $E_x \sin(\alpha)$ ). So, as rotation angle increases the x-component increases, too (see Figure 5.17(a)-(g)). Therefore, the total field can be calculated through:  $E_z \cos(\alpha) + E_x \sin(\alpha)$ .

Furthermore, AD-CRR structure showed very interesting results especially with x-component. There are four different charge distribution generated by the electric field Figure 5. 17 (i)-(n). Therefore to investigate the underlying reason, a vectors analysis is generated for electric field x and z components (see Figure

5. 16). Then, the perpendicular components onto each resonator parts are as following:

$$\mathbf{E}_{total} = -E_z \cos(\alpha) + E_x \sin(\alpha) - E_x \cos(\alpha) \quad (5.8)$$

$$\mathbf{E}_{total} = E_z \cos(\alpha) - E_x \sin(\alpha) - E_x \cos(\alpha) \quad (5.9)$$

Where (5.8) describes right side resonator part, and (5.9) describes left side, therefore the change in polarization of  $E_x$  generates four capacitance instead of two capacitance as we showed in CAR-CRR, also increasing rotation angle make  $E_x$  dominate.

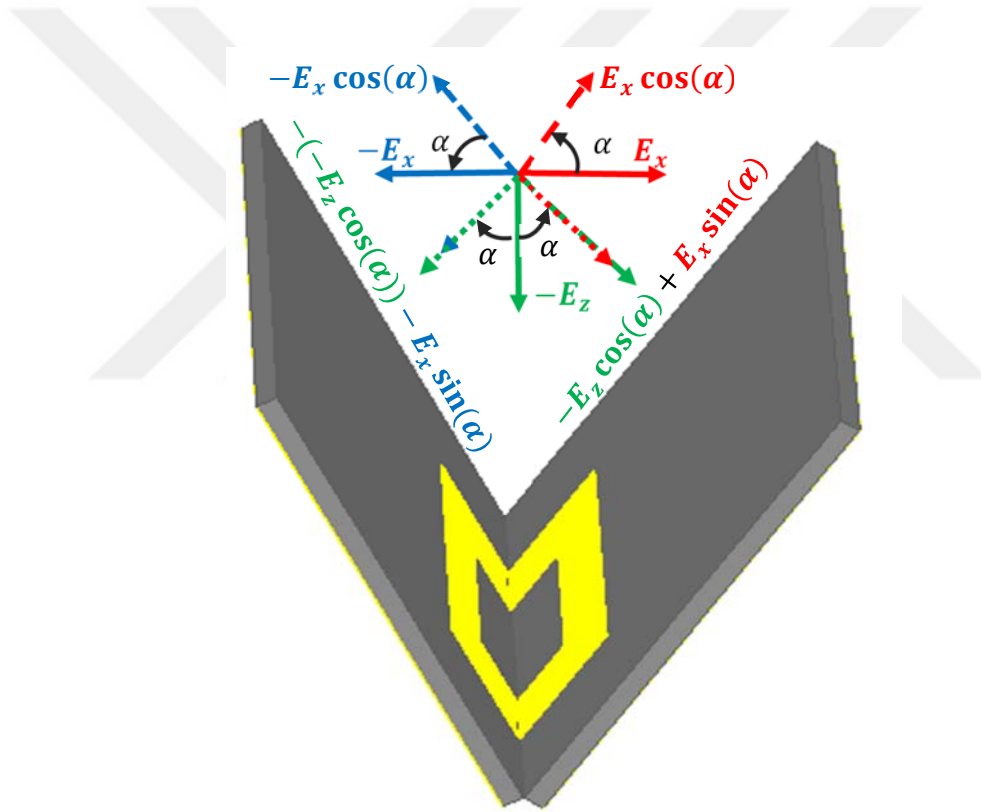


Figure 5. 16, vector analysis for  $E_x$ , and  $E_z$ .

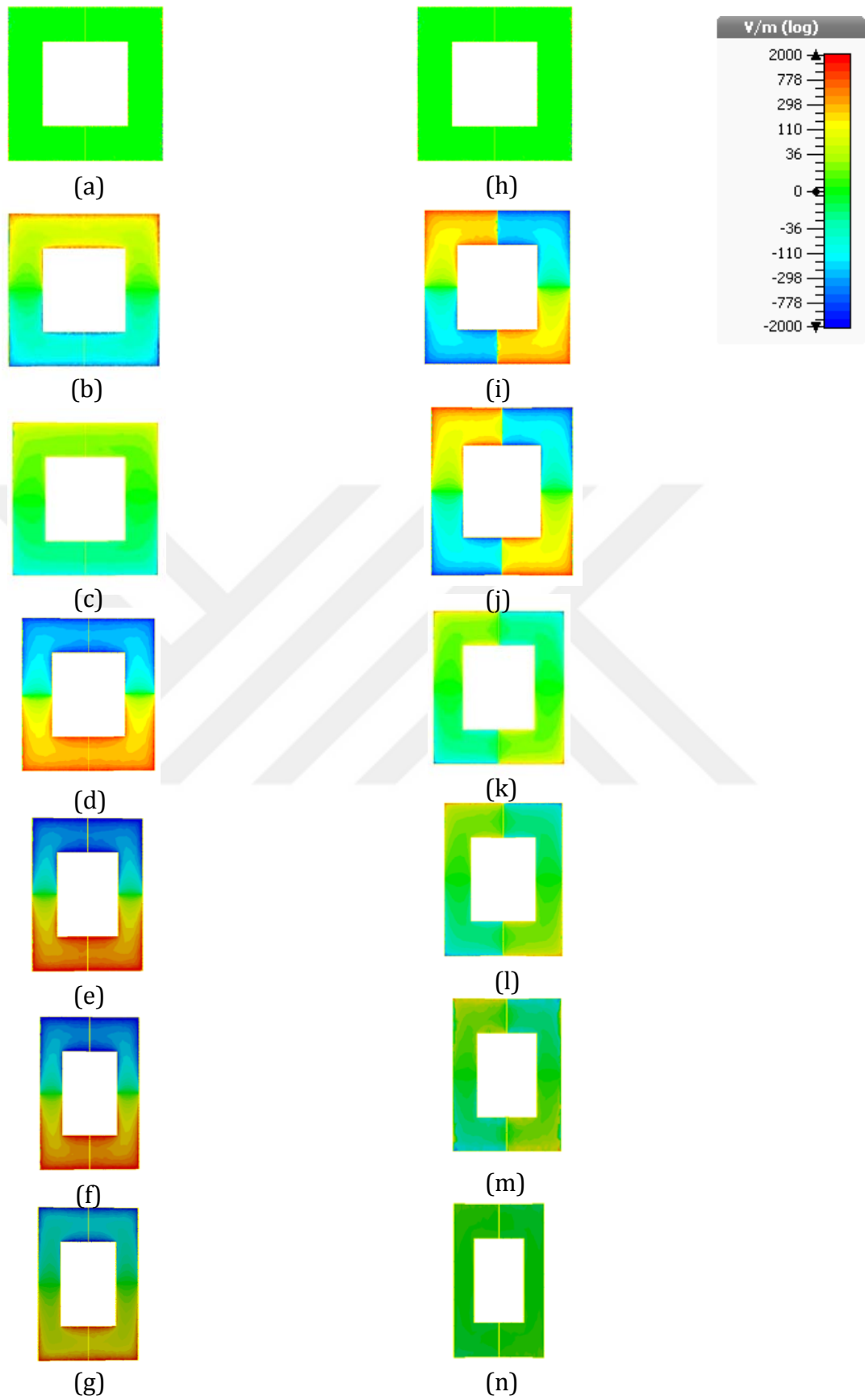


Figure 5. 17. E-field x-component (a-g) for CAR-CRR, and (f-n) for AD-CRR structure, for each rotation angle  $0^\circ$ ,  $10^\circ$ ,  $20^\circ$ ,  $30^\circ$ ,  $40^\circ$ ,  $50^\circ$ , and  $60^\circ$  respectively.

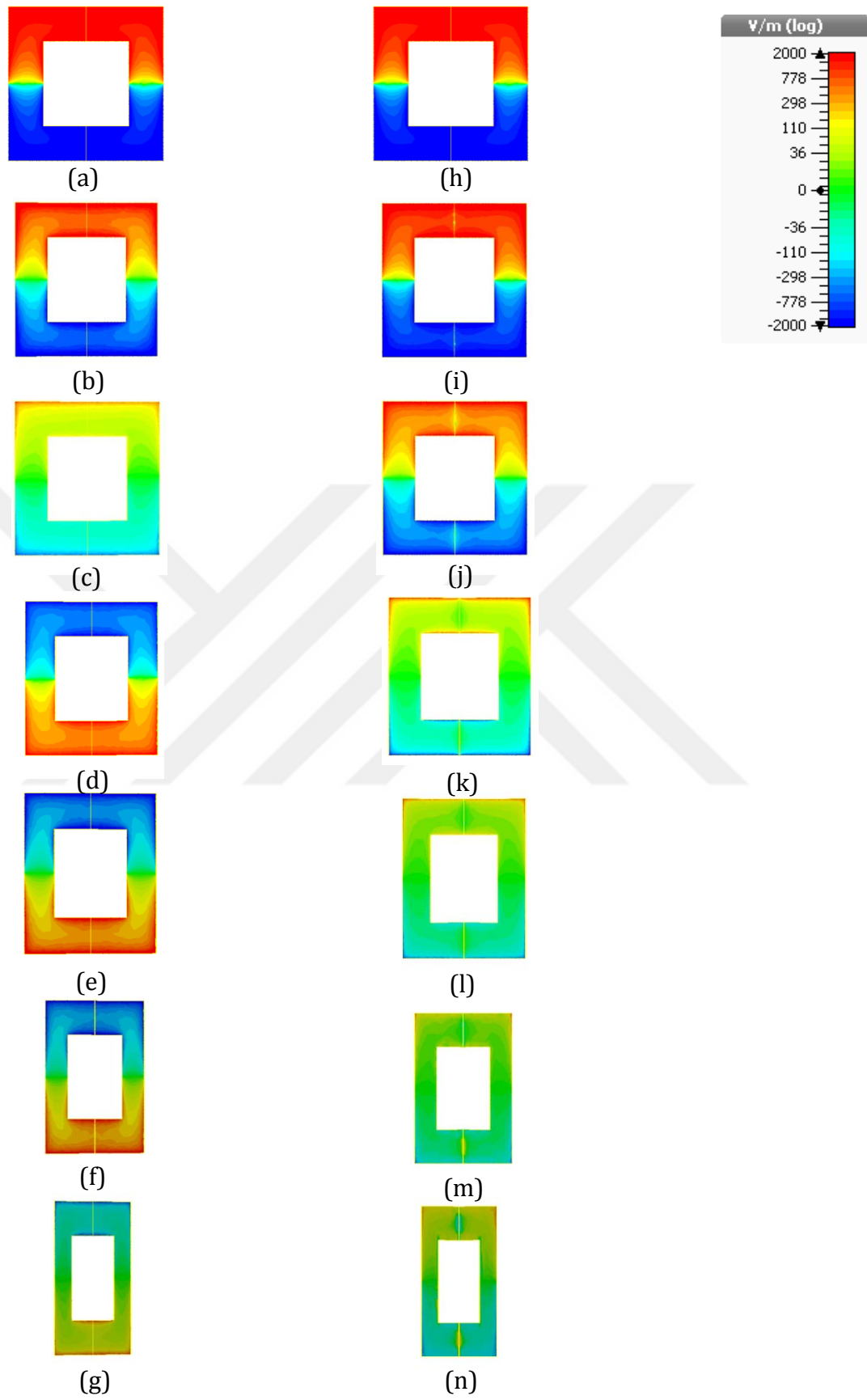


Figure 5. 18. E-field z-component (a-g) for CAR-CRR, and (f-n) for AD-CRR, for each rotation angle  $0^\circ$ ,  $10^\circ$ ,  $20^\circ$ ,  $30^\circ$ ,  $40^\circ$ ,  $50^\circ$ , and  $60^\circ$  respectively.

## 5.2. Experimental Realization

According to previously description of experimental setup in chapter 3, the suggested AD-CRR is fabricated by using standard printed circuit board technology. Then seven experimental results for the seven angles are carried out. Figure 5. 19, Figure 5. 20, and Figure 5. 21 show absorption,  $|S_{11}|$ , and  $|S_{21}|$  experimental results, respectively for all designed rotation angles. The experimental results show high compatibility with the simulation results except for some little differences. It is worth to note that the absorption levels of experimental result slightly differs from absorption levels of simulation, for all rotation angles. For example: The absorption increased from 0.879 to 0.957 at  $0^\circ$  (where  $\nabla A = 0.078$ ). At  $60^\circ$  is increased nearly the same as previous  $\nabla A$  value from 0.022 to 0.060 ( $\nabla A = 0.038$ ) (see Table 5.5. for all designed angles). On the other hand, one can observe that experimentally obtained  $|S_{11}|$  values also agree with simulations (see Figure 5.20). However, although experimentally obtained  $|S_{21}|$  values seems to be a bit different from simulation, the transmitted power is still near to zero since the transmitted power is measured with  $|S_{21}|^2$ , where the maximum transmission noted 0.054 at resonance frequency in  $60^\circ$ .

Furthermore, the resonance frequency change is imperceptible, where the maximum change noted as 11 MHz at  $60^\circ$ . In addition to this, the difference in results may drive from three points:

1. Structure fabrication tolerance is slightly different from structure in simulation.
2. The FR4 substrate parameters (dielectric constant and tangent loss) may be slightly different from selected parameters in simulation. In next sub section, we will see the influence of these parameters in more details.
3. Angle resolution. Due to laboratory limitations, angle constructed from foam manually (i.e. by using human hand). Therefore, it may cause a slight difference in one or two angles side increasing and/or decreasing.

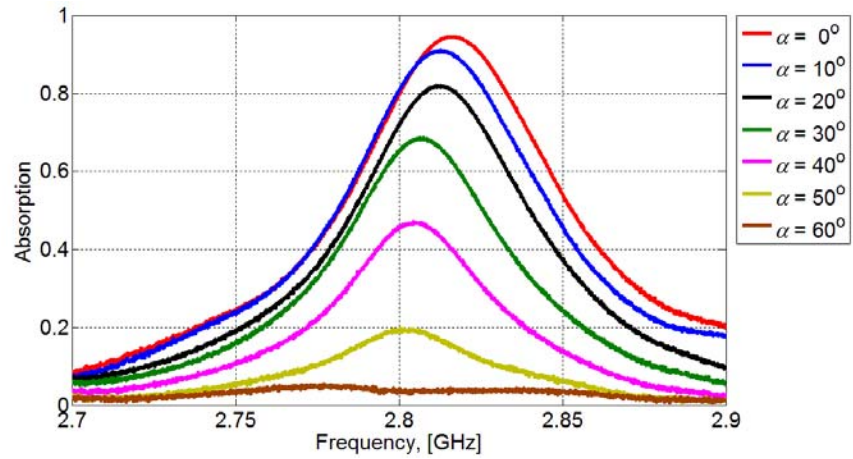


Figure 5.19. Experimental result for absorption level related with changing in rotation angle ( $\alpha$ )

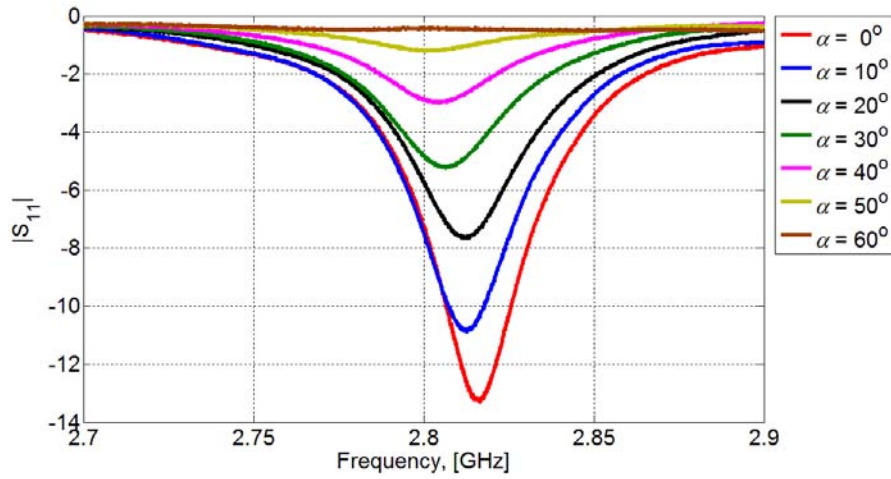


Figure 5.20. Experimental result for reflection level related with changing in rotation angle ( $\alpha$ )

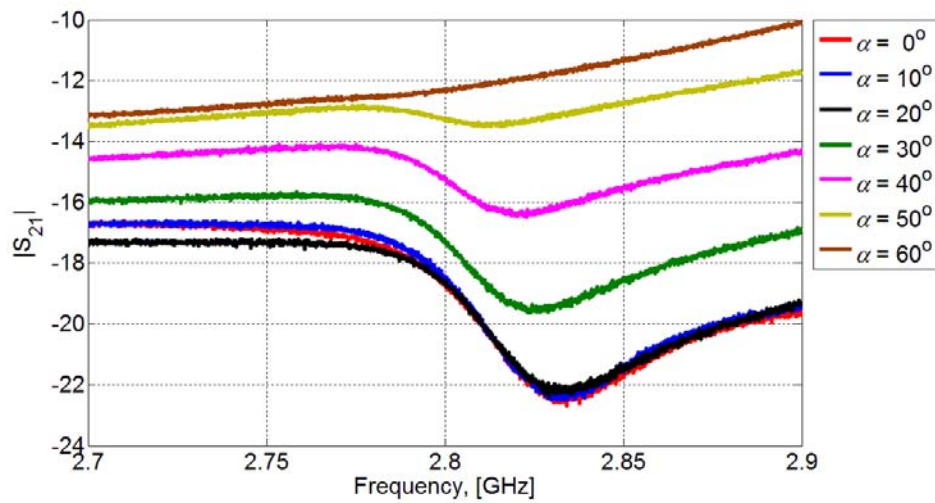


Figure 5.21. Experimental result for transition level related with changing in rotation angle ( $\alpha$ )

Table 5.5. Comparison between simulation and experimental results.

Angle	Resonance frequency $f_0$ (GHz)			Absorption peak level		
	Simulation	Experimental	$ \nabla f_0 $	Simulation	Experimental	$ \nabla A $
$0^\circ$	2.811	2.823	0.012	0.879	0.957	0.078
$10^\circ$	2.808	2.821	0.013	0.841	0.913	0.072
$20^\circ$	2.806	2.820	0.014	0.760	0.860	0.100
$30^\circ$	2.803	2.819	0.016	0.608	0.705	0.097
$40^\circ$	2.800	2.814	0.014	0.375	0.496	0.121
$50^\circ$	2.794	2.810	0.016	0.139	0.195	0.056
$60^\circ$	2.781	2.793	0.012	0.022	0.060	0.038

### 5.3. Influence of Geometrical Parameters

This part presents the results of the studies on the effects of changing geometric parameters and substrate material properties on the absorption level and the resonance frequency, in detail. Therefore, geometric parameters;  $h$ ,  $w$ ,  $L_r$  and material properties; dielectric constant ( $\epsilon_r$ ), and loss tangent ( $\tan \delta$ ) are examined. In order to observe the effects of each parameter properly, the studies are conducted by varying only one parameter at the same time and other parameters are kept constant. The effects are observed for all rotation angles.

#### 5.3.1. Influence of substrate thickness ( $h$ )

Herein three different substrate thicknesses ( $h$ ) are examined parametrically which are 0.5 mm, 1.5 mm, and 2.5 mm, where 1.5 mm is the designed value of this work. The results are reported in Figure 5. 22. The figure shows that AD-CRR is least sensitive to the rotation angle when  $h = 0.5$  mm. As the substrate thicknesses is decreased to 0.5 mm, the substrate losses also decreases and this yields absorption levels drop. But the sensing mechanism still works fine. On the other hand, for  $h = 0.5$  mm, it displayed nearly a linear relation between rotation angle and the absorption level. So logically, when substrate thickness is increased ( $h = 2.5$  mm), it will cause an increase in absorption level as dielectric losses increases. This is also affected in sensing mechanism, as we see for  $\alpha = 0^\circ$ ,  $10^\circ$ , and  $20^\circ$  the absorption is near to unity (see Table 5. 6). The

results displayed rapidly decrease from 90% absorption to 0.077% from 30° to 60° respectively.

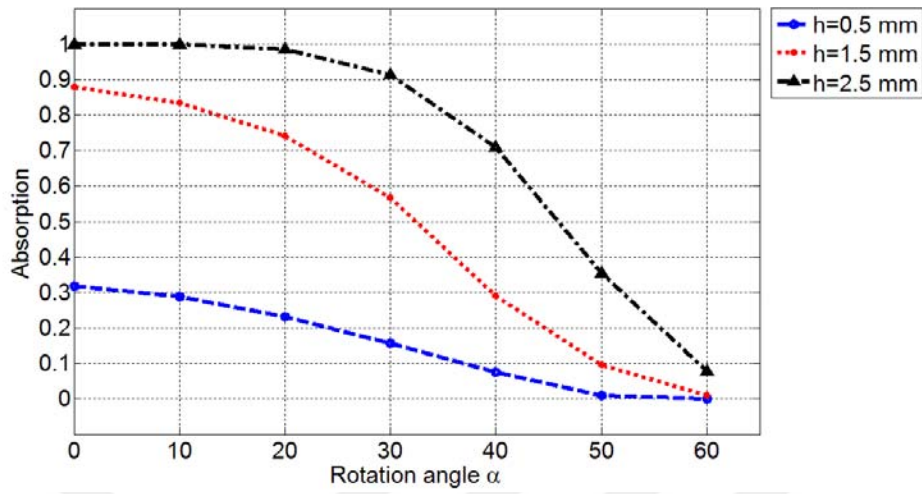


Figure 5.22. Influence of changing substrate thicknesses.

Table 5.6. Relation between rotation angle, absorption level, and resonance frequencies  $f_0$ (GHz) for three steps of changing in substrate thicknesses.

Angle	$h = 0.5 \text{ mm}$		$h = 1.5 \text{ mm}$		$h = 2.5 \text{ mm}$	
	$f_0$ (GHz)	Absorption peak level	$f_0$ (GHz)	Absorption peak level	$f_0$ (GHz)	Absorption peak level
0°	2.670	0.317	2.811	0.879	2.849	0.998
10°	2.670	0.287	2.808	0.841	2.845	0.998
20°	2.668	0.232	2.806	0.760	2.842	0.985
30°	2.668	0.156	2.803	0.608	2.842	0.912
40°	2.668	0.076	2.800	0.375	2.837	0.709
50°	2.479	0.009	2.794	0.139	2.823	0.354
60°	2.479	0.001	2.781	0.022	2.812	0.077

### 5.3.2. Influence of ring width (w)

In order to investigate the effects of ring width (w), five different ring widths are examined which are 3.5 mm, 4 mm, 4.5 mm, 5 mm and 5.5 mm. The results are reported in Figure 5.23, and Table 5. 7. In general, it is not effective, which means that the ring width is highly effective in resonance frequency, have little effect on absorption level. Therefore, when width is increased it cause an

increase in the resonance frequency about 343.8 MHz at 0°. If ring width is increased from 3.5 mm to 5.5 mm (see Table 5.7) the absorption level is increased just 17.85% at the same angle (see Figure 5. 23).

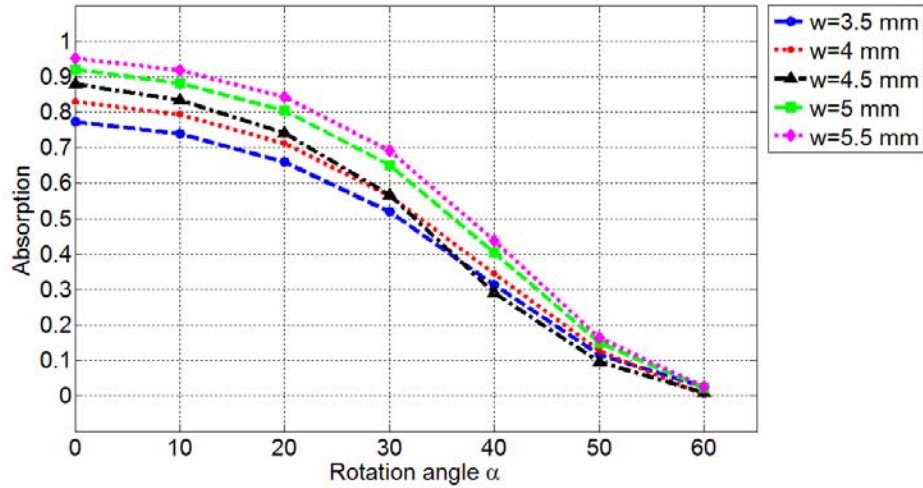


Figure 5. 23. Effect of ring width in absorption level

Table 5. 7. Relation between rotation angle, absorption level, and resonance frequencies  $f_0$ (GHz) for different ring width.

Angle	$w = 3.5$ mm	$w = 4$ mm	$w = 4.5$ mm	$w = 5$ mm	$w = 5.5$ mm
	$f_0$ (GHz)	$f_0$ (GHz)	$f_0$ (GHz)	$f_0$ (GHz)	$f_0$ (GHz)
0°	2.641	2.724	2.811	2.898	2.985
10°	2.635	2.718	2.808	2.895	2.981
20°	2.634	2.716	2.806	2.893	2.977
30°	2.632	2.711	2.803	2.887	2.976
40°	2.630	2.709	2.800	2.884	2.972
50°	2.626	2.704	2.794	2.874	2.965
60°	2.493	2.670	2.781	2.860	2.948

### 5.3.3. Influence of ring size ( $L_r$ )

The last geometrical parameter that will be examined here is the ring side length  $L_r$ . It should be noted that changing  $L_r$  means a changing the side length for both edges since the AD-CRR is a square resonator. The absorption results show an opposite relation between  $L_r$  and absorption level. When  $L_r$  increases, it cause a decrease in the absorption level. For example the absorption decreased

from 0.923 to 0.813 when  $L_r$  increased from 18.5 mm to 21.5 mm at  $0^\circ$  (see Figure 5.24, and Table 5.8).

Additionally, the resonance frequency is highly dependent on length of the ring side. Therefore increasing the ring dimension caused decrease in resonance frequency, and vice versa. The results show about 566 MHz decrease in frequency when the side length increases from 18.5 mm to 21.5 mm (see Table 5.8). It is important to note that the sensing mechanism is not affected by change in ring-side length see Figure 5.22.

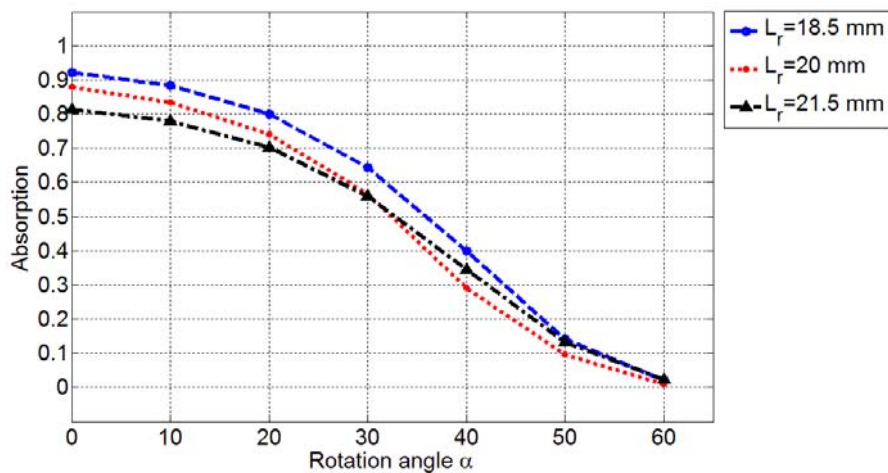


Figure 5.24. The effect of changing ring size on absorption level

Table 5.8. Relation between rotation angle, absorption level, and resonance frequencies  $f_0$ (GHz) for three steps of changing ring size.

Angle	$L_r = 18.5$ mm		$L_r = 20$ mm		$L_r = 21.5$ mm	
	$f_0$ (GHz)	Absorption peak level	$f_0$ (GHz)	Absorption peak level	$f_0$ (GHz)	Absorption peak level
$0^\circ$	3.118	0.923	2.811	0.879	2.553	0.813
$10^\circ$	3.114	0.883	2.808	0.841	2.550	0.779
$20^\circ$	3.111	0.801	2.806	0.760	2.548	0.703
$30^\circ$	3.107	0.644	2.803	0.608	2.546	0.553
$40^\circ$	3.095	0.399	2.800	0.375	2.537	0.344
$50^\circ$	3.088	0.146	2.794	0.139	2.531	0.133
$60^\circ$	3.060	0.022	2.781	0.022	2.513	0.022

The three previous subsections explained the effects of geometrical parameters on absorption mechanism. Depending on the observations, it is concluded that the substrate thickness is the only parameter that play important role in sensing mechanism and that the other parameters just cause a shift in the resonance frequency and/or a little bit is affected in the absorption level.

### 5.3.4. Influence of dielectric change ( $\epsilon_r$ )

The reported dielectric constant value in this work is 4.3 (at 10 GHz) for the substrate type FR-4. Therefore, in order to investigate the effect of dielectric constant, two more values are examined which are 3.3 and 5.3.

According to parallel plate capacitance formula (5.10), the capacitance highly depends on the dielectric constant. Then increase in dielectric constant cause an increase in the capacitance as seen in the equation (Capolino, 2009):

$$C = \frac{A\epsilon_r}{d} \quad (5.10)$$

Where  $A$  is the metallic area and  $d$  is the distance between two metals.

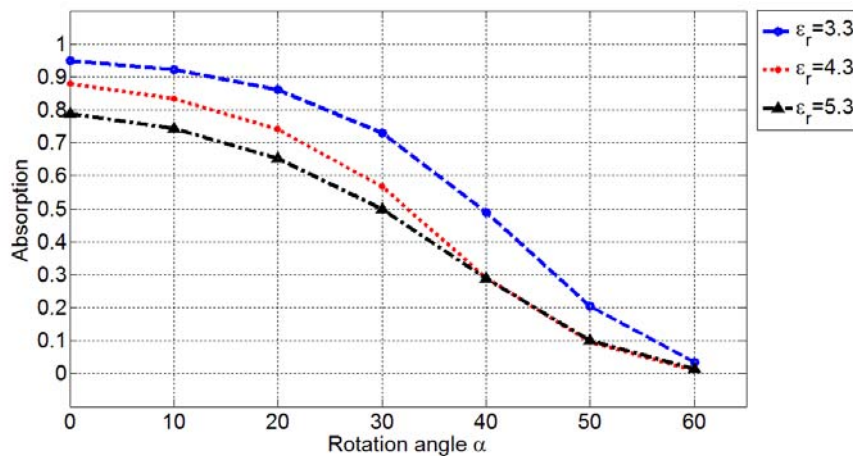


Figure 5. 25. The effects of substrate dielectric constant changes of absorption level.

Then increasing  $C$  causes decrease in resonance frequency according to equation (5. 5). The simulation results confirmed the above explanation. For  $\epsilon_r = 3.3$  the resonance frequency at  $0^\circ$  is 3.171 GHz by increasing  $\epsilon_r$  to 4.3 the

result showed decrease to 2.811 GHz, and a decrease to 2.549 GHz when  $\epsilon_r$  is increased to 5.3 (see Table 5.9). In addition, the change in dielectric constant does not result in a change in the absorption mechanism (see Figure 5.25).

Table 5. 9. Relation between rotation angle, absorption level, and resonance frequencies  $f_0$ (GHz) for three different substrate dielectric constants values.

Angle	$\epsilon_r = 3.3$		$\epsilon_r = 4.3$		$\epsilon_r = 5.3$	
	$f_0$ (GHz)	Absorption peak level	$f_0$ (GHz)	Absorption peak level	$f_0$ (GHz)	Absorption peak level
0°	3.171	0.948	2.811	0.879	2.549	0.789
10°	3.166	0.922	2.808	0.841	2.546	0.743
20°	3.163	0.861	2.806	0.760	2.537	0.652
30°	3.160	0.730	2.803	0.608	2.535	0.498
40°	3.150	0.491	2.800	0.375	2.532	0.288
50°	3.140	0.203	2.794	0.139	2.525	0.101
60°	3.126	0.034	2.781	0.022	2.503	0.015

### 5.3.5. Influence of tangent loss ( $\tan\delta$ )

The last parameter that will be investigated here is tangent loss. This parameter is described the relation between imaginary and real parts of relative dielectric permittivity and follows this formula (Pozar, 2012):

$$\epsilon_r = \epsilon' - j\epsilon'' \quad (5.11)$$

$$\tan\delta = \frac{\epsilon''}{\epsilon'} \quad (5.12)$$

Therefore, to investigate the effects of tangent loss, four different values in addition to the designed value are examined. These are 0.005, 0.015, 0.025, 0.035 and 0.045. In more detail, in Figure 5. 26 tangent loss of 0.005 shows a nonlinear mechanism. When the tangent loss is increased, the sensing mechanism becomes more stable. As a logical consequence, increasing the tangent losses leads to an increase in absorption level (Tuong et al., 2013). This is not surprising result it confirms previous literature (Ekmekci et al., 2015),

and (Tuong et al., 2013). However, in this work increasing tangent loss cause a decrease in absorption level as presented in (Tao et al., 2010 and also a nonlinear decrease in absorption. Similarly, Costa et al. explained the nonlinear results by using impedance matching method. They suggested that increasing the loss tangent higher than designed value cause a reduction in the real part of impedance. So the design does not perfectly match with free space. In the other hand, decreasing loss caused the absorber impedance to be higher than matching impedance and also the absorption level goes down (Costa et al., 2012).

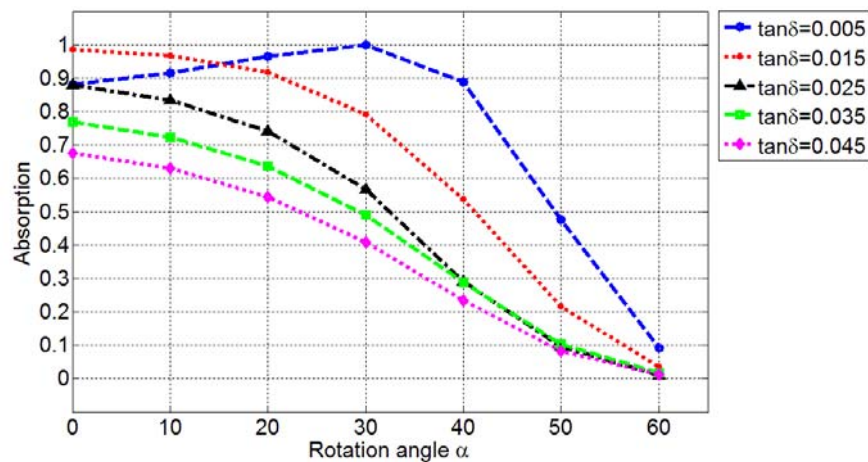


Figure 5. 26. The effect of tangent loss  $\tan\delta$  changes in absorption level.

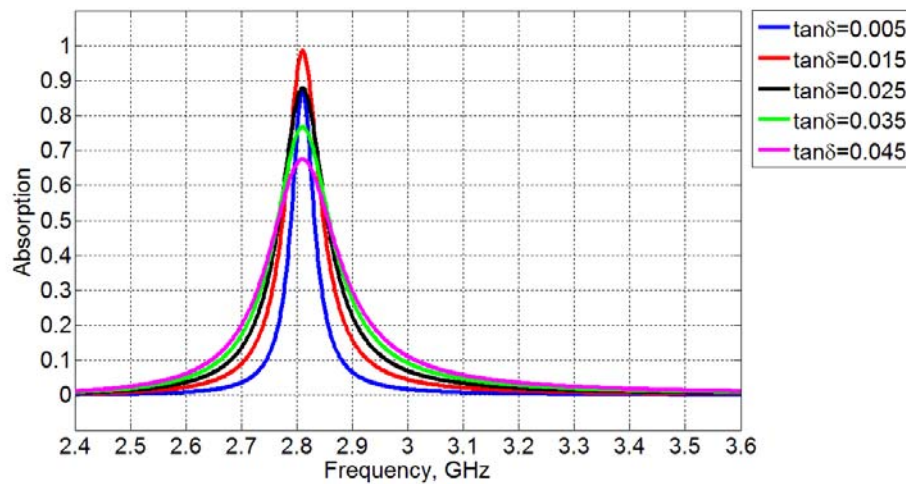


Figure 4. 27. The effect of changing tangent loss  $\tan\delta$  in absorption bandwidth for rotation angle =  $0^\circ$ .

Furthermore, as presented in chapter 2, the absorption means the dissipation of the incident power on the structure. Therefore, an increase in loss tangent is

expected to yield an increase in the dissipated power on the absorber, regardless the absorption level increase or decrease. Therefore, a new graph carried out for this reason for the absorption at  $0^\circ$  for the five-loss tangent values see Figure 5. 27.

Furthermore, figure 5.27 shows perfect absorption when  $\tan\delta = 0.015$ , furthermore increasing in tangent loss beyond 0.015 cause a decrease in the absorption level for  $\alpha = 0^\circ$ .

#### 5.4. Scaling Structure to THz Region

One important point in absorber design is scaling structure for operating in the frequency bands. Generally, scaling from one band to another band inside microwave region which gives highly compatible results. Such scaling is easy and popular in literature, but scaling to THz and optical region is very popular in practice due to their applications like biomedical engineering (Balamati et al., 2016) and information security (Rhee et al., 2014). Additionally microwave cannot propagate in water. On the other hand, THz is non-ionizing and has the ability to pass through wide range of materials (Rhee et al., 2014).

To scale any structure from one range of frequency to work in another range of frequency all we need to do is select scaling factor  $S_f$  then scale all structure parameters according to this factor. Therefore to find scaling factor  $S_f$ :

$$S_f = \frac{\text{resonance frequency in designed range}}{\text{resonance frequency in new range}} \quad (5. 13)$$

For example if we want to scale the designed structure to work in 2.811 THz (we choose this frequency for easy calculation), the scaling factor is  $S_f = 1000$ . So by dividing all parameters value by 1000, means the absorber is scaled to work in THz. Table 5. 11 shows the new parameters for THz region, we note that in THz the structure parameters are in  $\mu\text{m}$ .

In Figure 5. 28. we see that the absorption mechanism is still correct but the absorption level decreased and resonance frequency shifted from the expected

resonance frequency, because material properties in THz are different from GHz. Additionally, the structure parameters are scaled but material properties such as substrate permittivity and tangent loss, and metal conductivity do not scale to work in THz.

Table 5. 11. Structure parameters scaled to work in 2.8104 THz

Parameters	Dimension (mm) (S-band)	Dimension ( $\mu\text{m}$ ) (THz)
$L_x$	72.136	72.136
$L_y$	34.036	34.036
$h$	1.5	1.5
$L_r$	20	20
$w$	4.5	4.5
$t_m$	0.035	0.035

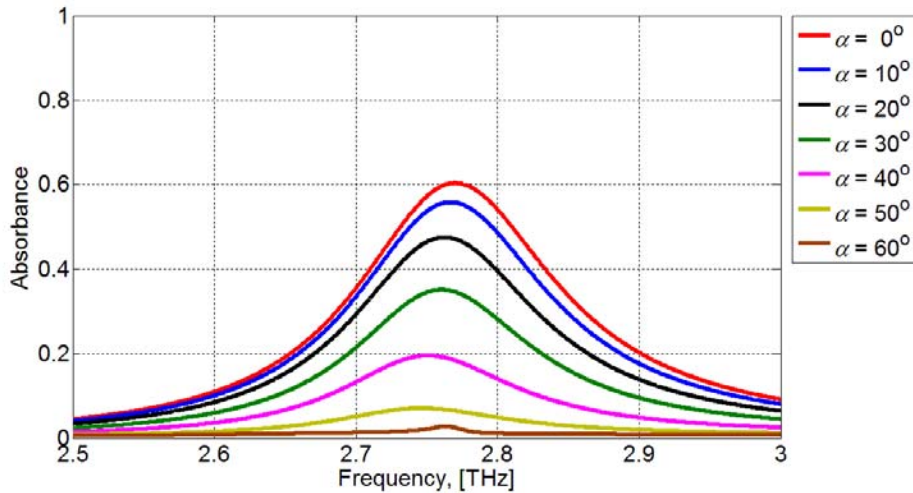


Figure 5. 28. Absorption level related with frequency for all rotation angles for scaling structure.

## 6. CONCLUSION

In the thesis study, a simple structure called Angle Depended Closed Ring Resonator (AD-CRR) consists of closed ring resonator on the top, an FR-4 substrate layer in the middle and a ground plane in the bottom is proposed, numerically analyzed, fabricated and experimentally validated. This structure is presented to be an absorption level tunable structure by folding it mechanically. By folding the two parts of resonator inward, the structure is shown to provide a very good chromatic tuning of the absorption level. The structure is examined in S-band region first numerically and experimentally, then scaled to THz region and additional numerical analyses are performed.

The simulation results approved that the absorption is based on the electrical dipole resonance, however the absorption level can be tuned by tuning the amount of circulating current between the closed ring in the top and metallic ground plane in the bottom.

The comparison between AD-CRR and CAR-CRR structures explain that the AD-CRR structure excited by the two opposite value of E-field  $x$ -components and  $z$ -component. On the other hand, CAR-CRR structure is only excited by one component of  $x$  and one component of  $z$ . This interesting result gives a good explanation for the rapid decreases in absorption level.

The tuning of absorption peak level of the proposed structure based on rotation angle makes it a good candidate for practical applications, such as sensor applications. Additionally, it promises a new future generation of AM-modulator, and ON/OFF switching.

The absorption level peaks and frequency of the resonance can be tailored by controlling the AD-CRR structure parameters and substrate material properties, however the simulation results show:

- The relation between rotation angle and absorption level is not effected by changing the substrate thickness. It only increases the level of absorption as substrate thickness increases.

- Gradual changes in ring width ( $w$ ) effects the resonance frequency, with a very small effect in the absorption level.
- The change in the ring size  $L_r$  can be used to tune the absorption level and the resonance frequency. In more detail, increasing the ring dimension caused decrease in resonance frequency, and vice versa.
- The two parallel plate acts as a capacitance therefore increase in dielectric constant value between the two plates cause an increase in the capacitance and it yields a decrease in the resonance frequency.
- The change in tangent loss presents a nonlinear effect in the absorption level of AD-CRR. The results show that a perfect absorption is possible when the tangent loss is 0.015.

Finally, the simulation results in THz are promised for future potential application such as sensor, perfect absorber, modulator, and switching.

## Appendix A

Consider an electromagnetic plane wave propagate in the z-direction in lossless medium, the electric field is in the x-direction:  $E(z) = \bar{x}E(z)$ , and magnetic field in the y-direction  $H(z) = \bar{y}H(z)$ . See Figure A. 1. (Note that all information here from (Pozar, 2012), (Cheng, 1993), and (Nicolson et al., 1970))

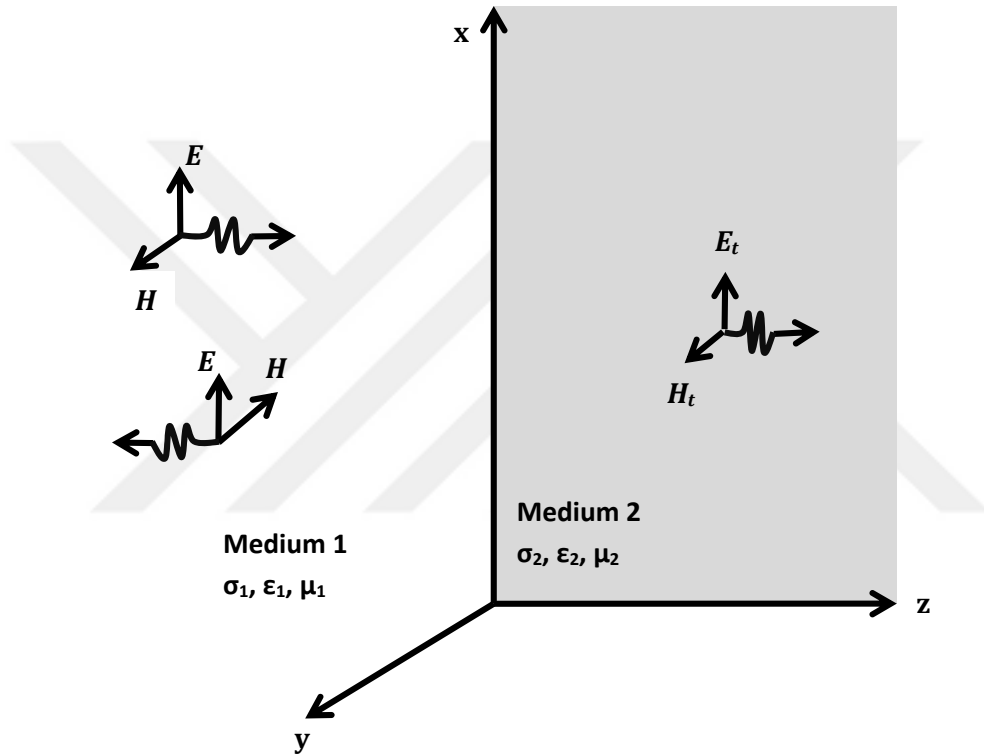


Figure A. 1, Electromagnetic plane wave normal incidence on interface between two different medium, reflection plane wave, and transition plane wave (Cheng., 1993).

Then we can write these relations:

$$E_i(z) = \bar{x}E_o e^{-jk_1 z} \quad (\text{A. 1})$$

$$H_i(z) = \bar{y}H_o e^{-jk_1 z} = \frac{1}{\eta} E_i(z) = \bar{y} \frac{1}{\eta} E_o e^{-jk_1 z} \quad (\text{A. 2})$$

When the plane wave strike into boundary of infinite medium2 then the reflected wave is as following:

$$\mathbf{E}_r(\mathbf{z}) = \bar{\mathbf{x}} \Gamma \mathbf{E}_o e^{jk_1 z} \quad (\text{A. 3})$$

$$\mathbf{H}_r(\mathbf{z}) = \bar{\mathbf{y}} \Gamma \mathbf{H}_o e^{jk_1 z} = \frac{1}{\eta_1} \Gamma \mathbf{E}_r(\mathbf{z}) = -\bar{\mathbf{y}} \frac{1}{\eta_1} \Gamma \mathbf{E}_o e^{jk_1 z} \quad (\text{A. 4})$$

Where  $\Gamma$  is reflection coefficient, and  $\eta_1$  is intrinsic impedance in medium one, then from the above functions, we can drive reflection matrix:

$$\begin{bmatrix} \mathbf{E}_r(\mathbf{z}) \\ \mathbf{H}_r(\mathbf{z}) \end{bmatrix} = \begin{bmatrix} \bar{\mathbf{x}} \Gamma e^{jk_1 z} & \mathbf{0} \\ \mathbf{0} & -\bar{\mathbf{y}} \Gamma e^{jk_1 z} / \eta_1 \end{bmatrix} \begin{bmatrix} \mathbf{E}_o(\mathbf{z}) \\ \mathbf{E}_o(\mathbf{z}) \end{bmatrix} \quad (\text{Reflection matrix}) \quad (\text{A. 5})$$

Therefore, we start from the above functions to drive transition matrix:

$$\mathbf{E}_t = \bar{\mathbf{x}} \mathbf{T} \mathbf{E}_o e^{-j\gamma z} \quad (\text{A. 6})$$

$$\mathbf{H}_t = \bar{\mathbf{y}} \frac{1}{\eta_2} \mathbf{T} \mathbf{E}_o e^{-j\gamma z} \quad (\text{A. 7})$$

$$\eta_2 = \frac{j2\pi f \mu}{\gamma} \quad (\text{A. 8})$$

$$\gamma = \alpha + j\beta = j2\pi f \sqrt{\mu \epsilon} \sqrt{1 - j\sigma / 2\pi f \epsilon} \quad (\text{A. 9})$$

Where  $\mathbf{T}$  is transmission coefficient,  $\eta_2$  is intrinsic impedance in medium two,  $\gamma$  is complex propagation factor,  $\beta$  is phase factor, and  $\alpha$  is attenuation factor. Equation (A. 9) for FR4 substrate can be reduce to this form ( $\gamma = j2\pi f \sqrt{\mu \epsilon}$ ) because at GHz frequency  $j\sigma / 2\pi f \epsilon \approx 0$ , so the intrinsic impedance become :

$$\eta_2 = \sqrt{\frac{\mu_2}{\epsilon_2}} \quad (\text{A. 10})$$

Additionally, the transition wave related with incident and reflection wave by (A. 11), and (A. 12).

$$\mathbf{E}_t = \mathbf{E}_i(z) + \mathbf{E}_r(z) = \bar{x}\mathbf{E}_o e^{-jk_1 z} + \bar{x}\mathbf{E}_o e^{jk_1 z} \quad (\text{A. 11})$$

$$\mathbf{H}_t = \frac{1}{\eta_2} \mathbf{E}_i(z) - \frac{1}{\eta_2} \mathbf{E}_r(z) = \bar{y} \frac{1}{\eta_2} \mathbf{E}_o e^{-jk_1 z} - \bar{y} \frac{1}{\eta_2} \mathbf{E}_o e^{jk_1 z} \quad (\text{A. 12})$$

$$\begin{bmatrix} \mathbf{E}_t(z) \\ \mathbf{H}_t(z) \end{bmatrix} = \begin{bmatrix} \mathbf{1} & \mathbf{1} \\ \mathbf{1}/\eta_2 & -\mathbf{1}/\eta_2 \end{bmatrix} \begin{bmatrix} \mathbf{E}_i(z) \\ \mathbf{E}_r(z) \end{bmatrix} \quad (\text{Transition matrix}) \quad (\text{A. 13})$$

Therefore, the reflection coefficient and transition coefficient follow respectively:

$$\Gamma = \frac{E_r}{E_i} \quad (\text{A. 14})$$

By Dividing the two side of equations (A. 11), and (A. 12) into  $E_i$  :

$$\mathbf{1} + \Gamma = \mathbf{T} \quad (\text{A. 15})$$

$$\frac{\mathbf{T}}{\eta_2} = \frac{1}{\eta_1} - \frac{\Gamma}{\eta_1} \quad (\text{A. 16})$$

$$\Gamma = \frac{\eta_2 - \eta_1}{\eta_2 + \eta_1} \quad (\text{Reflection coefficient}) \quad (\text{A. 17})$$

$$\mathbf{T} = \frac{2\eta_2}{\eta_2 + \eta_1} \quad (\text{Transmission coefficient}) \quad (\text{A. 18})$$

## Appendix B

Consider an electromagnetic plane wave propagate in lossless medium and oblique incident into interface between medium one and medium two, and medium two bounded by PEC conductor (see Figure B. 1). Where,  $\theta_i$  represent oblique incident angle,  $\Gamma_{11}\exp(i\phi_{11})$  is reflection coefficient and reflection angle from first interface between medium one and two,  $T_{12}\exp(i\theta_{12})$  is transmission coefficient and transmission angle for incident wave throw first interface, the partial transmission wave goes through medium 2 with propagation complex phase vector  $\beta$ . Additionally, transmission wave continue to propagate through

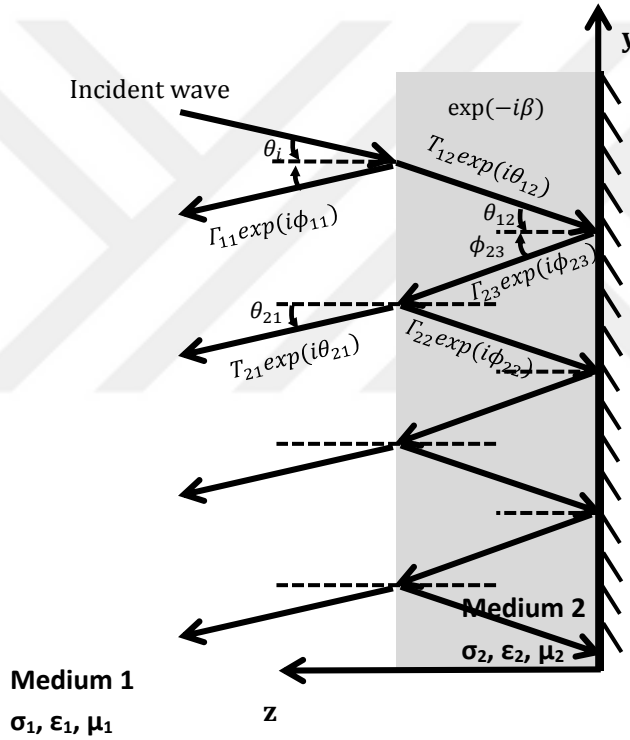


Figure B. 1, Electromagnetic plane wave oblique incidence on interface between two different medium by incident angle  $\theta_i$ .

medium 2 until it arrives to metallic PEC ground, then signal reflects back with reflection coefficient and reflection angle from PEC interface  $\Gamma_{23}\exp(i\phi_{23})$ . Then when it reaches interface medium 2 to medium 1, the signal is also separated into two parts. One reflects back inside medium two  $\Gamma_{22}\exp(i\phi_{22})$ . And the second partial part passes through the interface with transmission coefficient, and angle  $T_{21}\exp(i\theta_{21})$ . This mechanism is continues until reflection inside

medium 2 vanishes. Then the total reflection is calculated by superposition, next modulating absorber by equations:

$$\begin{aligned}
\Gamma_{\text{total}} &= \Gamma_{11}e^{i\phi_{11}} + T_{12}e^{i\theta_{12}}e^{-i\beta}e^{i\phi_{23}}e^{-i\beta}T_{21}e^{i\theta_{21}} \\
&\quad + T_{12}e^{i\theta_{12}}e^{-i\beta}e^{i\phi_{23}}e^{-i\beta}(\Gamma_{22}e^{i\phi_{22}}e^{-i\beta}e^{i\phi_{23}}e^{-i\beta})^1T_{21}e^{i\theta_{21}} \\
&\quad + T_{12}e^{i\theta_{12}}e^{-i\beta}e^{i\phi_{23}}e^{-i\beta}(\Gamma_{22}e^{i\phi_{22}}e^{-i\beta}e^{i\phi_{23}}e^{-i\beta})^2T_{21}e^{i\theta_{21}} + \dots \\
&\quad \dots + T_{12}e^{i\theta_{12}}e^{-i\beta}e^{i\phi_{23}}e^{-i\beta}(\Gamma_{22}e^{i\phi_{22}}e^{-i\beta}e^{i\phi_{23}}e^{-i\beta})^nT_{21}e^{i\theta_{21}} \\
\Gamma_{\text{total}} &= \Gamma_{11}e^{i\phi_{11}} + T_{12}T_{21}e^{i(\theta_{12}-2\beta+\phi_{23}+\theta_{21})} \sum_{n=0}^{\infty} (\Gamma_{22}e^{i(\phi_{22}-2\beta+\phi_{23})})^n
\end{aligned}$$

We must note that PEC conductor reflects wave by  $e^{i\phi_{23}} = -1 = e^{-i\pi}$  then:

$$\begin{aligned}
\Gamma_{\text{total}} &= \Gamma_{11}e^{i\phi_{11}} + T_{12}T_{21}e^{i(\theta_{12}+\theta_{21}-2\beta-\pi)} \sum_{n=0}^{\infty} (\Gamma_{22}e^{i(\phi_{22}-2\beta-\pi)})^n \\
\Gamma_{\text{total}} &= \Gamma_{11}e^{i\phi_{11}} + \frac{T_{12}T_{21}e^{i(\theta_{12}+\theta_{21}-2\beta-\pi)}}{1 - \Gamma_{22}e^{i(\phi_{22}-2\beta-\pi)}}
\end{aligned}$$

Where  $\beta = \frac{2\pi}{\lambda_0}nd$  complex propagation phase in medium 2,  $n$  substrate refractive index,  $\lambda_0$  is wavelength free space, and  $d$  is the distance wave need to move from interface one to PEC interface:

$$n = \sqrt{\varepsilon_2\mu_2}$$

From Snell's law we can calculate the propagation distance:

$$n_1 \sin(\theta_i) = n_2 \sin(\theta_{12})$$

$$\sin(\theta_{12}) = \frac{n_2}{n_1 \sin(\theta_i)}$$

$$\theta_{12} = \sin^{-1} \left( \sqrt{\frac{\epsilon_1 \mu_1}{\epsilon_2 \mu_2}} \sin(\theta_i) \right)$$

$$d = h \cos \left( \sin^{-1} \left( \frac{\sin(\theta_i)}{\sqrt{\frac{\epsilon_2 \mu_2}{\epsilon_1 \mu_1}}} \right) \right)$$

$h$  is substrate thickness.



## REFERENCES

- Abdin, M., Rafique, U., Malik, F., Qasim, S., Khan, M. A., & Ahmed, M. M., 2012. A novel dual-band frequency selective surface absorber. *International Journal of Electromagnetics and Applications*, 2(6), 182-185.
- Alaee, R., Menzel, C., Rockstuhl, C., Lederer, F., 2012. Perfect absorbers on curved surfaces and their potential applications. *Optics express*, 20(16), 18370-18376.
- Al-Naib, I. A. I., Jansen, C., Koch, M., 2008. Thin-film sensing with planar asymmetric metamaterial resonators. *Applied Physics Letters*, 93(8), 083507-0835073.
- Averitt, R. D., Padilla, W. J., Chen, H. T., O'Hara, J. F., Taylor, A. J., Highstrete, C., Lee, M., Zide, J. M. O., Bank, S. R., Gossard, A. C., 2007. Terahertz metamaterial devices. In *Optics East, International Society for Optics and Photonics*.677209-677209.
- Aydin, K., Bulu, I., Guven, K., Kafesaki, M., Soukoulis, C. M., & Ozbay, E., 2005. Investigation of magnetic resonances for different split-ring resonator parameters and designs. *New journal of physics*, 7(1), 168.
- Aydin, K., Ferry, V. E., Briggs, R. M., Atwater, H. A., 2011. Broadband polarization-independent resonant light absorption using ultrathin plasmonic super absorbers. *Nature communications*, 2, 517.
- Ayop, O. B., Abd Rahim, M. K., Murad, N. A., Samsuri, N. A., & Dewan, R., 2014. Triple Band Circular Ring-Shaped Metamaterial Absorber for X-Band Applications. *Progress In Electromagnetics Research M*, 39, 65-75.
- Ayop, O., Rahim, M. K. A., Murad, N. A., & Samsuri, N. A., 2016. Dual-resonant polarization-independent and wide-angle metamaterial absorber in X-band frequency. *Applied Physics A*, 122(4), 1-7.
- Balanis, C. A., 1989. *Advanced engineering electromagnetics*. Second edition. John Wiley & Sons.
- Balanis, C. A., 2005. *Antenna theory: analysis and design*. Third edition. John Wiley & Sons.
- Baskey, H. B., Akhtar, M. J., Dixit, A. K., Shami, T. C., 2015. Design, synthesis, characterization and performance evaluation of multi-band perfect

- metamaterial absorber. *Journal of Electromagnetic Waves and Applications*, 29(18), 2479-2491.
- Bilotti, F., Toscano, A., Vegni, L., Aydin, K., Alici, K. B., Ozbay, E., 2007. Equivalent-circuit models for the design of metamaterials based on artificial magnetic inclusions. *Microwave Theory and Techniques, IEEE Transactions on*, 55(12), 2865-2873.
- Bingham, C. M., Tao, H., Liu, X., Averitt, R. D., Zhang, X., and Padilla, W. J., 2008. Planar wallpaper group metamaterials for novel terahertz applications. *Optics Express*, 16(23), 18565-18575.
- Capolino, F., 2009. *Applications of metamaterials*. Taylor and Francis Group, LLC.
- Celozzi, S., Lovat, G., Araneo, R., 2008. *Electromagnetic shielding*. John Wiley & Sons, Inc.
- Che Seman, F., Cahill, R., Fusco, V. F., Goussetis, G., 2011. Design of a salisbury screen absorber using frequency selective surfaces to improve bandwidth and angular stability performance. *Microwaves, Antennas & Propagation, IET*, 5(2), 149-156.
- Chen, H. T., 2012. Interference theory of metamaterial perfect absorbers. *Optics express*, 20(7), 7165-7172.
- Cheng, D. K. 1993. *Fundamentals of engineering electromagnetics*. Addison-Wesley Publishing Company, Inc.
- Cheng, Y., Nie, Y., Gong, R., 2013. A polarization-insensitive and omnidirectional broadband terahertz metamaterial absorber based on coplanar multi-squares films. *Optics & Laser Technology*, 48, 415-421.
- Choudhury, B., Menon, A., & Jha, R. M., 2016. *Active Terahertz Metamaterial for Biomedical Applications*. Springer Singapore. 1-41.
- Costa, F., Genovesi, S., Monorchio, A., Manara, G., 2013. A circuit-based model for the interpretation of perfect metamaterial absorbers. *Antennas and Propagation, IEEE Transactions on*, 61(3), 1201-1209.
- Daintith, J. 2009. *The facts on file dictionary of physics*. Infobase Publishing. Edition Fourth. - Aylesbury, UK : Market House Books Ltd.

- Dincer, F., 2015. Electromagnetic energy harvesting application based on tunable perfect metamaterial absorber. *Journal of Electromagnetic Waves and Applications*, 1-10.
- Dincer, F., Akgol, O., Karaaslan, M., Unal, E., Sabah, C., 2014. Polarization angle independent perfect metamaterial absorbers for solar cell applications in the microwave, infrared, and visible regime. *Progress In Electromagnetics Research*, 144, 93-101.
- Do, T. V., Bui, S. T., Nguyen, T. H., Nguyen, T. T., Nguyen, T. T., Lee, Y., Vu, D. L. 2012. Design, fabrication and characterization of a perfect absorber using simple cut-wire metamaterials. *Advances in Natural Sciences: Nanoscience and Nanotechnology*, 3(4), 045014.
- Du Toit, L. J., Cloete, J. H., 1990, May. Advances in the design of Jaumann absorbers. In *Antennas and Propagation Society International Symposium, 1990. AP-S. Merging Technologies for the 90's. Digest IEEE..* 1212-1215.
- Dunsmore, J. P., 2012. *Handbook of microwave component measurements: with advanced VNA techniques.* John Wiley & Sons.
- Dybdal, R. B., 1987. Radar cross section measurements. *Proceedings of the IEEE*, 75(4), 498-516.
- Ekmekci, E., Demir, E., 2015, On/Off Switching of Absorption Spectra by Layer Shifting for Double Layer Metamaterial Based Absorber. *Antennas and Wireless Propagation Letters: IEEE.* (15), 532 – 535.
- Ekmekci, E., Strikwerda, A. C., Fan, K., Keiser, G., Zhang, X., Turhan-Sayan, G., Averitt, R. D., 2011. Frequency tunable terahertz metamaterials using broadside coupled split-ring resonators. *Physical Review B*, 83(19), 193103-1931034.
- Ekmekci, E., Turhan-Sayan, G., 2009. Comparative investigation of resonance characteristics and electrical size of the double-sided SRR, BC-SRR and conventional SRR type metamaterials for varying substrate parameters. *Progress In Electromagnetics Research B*, 12, 35-62.
- Ekmekci, E., Turhan-Sayan, G., 2011, July. Metamaterial sensor applications based on broadside-coupled SRR and V-Shaped resonator structures. In *2011 IEEE International Symposium on Antennas and Propagation (APSURSI).* 1170 – 1172.

- Ekmekci, E., Turhan-Sayan, G., 2013. Multi-functional metamaterial sensor based on a broad-side coupled SRR topology with a multi-layer substrate. *Applied Physics A*, 110(1), 189-197.
- Emerson, W. H., 1973. Electromagnetic wave absorbers and anechoic chambers through the years. *Antennas and Propagation, IEEE Transactions on*, 21(4), 484-490.
- Engen, G. F., Hoer, C. A., 1979. Thru-reflect-line: An improved technique for calibrating the dual six-port automatic network analyzer. *Microwave Theory and Techniques, IEEE Transactions on*, 27(12), 987-993.
- Fedotov, V. A., Rose, M., Prosvirnin, S. L., Papasimakis, N., Zheludev, N. I., 2007. Sharp trapped-mode resonances in planar metamaterials with a broken structural symmetry. *Physical Review Letters*, 99(14), 147401.
- Feng, Y. B., Qiu, T., Shen, C. Y., 2007. Absorbing properties and structural design of microwave absorbers based on carbonyl iron and barium ferrite. *Journal of Magnetism and Magnetic Materials, Science Direct*, 318(1), 8-13.
- Fu, Y. H., Liu, A. Q., Zhu, W. M., Zhang, X. M., Tsai, D. P., Zhang, J. B., Mei, Ting., Tao, Ji F., Chen, H., Zhang, Xin H., Teng, Jing H., Zheludev, Nikolay I., Lo, Guo Q. T., J. H., A., 2011. Micromachined Reconfigurable Metamaterial via Reconfiguration of Asymmetric Split-Ring Resonators. *Advanced Functional Materials*, 21(18), 3589-3594.
- Ghosh, S., Srivastava, K. V., 2015. An equivalent circuit model of FSS-based metamaterial absorber using coupled line theory. *Antennas and Wireless Propagation Letters, IEEE*, 14, 511-514.
- Han, Z., Kohno, K., Fujita, H., Hirakawa, K., Toshiyoshi, H., 2014. MEMS reconfigurable metamaterial for terahertz switchable filter and modulator. *Optics express*, 22(18), 21326-21339.
- Hawkes, A. M., Katko, A. R., Cummer, S. A., 2013. A microwave metamaterial with integrated power harvesting functionality. *Applied Physics Letters, American Institute of Physics (AIP)*, 103(16), 163901-1639013.
- He, X. J., Li, T. Y., Wang, L., Wang, J. M., Jiang, J. X., Yang, G. H., Meng, Fan-yi., Wu, Q., 2014. Electrically tunable terahertz wave modulator based on

- complementary metamaterial and graphene. *Journal of Applied Physics*, 115(17), 17B903-17B9033.
- He, X. J., Wang, Y., Wang, J., Gui, T., Wu, Q., 2011. Dual-band terahertz metamaterial absorber with polarization insensitivity and wide incident angle. *Progress In Electromagnetics Research*, 115, 381-397.
- Hu, F., Qian, Y., Li, Z., Niu, J., Nie, K., Xiong, X., Zhang, W., Peng, Z., 2013. Design of a tunable terahertz narrowband metamaterial absorber based on an electrostatically actuated MEMS cantilever and split ring resonator array. *Journal of Optics*, 15(5), 055101-055107.
- Huang, L., and Chen, H., 2011. Multi-band and polarization insensitive metamaterial absorber. *Progress In Electromagnetics Research*, 113, 103-110.
- Huang, T. Y., Tseng, C. W., Yeh, T. T., Yeh, T. T., Luo, C. W., Akalin, T., Yen, T. J., 2015. Experimental realization of ultrathin, double-sided metamaterial perfect absorber at terahertz gap through stochastic design process. *Scientific reports*, (5), 186051-186056.
- Huang, X., He, X., Guo, L., Yi, Y., Xiao, B., Yang, H., 2015. Analysis of ultra-broadband metamaterial absorber based on simplified multi-reflection interference theory. *Journal of Optics*, 17(5), 055101-055109.
- Huang, X., Yang, D., Yang, H., 2014. Multiple-band reflective polarization converter using U-shaped metamaterial. *Journal of Applied Physics: American Institute of Physics*, 115(10), 103505-1035056.
- Huang, X., Yang, H., Yu, S., Wang, J., Li, M., Ye, Q. 2013. Triple-band polarization-insensitive wide-angle ultra-thin planar spiral metamaterial absorber. *Journal of Applied Physics: American Institute of Physics*, 113(21), 213516-2135166.
- Landy, N. I., Bingham, C. M., Tyler, T., Jokerst, N., Smith, D. R., Padilla, W. J., 2009. Design, theory, and measurement of a polarization-insensitive absorber for terahertz imaging. *physical review B: American Physical Society*, 79(12), 125104-1251046.
- Landy, N. I., Sajuyigbe, S., Mock, J. J., Smith, D. R., Padilla, W. J., 2008. Perfect metamaterial absorber. *Physical review letters*, 100(20), 207402-2074024.

- Lapine, M., Powell, D., Gorkunov, M., Shadrivov, I., Marqués, R., Kivshar, Y., 2009. Structural tunability in metamaterials. *Applied Physics Letters: The American Institute of Physics*, 95(8), 0841050-0841053.
- Lee, Y. P., Rhee, J. Y., Yoo, Y. J., & Kim, K. W., 2016. *Metamaterials for Perfect Absorption*. Springer.
- Li, J., Shah, C. M., Withayachumnankul, W., Ung, B. S. Y., Mitchell, A., Sriram, S., Bhaskaran, M., Chang, S., Abbott, D., 2013. Mechanically tunable terahertz metamaterials. *Applied Physics Letters: The American Institute of Physics*, 102(12), 121101-1211014.
- Liu, X., Padilla, W. J., 2015. Thermochromic Infrared Metamaterials. *Advanced Materials. Wiley Online Library*. 5 (28), 871–875.
- Luo, H., Cheng, Y. Z., Gong, R. Z., 2011. Numerical study of metamaterial absorber and extending absorbance bandwidth based on multi-square patches. *The European Physical Journal B: Springer-Verlag*, 81(4), 387-392.
- Manceau, J. M., Shen, N. H., Kafesaki, M., Soukoulis, C. M., Tzortzakis, S., 2010. Dynamic response of metamaterials in the terahertz regime: Blueshift tunability and broadband phase modulation. *Applied Physics Letters: The American Institute of Physics*, 96(2), 021111-021113.
- Mandal, A., Ghosh, D., Malas, A., Pal, P., Das, C. K., 2012. Synthesis and Microwave Absorbing Properties of Cu-Doped Nickel Zinc Ferrite/Pb (Zr<sub>0.52</sub>Ti<sub>0.48</sub>)O<sub>3</sub> Nanocomposites. *Journal of Engineering: Hindawi Publishing Corporation*, 2013, 3910831-3910838.
- Marqués, R., Medina, F., Rafii-El-Idrissi, R., 2002. Role of bianisotropy in negative permeability and left-handed metamaterials. *Physical Review B: The American Institute of Physics*, 65(14), 144441-144446.
- Melik, R., Unal, E., Perkgoz, N. K., Puttlitz, C., Demir, H. V., 2009. Flexible metamaterials for wireless strain sensing. *Applied Physics Letters: The American Institute of Physics*, 95(18), 181105-181108.
- Melik, R., Unal, E., Perkgoz, N. K., Puttlitz, C., Demir, H. V., 2010. Metamaterial based telemetric strain sensing in different materials. *Optics express: Optical Society of America*, 18(5), 5000-5007.

- Mirza, I., Sabas, J. N., Shi, S., Prather, D. W., 2009. Experimental demonstration of metamaterial-based phase modulation. *Progress In Electromagnetics Research: EMW Publishing*, 93, 1-12.
- Mitra, R., Chan, C. H., Cwik, T., 1988. Techniques for analyzing frequency selective surfaces-a review. *Proceedings of the IEEE*, 76(12), 1593-1615.
- Munk Ben A., 2000. *Frequency Selective Surfaces Theory and Design*. John Wiley and Sons.
- Munk Ben A., 2008. *Metamaterials critique and alternatives*. John Wiley and Sons, Inc.
- Nakanishi, T., Kitano, M., 2015. Implementation of electromagnetically induced transparency in a metamaterial controlled with auxiliary waves. *Physical Review Applied: The American Institute of Physics*, 4(2), 024013-0240139.
- Naqui, J., Martin, F., 2013. Transmission lines loaded with bisymmetric resonators and their application to angular displacement and velocity sensors. *Microwave Theory and Techniques, IEEE Transactions on*, 61(12), 4700-4713.
- Nguyen, T. H., Bui, S. T., Nguyen, T. T., Nguyen, T. T., Lee, Y., Nguyen, M. A., Vu, D. L., 2014. Metamaterial-based perfect absorber: polarization insensitivity and broadband. *Advances in Natural Sciences: Nanoscience and Nanotechnology, IOP publishing*, 5(2), 025013-0250137.
- Nicolson, A. M., Ross, G. F., 1970. Measurement of the intrinsic properties of materials by time-domain techniques. *Instrumentation and Measurement, IEEE Transactions on*, 19(4), 377-382.
- Orfanidis, S. J., 2002. *Electromagnetic waves and antennas*. New Brunswick, NJ: Rutgers University 227-250.
- Otto, H., & Johnson, M. H. (1960). U.S. Patent No. 2,951,246. Washington, DC: U.S. Patent and Trademark Office.
- Ou, J. Y., Plum, E., Zhang, J., Zheludev, N. I., 2013. An electromechanically reconfigurable plasmonic metamaterial operating in the near-infrared. *Nature nanotechnology, Macmillan Publishers Limited.*, 8(4), 252-255.

- Padilla, W. J., Taylor, A. J., Highstrete, C., Lee, M., Averitt, R. D., 2006. Dynamical electric and magnetic metamaterial response at terahertz frequencies. *Physical Review Letters*, 96(10), 107401-1074014.
- Padilla, W. J., Taylor, A. J., Highstrete, C., Lee, M., Averitt, R. D., 2006. Dynamical electric and magnetic metamaterial response at terahertz frequencies. *Physical Review Letters: The American Physical Society*, 96(10), 107401-107404.
- Pang, Y., Cheng, H., Zhou, Y., Wang, J., 2013. Analysis and design of wire-based metamaterial absorbers using equivalent circuit approach. *Journal of Applied Physics, The American Physical Society*, 113(11), 114902.
- Pendry, J. B., Holden, A. J., Robbins, D. J., Stewart, W. J., 1999. Magnetism from conductors and enhanced nonlinear phenomena. *Microwave Theory and Techniques, IEEE Transactions on*, 47(11), 2075-2084.
- Pitchappa, P., Ho, C. P., Dhakar, L., Qian, Y., Singh, N., Lee, C., 2015. Periodic array of subwavelength MEMS cantilevers for dynamic manipulation of terahertz waves. *Microelectromechanical Systems, Journal of*, 24(3), 525-527.
- Pozar David M., *Microwave Engineering*, JohnWiley & Sons, Inc., 2012. - Fourth Edition.
- Sabah, C., Dincer, F., Karaaslan, M., Unal, E., Akgol, O., Demirel, E., 2014. Perfect metamaterial absorber with polarization and incident angle independencies based on ring and cross-wire resonators for shielding and a sensor application. *Optics Communications*, 322, 137-142.
- Sabah, C., Turkmen-Kucuksari, O., Turhan-Sayan, G., 2014. Metamaterial absorber-based sensor embedded into X-band waveguide. *Electronics Letters*, 50(15), 1074-1076.
- Savo, S., Shrekenhamer, D., Padilla, W. J., 2014. Liquid crystal metamaterial absorber spatial light modulator for THz applications. *Advanced Optical Materials*, 2(3), 275-279.
- Shadrivov, I. V., Lapine, M., Kivshar Y. S., 2015. *Nonlinear, tunable and active metamaterials..* New York, NY, USA: Springer.
- Shao, J., Li, J., Li, J., Wang, Y. K., Dong, Z. G., Chen, P., Wu, Rui-Xin, Zhai, Y., 2013. Analogue of electromagnetically induced transparency by doubly

- degenerate modes in a U-shaped metamaterial. *Applied Physics Letters*, 102(3), 034106-034109.
- Shen, X., Cui, T. J., Zhao, J., Ma, H. F., Jiang, W. X., & Li, H., 2011. Polarization-independent wide-angle triple-band metamaterial absorber. *Optics Express*, 19(10), 9401-9407. ISO 690.
- Singh, P. K., Korolev, K. A., Afsar, M. N., Sonkusale, S., 2011. Single and dual band 77/95/110 GHz metamaterial absorbers on flexible polyimide substrate. *Applied Physics Letters*, 99(26), 264101-264104.
- Smith, D. R., Vier, D. C., Koschny, T., Soukoulis, C. M., 2005. Electromagnetic parameter retrieval from inhomogeneous metamaterials. *Physical Review E*, 71(3), 036617-036621.
- Sun, J., Liu, L., Dong, G., Zhou, J., 2011. An extremely broad band metamaterial absorber based on destructive interference. *Optics Express*, 19(22), 21155-21162.
- Tao, H., Bingham, C. M., Pilon, D., Fan, K., Strikwerda, A. C., Shrekenhamer, D., D., Landy, N. I., Padilla, W. J., Zhang, X., Averitt, R. D., 2010. A dual band terahertz metamaterial absorber. *Journal of physics D: Applied physics*, 43(22), 225102-225107.
- Tao, H., Bingham, C. M., Strikwerda, A. C., Pilon, D., Shrekenhamer, D., Landy, N. I., Padilla, W. J., Zhang, X., Averitt, R. D., 2008. Highly flexible wide angle of incidence terahertz metamaterial absorber: Design, fabrication, and characterization. *physical review B*, 78(24), 241103-241107.
- Tuong, P. V., Park, J. W., Lam, V. D., Jang, W. H., Nikitov, S. A., Lee, Y. P., 2013. Dielectric and Ohmic losses in perfectly absorbing metamaterials. *Optics Communications*, 295, 17-20.
- Valente, J., Ou, J. Y., Plum, E., Youngs, I. J., Zheludev, N. I., 2015. Reconfiguring photonic metamaterials with currents and magnetic fields. *Applied Physics Letters*, 106(11), 111905-111909.
- Wang, B. X., Zhai, X., Wang, G. Z., Huang, W. Q., Wang, L. L., 2015. Design of a four-band and polarization-insensitive terahertz metamaterial absorber. *Photonics Journal, IEEE*, 7(1), 1-8.

- Wang, B. X., Zhai, X., Wang, G. Z., Huang, W. Q., Wang, L. L., 2015. A novel dual-band terahertz metamaterial absorber for a sensor application. *Journal of Applied Physics*, 117(1), 014504.
- Wanghuang, T., Chen, W., Huang, Y., Wen, G., 2013. Analysis of metamaterial absorber in normal and oblique incidence by using interference theory. *AIP Advances*, 3(10), 102118-102126.
- Watts, C. M., Liu, X., & Padilla, W. J. (2012). Metamaterial electromagnetic wave absorbers. *Advanced Materials*, 24(23), OP98–OP120.
- Watts, C. M., Shrekenhamer, D., Montoya, J., Lipworth, G., Hunt, J., Sleasman, T., Krishna, S., Smith, David R., Padilla, W. J., 2014. Terahertz compressive imaging with metamaterial spatial light modulators. *Nature Photonics*, 8(8), 605-609.
- Withayachumnankul, W., Jaruwongrungrsee, K., Tuantranont, A., Fumeaux, C., Abbott, D., 2013. Metamaterial-based microfluidic sensor for dielectric characterization. *Sensors and Actuators A: Physical*, 189, 233-237.
- Xu, W., Sonkusale, S., 2013. Microwave diode switchable metamaterial reflector/absorber. *Applied Physics Letters*, 103(3), 031902-031906.
- Yang, G. H., Liu, X. X., Lv, Y. L., Fu, J. H., Wu, Q., Gu, X., 2014. Broadband polarization-insensitive absorber based on gradient structure metamaterial. *Journal of Applied Physics*, 115(17), 17E523.
- Ye, Y., Jin, Y., He, S., 2009. Omni-directional, broadband and polarization-insensitive thin absorber in the terahertz regime. *arXiv preprint arXiv:0906.2137*.
- Yoo, Y. J., Kim, Y. J., Hwang, J. S., Rhee, J. Y., Kim, K. W., Kim, Y. H., Cheong, H., Chen, L. Y., Lee, Y. P., 2015. Triple-band perfect metamaterial absorption, based on single cut-wire bar. *Applied Physics Letters*, 106(7), 071105-0711056.
- You, K. Y., Abbas, Z., Malek, M. F. A., Cheng, E. M., 2014. Non-destructive Dielectric Measurements and Calibration for Thin Materials Using Waveguide-Coaxial Adaptors. *Measurement Science Review*, 14(1), 16-24.
- Yu, Z., Liu, S., Fang, C., Huang, X., Yang, H., 2015. Design, simulation, and fabrication of single-/dual-/triple band metamaterial absorber. *Physica Scripta*, 90(6), 065501--065506.

- Yuan, H., Zhu, B. O., Feng, Y., 2015. A frequency and bandwidth tunable metamaterial absorber in x-band. *Journal of Applied Physics*, 117(17), 173103-173109.
- Zaichun, C., Rahmani, M., Yandong, G., Chong, C. T., Minghui, H., 2012. Realization of Variable Three-Dimensional Terahertz Metamaterial Tubes for Passive Resonance Tunability. *Advanced Materials*, 24(23), OP143–OP147.
- Zhang, H., Cao, X. Y., Gao, J., Yang, H., Yang, Q., 2014. A novel dual-band metamaterial absorber and its application for microstrip antenna. *Progress In Electromagnetics Research Letters*, 44, 35-41.
- Zhang, W., Liu, A. Q., Zhu, W. M., Li, E. P., Tanoto, H., Wu, Q. Y., eng, J. H., Zhang, X. H., Tsai, M. L. J., Lo, G. Q., Kwong, D. L., 2012. Micromachined switchable metamaterial with dual resonance. *Applied Physics Letters*, 101(15), 151902-151907.
- Zhang, Y., Zhou, L., Li, J. Q., Wang, Q. J., & Huang, C. P., 2015. Ultra-broadband and strongly enhanced diffraction with metasurfaces. *Scientific reports*, 5, 10119.
- Zheludev, N. I., Kivshar, Y. S., 2012. From metamaterials to metadevices. *Nature materials*, 11(11), 917-924.
- Zhong, S., & He, S., 2013. Ultrathin and lightweight microwave absorbers made of mu-near-zero metamaterials. *Scientific reports*, (3), 2083(1-5).
- Zhu, B., Huang, C., Feng, Y., Zhao, J., Jiang, T., 2010. Dual band switchable metamaterial electromagnetic absorber. *Progress In Electromagnetics Research B*, 24, 121-129.
- Zhu, W. M., Liu, A. Q., Bourouina, T., Tsai, D. P., Teng, J. H., Zhang, X. H., Lo, G. Q., Kwong, D. L., Zheludev, N. I. (2012). Microelectromechanical Maltese-cross metamaterial with tunable terahertz anisotropy. *Nature communications*, 3, 1274.
- Zhu, W. M., Liu, A. Q., Zhang, W., Tao, J. F., Bourouina, T., Teng, J. H., Zhang, X. H., Wu, Q. Y., Tanoto, H., Guo, H. C., Lo, G. Q., Lo, G. Q., 2011. Polarization dependent state to polarization independent state change in THz metamaterials. *Applied Physics Letters*, 99(22), 221102-2211023.

Zhu, W. M., Liu, A. Q., Zhang, X. M., Tsai, D. P., Bourouina, T., Teng, J. H., Zhang, X. H., Guo, H. C., Tanoto, H., Mei, T., Lo, G. Q., Lo, G. Q., 2011. Switchable magnetic metamaterials using micromachining processes. *Advanced Materials*, 23(15), 1792-1796.

Zhu, W., Zhao, X., Gong, B., Liu, L., Su, B., 2011. Optical metamaterial absorber based on leaf-shaped cells. *Applied Physics A*, 102(1), 147-151.

Zouhdi, S., Sihvola, A., and Aarsalane, M., 2012. *Advances in electromagnetics of complex media and metamaterials (Vol. 89)*. Springer Science & Business Media.



## RESUME

Name Surname : Khalid Saeed Lateef AL-BADRI

Place/Date of birth: Sala Din-IRAQ, 1983

Marital Status : Married

Foreign Language : English

E-mail : saaedkhalid@gmail.com



### **Educational Background**

High school : Al-Khatib High School, 2001

Bachelor : University of Baghdad - Al-Khwarizmi collage of Engineering  
Department of Information and Communication, 2006.